Development of cathodic electrocatalysts for low temperature H_2 fuel cell applications: Improving oxygen reduction activity through the manipulation of size, shape, and composition

by

Timothy Blair Van Cleve

A dissertation submitted in partial fulfillment
of the requirements for the degree of
Doctor of Philosophy
(Chemical Engineering)
in the University of Michigan
2016

Doctoral Committee:

Professor Suljo Linic, Chair
Professor Mark A. Barteau
Professor Charles McCrory
Professor Johannes W. Schwank

This dissertation is dedicated to my family,

especially Dad

Acknowledgements

I am very appreciative for all of the support and encouragement that has led to the completion of this thesis. I wish to thank my advisor, Prof. Suljo Linic, for his guidance and enthusiasm which has helped me grow as a researcher. I would also like to express my gratitude toward my thesis committee members, Professors Mark Barteau, Charles McCrory, and Johannes Schwank, first for being so accommodating when scheduling meetings, but also for giving meaningful suggestions and dialogue during our discussions.

Thanks to all Linic group members, past and present. I would not have completed my PhD if it hadn't been for all your suggestions, dialogue, criticism, and patience. All of you made last few years working at Michigan such a rewarding experience. In particular, I wish to acknowledge Dr. Hongliang Xin, Dr. Adam Holewinski, Saman Moniri, Emily Gibara, and Gaby Belok for all their contributions over the course of my doctoral work. Additionally, I would like to thank several collaborators: Dr. Juan Carlos Idrobo and Dr. Karren L. More (Oakridge National Laboratory), and Dr. John Katsoudas (Argonne National Laboratory) for their assistance with characterizing our electrocatalysts.

To all of my friends from Ann Arbor, thanks for all of the adventures outside of research, which enriched my experience at Michigan. I was so lucky to have made such great friends during the past few years and I wish all of you the best of luck in your future endeavors.

Thanks to my family, Carol, Kevin, Kelley, and Jeff for their love and unwavering support throughout the entirety of my life. I would not be able to achieve this degree without your

encouragement. Finally, I want to thank my wife, Laura, for … everything. I am very excited to start our next adventure in Colorado together.

Table of Contents

List of Figures

Figure

List of Tables

Table

Abstract

In this dissertation, the oxygen reduction activity of metal nanoparticle electrocatalysts is improved through the manipulation of their size, shape, and composition. The design of superior catalysts first requires identifying processes that limit overall performance. On both silver and platinum electrodes, the rate of oxygen reduction is limited by the initial proton/electron transfer to O_2, however the limited site availability also limits ORR activity of platinum at high electrochemical potentials. Different approaches must employed to improve the activity of platinum and silver electrocatalysts.

The first project in this thesis describes the development of Pt alloy electrocatalysts with enhanced ORR activity compared to Pt/C standards. The design of Pt monolayer electrocatalysts is informed by quantum chemical calculations. By understanding how alloying impacts the reactivity of surface atoms, we are able to prepare a special class of catalysts with finely tunable activity dependent upon the composition of their nanoparticle core. The best performing materials have specific activities up to four times higher than Pt/C electrocatalysts. Rigorous characterization and electrochemical testing confirm these enhancements and the observed trends in activity result from the alloy structure rather than size and shape effects.

The second project focuses on controlling the morphology of Ag electrocatalysts in order to improve their alkaline ORR activity. In this study, the rates on Ag nanospheres and Ag nanocubes are compared over a wide range of metal loadings. Contrary to our original hypothesis, nanospheres are found to be slightly more active than nanocubes. Rigorous experimental work

confirms the reported shape dependence effects are consistent with the relative abundance of 111 and 100 sites on Ag nanoparticles.

Chapter 1

Introduction

1.1 Summary

This chapter provides a general introduction to low temperature fuel cells, giving a basic overview of how fuel cells operate and describing the various inefficiencies that diminish device performance. The chapter begins with a brief discussion about the importance of catalysts and their applications. The discussion then focuses on the potential of fuel cell technology to alleviate the negative environmental consequences of our dependence on fossil fuels. We then describe the basic operation of fuel cells, including an introduction to the oxygen reduction reaction, which is the main source of efficiency losses in fuel cells. General trends in catalytic activity will be described on existing platinum, silver, and carbon/nitrogen-based materials. The end of this chapter provides an overview of the work presented in this thesis with short descriptions of each subsequent chapter.

1.2 Catalysts and their applications

Recent technological advances in food production, chemical industries, and manufacturing have enabled humanity to achieve unforeseen prosperity. Many technologies rely on catalysts, which are substances that increase the rate of chemical reactions without undergoing a permanent physical or chemical change, to efficiently convert reactants and fuels into desired products and energy. For example, homogeneous catalysts are used in the pharmaceutical industry to synthesize

high purity and effective medicines with less harmful side effects.[1,2] Catalysts are also used in the production of different plastics as well as in manufacturing their precursors such as ethylene, propylene, and various epoxides.[3–6] Exhaust systems in automobiles contain catalysts, which reduce the amount of harmful chemicals expelled as pollution, drastically improving air quality in many big cities.[7]

Arguably one of the most important application of catalysts is the Haber-Bosch process for synthesizing ammonia, a vital chemical precursor for fertilizer. Ammonia-based fertilizers improve crop yields enabling greater availability of food and better nutrition, and is a major reason for recent increases in global population.[8] In fact, the majority of N found in human protein originates from NH_3 produced by the Haber-Bosch process.[9]

In the Haber-Bosch process, nitrogen gas (N_2) from air is combined with excess hydrogen gas (H_2) to produce ammonia (NH_3) as shown in the equation 1.1. Despite being an exothermic reaction, substantial energy is required to activate N_2 by breaking the strong N-N bond. Specifically, catalysts interact with N_2 to lower the activation barriers, thus increasing the rate of ammonia production at comparable operating conditions. Consequently, significant rates and yields can be achieved at much lower temperatures by utilizing effective catalysts.

$$N_2\,(g) + 3H_2\,(g) \rightarrow 2NH_3\,(g) \quad (1.1)$$

1.3 Global challenges

Humanity has long faced problems associated with the scarcity of resources such as food, water, land, and raw materials essential to maintain standards of living. In an increasingly interconnected world, we have been able to better address some local shortages, but with newfound prosperity, humanity is now faced with these challenges on a global scale. One major challenge

is how we can mitigate our environmental impact without sacrificing our standard of living. Specifically, our society is currently very dependent upon fossil fuels as a chemical and energy source, but the introduction of additional carbon into the atmosphere and oceans has several severe environmental consequences. While the exact extent of the environmental impact is difficult to forecast, now is the time to develop and test solutions before irreversible damage occurs.

Currently, the US consumes roughly 100 Quadrillion BTUs of energy annually, accounting for 18% of the global energy demand.[10,11] Roughly ¼ of our national energy is used to fuel the transportation sector.[11] Petroleum supplies over 90% this demand, with less than 10% coming from renewables such as ethanol and electricity.[11] As standards of living and population sizes continue to grow, particularly in countries like China, India, and Brazil, there will be even greater demand for fossil fuels.[12] There is an urgent need to develop clean and efficient energy systems to address our reliance on fossil fuels for transportation needs. The development of hydrogen fuel cell powered vehicles has received considerable attention as an alternative mode of mobile power generations.

1.4 Fuel cells

Low temperature fuel cells generate electrical energy from the exothermic reaction that converts hydrogen (H_2) and oxygen (O_2) gases into water (H_2O) (equation 1.2a). The overall fuel cell reaction consists of two electrochemical half reactions: the oxidation of hydrogen (H_2) (equation 1.2b) and the reduction of oxygen (O_2) (equation 1.2c), which occur separately at the anode and cathode electrodes. Often, Pt nanoparticle electrocatalysts are used to increase the reaction rates at both electrodes. The electrolyte, the phase located between these electrodes, enables the transport of charged chemical species such as protons (H^+) or hydroxide anions (OH^-) across the cell. In a proton exchange membrane (PEM) fuel cell, the acidic electrolyte contains

significant H^+ concentrations. Fuel cells can also operate in basic media, where OH^- is a dominant charged species.

$$2H_2 + O_2 \rightarrow 2H_2O \quad (1.2a)$$

$$H_2 \rightarrow 2H^+ + 2e^- \quad (1.2b)$$

$$4H^+ + 4e^- + O_2 \rightarrow 2H_2O \quad (1.2c)$$

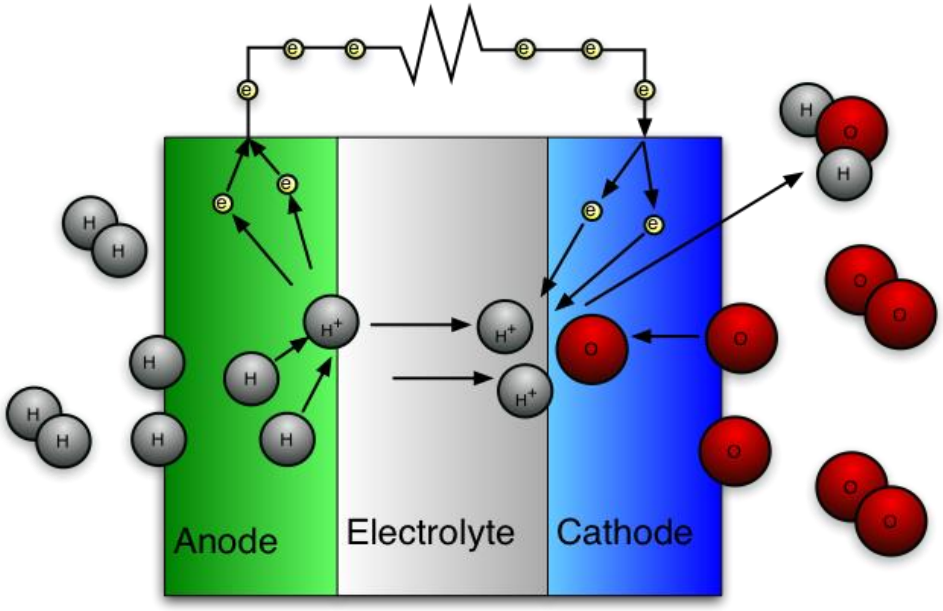

Figure 1.1. Representation of PEM fuel cell consuming hydrogen (H_2) and oxygen (O_2) gases to produce water (H_2O).

Figure 1.1 describes how a PEM fuel works. At the anode, hydrogen gas is oxidized to form protons and energetic electrons. The protons are shuttled across the proton exchange membrane where they react at the cathode. Meanwhile, these energetic electrons travel through an external circuit where they can deposit energy to a load such as an electric motor. At the cathode, protons and electrons react with molecular oxygen to form water as the product. In general, the oxidization reaction is much quicker than the multi-step reduction reaction.

The power generated by the fuel cell is the product of current, which is the rate at which electrons are created, and potential, which is the energy carried by each electron. Thermodynamics limit the maximum potential drop across a fuel cell to 1.23 V at standard conditions, but at this potential, there is no driving force promoting the formation of water. Consequently, no current can be drawn from the fuel cell at this condition, which is known as open circuit or equilibrium cell potential. Some of this voltage must be sacrificed for the fuel cell to generate appreciable current and power. On the other end of the spectrum, at low cell potentials, the rate of generation of electrons is limited by the diffusion of reactants through the cell, thus limiting the maximum achievable current. This is known as the short circuit current. Optimal power generation is achieved by operating at some intermediate voltage while drawing as large a current as possible at that potential.

1.5 Major limitations in current fuel cells

As previously mentioned, fuel cell efficiency is limited primarily by the oxygen reduction reaction (ORR), which occurs at much lower rates than the hydrogen oxidization at the anode.[13] Furthermore, analyzing the performance of individual fuel cell components found that the majority of potential losses were associated with activation of the cathodic reaction, as shown in Figure 1.2.[14] This figure shows how the cell potential, the difference between electrode potentials, varies as a function of current drawn in four different fuel cell assemblies. An ideal fuel cell would be able to generate high currents at high voltages (near the open circuit voltage of 1.169 V), but a large amount of potential is sacrificed to overcome kinetic barriers associated with the oxygen reduction reaction (η_{ORR}). These *i*-*V* curves show that ORR limits overall fuel cell performance across a wide range of operating conditions.

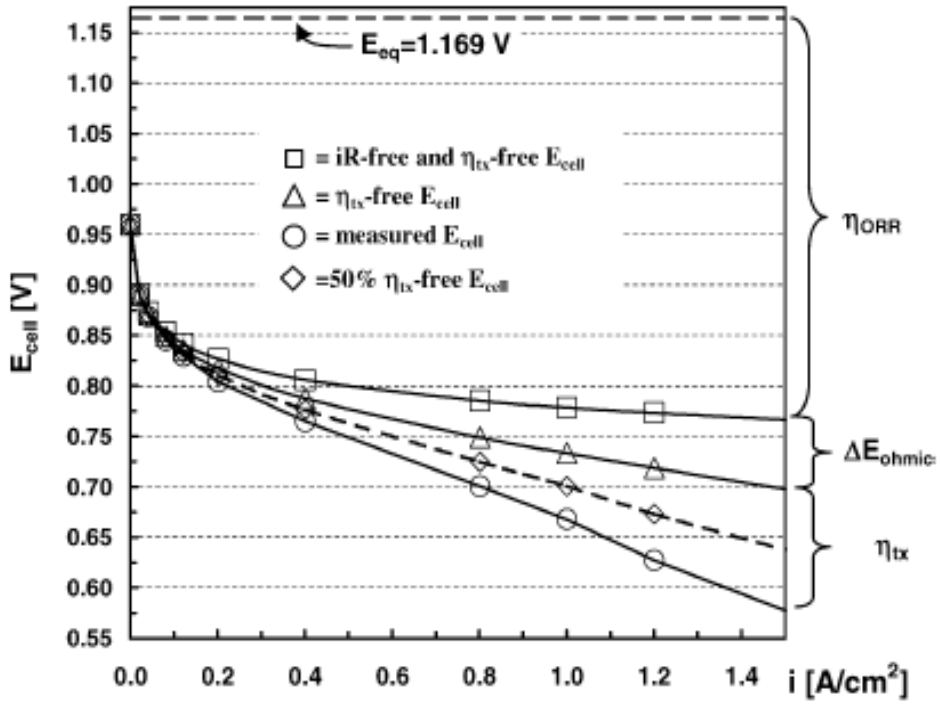

Figure 1.2. A current-voltage plot comparing the effect of various inefficiencies on cell potential drops as a function of generated current density.[14]

To overcome these sluggish kinetics, the loading of Pt catalysts at the cathode is often increased, but this has the negative consequence of increasing overall device cost. In current fuel cell technology, the catalyst cost already accounts for over 35 % of the total fuel cell assembly cost.[14] The development of cheaper, more active, and more stable electrocatalysts for the oxygen reduction reaction is vital for fuel cells to become more competitive with conventional technologies like internal combustion engines. A summary of DOE targets for ORR catalyst performance are presented in Table 1.[15]

Table 1. DOE technical targets for fuel cell electrocatalysts

Characteristic	Units	2011 Status[16,17]	2020 Target
Platinum group metal content (both electrodes)	g / kW	0.19	0.125
Platinum group metal (PGM) total loading	mg PGM / cm^2 electrode area	0.15	0.125
Loss in initial catalytic activity after 30k cycles	% mass activity loss	48	<40
Electrocatalyst support stability after 30k cycles	% mass activity loss	<10	<10
Mass Activity	A/mg Pt @ 0.9V	0.24	0.44
Non-Pt catalyst activity per volume of support catalysts	A/cm^3 @ 0.8V	60-165	300

1.6 Oxygen Reduction Reaction

In order to design a better ORR catalyst, it is important to understand how this electrochemical reaction proceeds on a catalyst surface. There has been extensive work investigating the oxygen reduction reaction on polycrystalline and single crystal metal electrodes as well as on supported nanoparticle systems.[18–21] Platinum (Pt) has been extensively studied because it has the highest specific activity (catalytic activity normalized by surface area) among all single element catalysts.[22] There is much experimental evidence suggesting that ORR proceeds through the following sequence of elementary reactions on the Pt(111) surface.[23–26] Note, $*$ designates an empty catalytic site and $ads*$ corresponds to species *ads* adsorbed on the catalyst.

$$O_2 + H^+ + e^- + * \rightarrow OOH* \quad (1.3a)$$

$$OOH* + * \rightarrow OH* + O* \quad (1.3b)$$

$$O* + H^+ + e^- \rightarrow OH* \quad (1.3c)$$

$$2\,(OH* + H^+ + e^- \rightarrow H_2O + *) \quad (1.3d)$$

The first elementary step in this catalytic cycle involves the transfer of a proton and electron to molecular oxygen to create a high energy hydroperoxyl surface intermediate (equation 1.3a). This species then chemically decomposes to a surface oxygen and hydroxyl species in the proximity of an empty surface site (equation 1.3b). These oxygenated species are then reduced and removed from the surface through a series of proton/electron transfers (reduction steps) producing two molecules of water for every oxygen molecule consumed (equations 1.3c and 1.3d).

Microkinetic modeling of the proposed ORR mechanism can predict rate dependencies on potential, pH, and O_2 assuming one of the elementary steps is rate limiting while other steps are at equilibrium. Experimental evidence of the relationship between potential and ORR rate (described in detail in Chapter 2) is consistent with the mechanism reported above, where O_2 activation is the rate limiting step on a clean Pt surface.[23] However, at operating conditions the relationship between potential and rate is complicated by the availability of surface sites. Therefore, the overall rate of ORR on Pt is limited both by its ability to activate O_2 as well as the availability of surface sites, which become saturated with OH* and water at high potentials.

As pure Pt electrocatalysts do not exhibit the necessary activity required for cost-effective fuel cells, current research has focused on improving both the catalyst's ability to activate O_2 and the availability of surface sites. In the following sections, I will highlight some seminal work on different ORR catalyst systems. In particular, I will emphasize different trends relating particle shape and size effects to ORR activity that have been reported in literature. Special attention will be given to how these results impact our work on developing improved platinum alloy and silver ORR electrocatalysts.

1.7 Previous research

1.7.1 Platinum as ORR catalyst

Platinum has been extensively studied because it exhibits the highest ORR activity compared to all other single elements. Additionally, Pt is one of few transition metals stable under the highly oxidizing conditions experienced at the PEM fuel cell cathode. At high potentials, the Pt surface oxidizes to form a surface oxide PtO rather than dissolving as ions in solution like other metals. In order to improve catalytic activity on a cost basis, early research efforts focused on maximizing the availability of active surface sites, both by reducing the extent of this oxidation and by reducing the particle size of the catalysts.

By shrinking the size of Pt electrocatalysts, a larger portion of atoms are on the particle surface, and therefore a larger portion can participate as reactive sites. Extensive size dependence studies have shown much higher mass activities are obtained for ~3nm Pt nanoparticles compared to large nanoparticles.[27,28] Unfortunately, smaller nanoparticles exhibit limited catalytic activity despite the high dispersion, or surface area to mass ratio. This is a result of reduced intrinsic activity with decreasing particle size. Smaller particles have much higher concentration of under-coordinated atoms, which are highly reactive, but tend to be poisoned by strongly interacting adsorbates.[28] Examining the ORR activity normalized on a surface area basis indicates larger nanoparticles perform better due to higher proportion of terrace sites. At sizes of roughly 11 nm, Pt nanoparticles exhibit specific activities of around 2.0 mA/cm^2 at 0.9 V_{RHE} which are comparable to polycrystalline Pt electrodes.[28]

Additional work on Pt single crystal electrodes demonstrates that the Pt(111) surface is much more active than Pt(110) and Pt(100) surfaces in non-interacting electrolyte such as perchloric acid.[29,30] Therefore, superior ORR activity can be achieved by increasing the relative

abundance of 111 sites on Pt nanoparticles.[31] There have been many reports which indicate that activities can be roughly doubled compared to quasi-spherical nanoparticles through the synthesis of Pt octahedra.[31–33] Unfortunately, manipulation of size and shape of pure Pt nanoparticles cannot achieve the activity benchmarks described in Table 1.[21,34] For this reason, recent Pt-based electrocatalysts work has focused on reducing cost by decreasing Pt content while simultaneously improving activity and stability through alloying.[24,35–37] This work will be covered in greater detail, as it leads to the work presented in this dissertation, in Chapters 4 and 5.

1.7.2 Silver as ORR catalyst

Historically, silver electrodes have been well studied electrocatalysts for alkaline fuel cells because of their moderately high activity and low cost relative to Pt electrodes.[38] Silver is not stable in the highly acidic conditions of PEM fuel cells, but it is strongly resistant to oxidization in alkaline solution. Previous studies on Ag catalysts report inconsistent trends in ORR activity as a consequence of particle shape and size.[39–42] Similar activity between Ag(100) and Ag(111) electrodes further makes it difficult to distinguish enhancements between Ag samples with different morphologies.[43,44] Compared to Pt, Ag is much less chemically reactive making the O_2 activation step rate limiting on these materials. Existing research on improving reactivity of silver electrocatalysts, as it relates to our work in this area, is presented in Chapter 6.

1.7.3 "Costless" Catalysts

Another strategy for obtaining high mass activities is the development of "cost-less" catalysts. These materials are much less active than Pt, but are composed of cheap and abundant elements like carbon (C), nitrogen (N), and iron (Fe). The proposed active sites are metal atoms bound to N in a polyphyrin ring similar to the heme group of hemoglobin in red blood cells.[45,46] A major limitation of costless catalysts are their low site density compared to metal nanoparticle

electrodes. While these materials may show high activities on a mass or cost basis, their low dispersion requires significant volume to achieve desired ORR rates. This volumetric constraint requires potential ORR catalysts to have activities no less than 1/10 of the activity of Pt.[14,38] While these materials continue to be extensively studied, these materials were not studied in this work and will not be thoroughly discussed.

1.8 Scope of this dissertation

The objective of this dissertation is to demonstrate how the catalytic activity of nanoparticles can be improved through selective manipulation of their size, shape, and composition. Specifically, the design of the electrocatalysts used in this work were guided by understanding the atomic level interactions between surface atoms and key intermediates in order to improve rates of oxygen reduction on Pt and Ag based electrodes.

Chapter 2 describes our bottom-up approach for designing catalysts with improved reaction kinetics based on atomic-level understanding of interaction between key chemical species on the catalytic surface. Microkinetic modeling is employed to understand which elementary steps control overall ORR rates on Pt and Ag surfaces. Density functional theory is applied to understand the relationship between catalyst nanostructure and the adsorption energy of key intermediates that govern overall catalytic performance.

Chapter 3 is a general survey of theoretical and experimental techniques utilized during this project. This chapter aims to provide the reader with a basic description of quantum chemical calculations, electrochemical methods, nanoparticle synthesis approaches, and characterization techniques and their applications. In depth discussion of experimental details and analysis are located in later chapters.

Chapter 4 focuses on the design and development of Pt monolayer electrocatalysts with enhanced ORR activity compared to pure Pt. Density functional theory calculations help identify Pt_{ML} electrocatalysts with subsurface Au as a promising material for study due to their slightly weakened OH affinity. A combined chemical and electrochemical synthesis method was developed to prepare electrocatalyst samples with $Au_xCu_y@Au_2@Pt$ structure. The activity and stability of these catalysts were assessed and compared with Pt nanoparticle standards. We find that our materials exhibit improved performance relative to Pt.

In Chapter 5, the effects of core composition on the ORR activity of $Au_xCu_y@Au_2@Pt$ structured electrocatalysts are examined across wider range of compositions in order to elucidate trends and relationships of interest. In this chapter, greater emphasis is placed on how ligand and lattice effects manipulate the OH binding energy and ultimately catalytic activity. Extensive characterization of alloy catalyst show evidence of weaker OH binding with increased compressive strain induced by higher Cu content within core.

In Chapter 6, the alkaline oxygen reduction activities on different Ag nanoparticles are compared. We find that Ag nanospheres are slightly more active than Ag nanocubes across a wide range of loadings. These enhancements were consistent with the relative abundance of 111 and 100 terrace sites.

Chapter 7 is the final chapter of the dissertation. This chapter states the general conclusions of the work presented in this dissertation and proposes future avenues of research.

1.9 References

1. Schmid, R. Homogeneous Catalysis with Metal Complexes in a Pharmaceuticals' and Vitamins' Company: Why, What for, and Where to Go? at <http://www.ingentaconnect.com/content/scs/chimia/1996/00000050/00000003/art00013>

2. Mills, P. L., Ramachandran, P. A. & Chaudhari, R. V. MULTIPHASE REACTION

ENGINEERING FOR FINE CHEMICALS AND PHARMACEUTICALS. *Rev. Chem. Eng.* **8,** 1–176 (1992).

3. Reich, L. & Stivala, S. S. A general kinetic scheme for ziegler-type polymerizations. *J. Polym. Sci. Part A Gen. Pap.* **1,** 203–216 (1963).

4. NATTA, G. *Stereoregular Polymers and Stereospecific Polymerizations*. *Stereoregular Polymers and Stereospecific Polymerizations* (Elsevier, 1967). doi:10.1016/B978-1-4831-9883-5.50027-1

5. Marimuthu, A., Zhang, J. & Linic, S. Tuning selectivity in propylene epoxidation by plasmon mediated photo-switching of Cu oxidation state. *Science* **339,** 1590–3 (2013).

6. Christopher, P. & Linic, S. Engineering selectivity in heterogeneous catalysis: Ag nanowires as selective ethylene epoxidation catalysts. *J. Am. Chem. Soc.* **130,** 11264–5 (2008).

7. Fales Jr., E. D. His Smoke-Eating 'Cats' Now Attack Traffic Smog. *Pop. Sci.* 83–85 (1955).

8. Smil, V. Detonator of the population explosion. **400,** 415 (1999).

9. Howarth, R. W. Coastal nitrogen pollution: A review of sources and trends globally and regionally. *Harmful Algae* **8,** 14–20 (2008).

10. Ad, U. E. I. International Energy Statistics - EIA. (2012). at <https://www.eia.gov/cfapps/ipdbproject/IEDIndex3.cfm?tid=44&pid=44&aid=2>

11. US Energy Information Adminstration. Annual Energy Outlook 2015. **1,** 1689–1699 (2015).

12. BP. BP Energy Outlook 2035. (2015). at <http://www.bp.com/content/dam/bp/pdf/energy-economics/energy-outlook-2015/Energy_Outlook_2035_booklet.pdf>

13. Debe, M. K. Electrocatalyst approaches and challenges for automotive fuel cells. *Nature* **486,** 43–51 (2012).

14. Gasteiger, H. A., Kocha, S. S., Sompalli, B. & Wagner, F. T. Activity benchmarks and requirements for Pt, Pt-alloy, and non-Pt oxygen reduction catalysts for PEMFCs. *Applied Catalysis B: Environmental* **56,** 9–35 (2005).

15. *Multi-Year Research, Development and Demonstration Plan: Technical Plan - Fuel Cells*. (2012). at <http://www1.eere.energy.gov/hydrogenandfuelcells/mypp/pdfs/fuel_cells.pdf>

16. Debe, M. K. U.S. Department of Energy Hydrogen and Fuel Cells Program. in *Annual Merit Review Proceedings* (2011).

17. Zelenay, P. *et al. FY 2011 Progress Report for the DOE Hydrogen Program*. (2011).

18. Schmidt, T. J., Grgur, B. N., Gasteiger, H. A., Behm, R. J. & Ross, P. N. Effect of Temperature on Surface Processes at the Pt (111) - Liquid Interface : Hydrogen Adsorption , Oxide Formation , and CO Oxidation. 8568–8577 (1999).

19. Greeley, J., Rossmeisl, J., Hellmann, A. & Norskov, J. K. Theoretical Trends in Particle

Size Effects for the Oxygen Reduction Reaction. *Zeitschrift für Phys. Chemie* **221,** 1209–1220 (2007).

20. Mayrhofer, K. J. J. *et al.* The impact of geometric and surface electronic properties of pt-catalysts on the particle size effect in electrocatalysis. *J. Phys. Chem. B* **109,** 14433–40 (2005).

21. Nesselberger, M. *et al.* The particle size effect on the oxygen reduction reaction activity of Pt catalysts: influence of electrolyte and relation to single crystal models. *J. Am. Chem. Soc.* **133,** 17428–33 (2011).

22. Nørskov, J. K. *et al.* Origin of the overpotential for oxygen reduction at a fuel-cell cathode. *J. Phys. Chem. B* **108,** 17886–17892 (2004).

23. Holewinski, A. & Linic, S. Elementary Mechanisms in Electrocatalysis: Revisiting the ORR Tafel Slope. *J. Electrochem. Soc.* **159,** H864–H870 (2012).

24. Xin, H., Holewinski, A. & Linic, S. Predictive Structure–Reactivity Models for Rapid Screening of Pt-Based Multimetallic Electrocatalysts for the Oxygen Reduction Reaction. *ACS Catal.* **2,** 12–16 (2012).

25. Grgur, B. N., Marković, N. M. & Ross, P. N. Temperature-dependent oxygen electrochemistry on platinum low-index single crystal surfaces in acid solutions. *Can. J. Chem.* **75,** 1465–1471 (1997).

26. Markovic, N. Surface science studies of model fuel cell electrocatalysts. *Surf. Sci. Rep.* **45,** 117–229 (2002).

27. Gasteiger, H. a. *et al.* Fuel Cell Basics. *Hydrog. energy* (2010).

28. Perez-Alonso, F. J. *et al.* The effect of size on the oxygen electroreduction activity of mass-selected platinum nanoparticles. *Angew. Chem. Int. Ed. Engl.* **51,** 4641–3 (2012).

29. Markovic, N., Gasteiger, H., Ross, P. N., Berkeley, L. & Division, M. S. Kinetics of Oxygen Reduction on Pt (hkl) Electrodes : Implications for the Crystallite Size Effect with Supported Pt Electrocatalysts. *J. Electrochern. Soc* **144,** 1591–1597 (1997).

30. Schmidt, T. J., Stamenkovic, V., Ross, Jr., P. N. & Markovic, N. M. Temperature dependent surface electrochemistry on Pt single crystals in alkaline electrolyte. *Phys. Chem. Chem. Phys.* **5,** 400–406 (2003).

31. Cui, C., Gan, L., Heggen, M., Rudi, S. & Strasser, P. Compositional segregation in shaped Pt alloy nanoparticles and their structural behaviour during electrocatalysis. *Nat. Mater.* **12,** 765–71 (2013).

32. Choi, S. Il *et al.* Synthesis and characterization of 9 nm Pt-Ni octahedra with a record high activity of 3.3 A/mgPt for the oxygen reduction reaction. *Nano Lett.* **13,** 3420–3425 (2013).

33. Wu, J. & Yang, H. Synthesis and electrocatalytic oxygen reduction properties of truncated octahedral Pt3Ni nanoparticles. *Nano Res.* **4,** 72–82 (2010).

34. Pedersen, C. M. *et al.* Benchmarking Pt-based electrocatalysts for low temperature fuel

cell reactions with the rotating disk electrode: oxygen reduction and hydrogen oxidation in the presence of CO (review article). *Electrochim. Acta* (2015). doi:10.1016/j.electacta.2015.03.176

35. Greeley, J. *et al.* Alloys of platinum and early transition metals as oxygen reduction electrocatalysts. *Nat. Chem.* **1,** 552–6 (2009).

36. Xin, H., Holewinski, A., Schweitzer, N., Nikolla, E. & Linic, S. Electronic Structure Engineering in Heterogeneous Catalysis: Identifying Novel Alloy Catalysts Based on Rapid Screening for Materials with Desired Electronic Properties. *Top. Catal.* **55,** 376–390 (2012).

37. Xin, H. & Linic, S. Communications: Exceptions to the d-band model of chemisorption on metal surfaces: The dominant role of repulsion between adsorbate states and metal d-states. *J. Chem. Phys.* **132,** 221101 (2010).

38. Holewinski, A., Idrobo, J.-C. & Linic, S. High-performance Ag-Co alloy catalysts for electrochemical oxygen reduction. *Nat. Chem.* **6,** 828–34 (2014).

39. Singh, P. & Buttry, D. A. Comparison of Oxygen Reduction Reaction at Silver Nanoparticles and Polycrystalline Silver Electrodes in Alkaline Solution. *J. Phys. Chem. C* **116,** 10656–10663 (2012).

40. Dong, X., Gu, H., Kang, J., Yuan, X. & Wu, J. Effects of the surface modification of silver nanoparticles on the surface-enhanced Raman spectroscopy of methylene blue for borohydride-reduced silver colloid. *J. Mol. Struct.* **984,** 396–401 (2010).

41. Wang, Q. *et al.* Shape-dependent catalytic activity of oxygen reduction reaction (ORR) on silver nanodecahedra and nanocubes. *J. Power Sources* **269,** 152–157 (2014).

42. Lee, C.-L., Tsai, Y.-L., Huang, C.-H. & Huang, K.-L. Performance of silver nanocubes based on electrochemical surface area for catalyzing oxygen reduction reaction. *Electrochem. commun.* **29,** 37–40 (2013).

43. Blizanac, B. B., Ross, P. N. & Marković, N. M. Oxygen reduction on silver low-index single-crystal surfaces in alkaline solution: rotating ring disk(Ag(hkl)) studies. *J. Phys. Chem. B* **110,** 4735–41 (2006).

44. Ohyama, J. *et al.* Oxygen reduction reaction over silver particles with various morphologies and surface chemical states. *J. Power Sources* **245,** 998–1004 (2014).

45. Su, D. S. *et al.* Metal-free heterogeneous catalysis for sustainable chemistry. *ChemSusChem* **3,** 169–80 (2010).

46. Jaouen, F. *et al.* Cross-laboratory experimental study of non-noble-metal electrocatalysts for the oxygen reduction reaction. *ACS Appl. Mater. Interfaces* **1,** 1623–39 (2009).

Chapter 2

Understanding Catalytic Reactions

2.1. Summary

This chapter describes in greater detail how catalysts improve reaction rates of chemical and electrochemical reactions. The chapter begins by describing how microkinetic modeling is used to understand how overall rates are influenced by the kinetics of elementary steps in the reaction mechanism. This methodology is then applied to electrochemical oxygen reduction reaction on Pt and Ag to identify the most likely ORR mechanism on these surfaces. Next, general trends of chemisorption on transition metal surfaces are discussed to understand how changing catalyst properties impacts elementary steps. Specifically, the relationship between OH binding energy and ORR activity will be explained. The end of the chapter will briefly review the major conclusions from previous studies and describe how these results motivate the current work.

2.2. Introduction

Accurate mathematical modeling of reactive systems has tremendous power to predict experimental outcomes and inform process development and optimization. Often it is difficult, if not impossible, to directly or accurately measure all parameters such as activation barriers or rate constants for the elementary reactions that govern macroscopic system behavior. However, fundamental understanding of the relationships between these parameters can simplify complex problems, enabling the discovery of suitable solutions. This section will focus on how the

application of microkinetic modeling and quantum chemical calculations to model catalyst surfaces can guide the design of improved catalytic materials.

2.3. Microkinetic modeling of chemical reactions

Microkinetic modeling is a powerful methodology used in chemical reactor design to elucidate parameters related to microscopic processes from macroscopic observations on the reactor scale. Identifying which processes or rates control the overall performance aids reactor and catalyst design. In general, basic reaction modeling on thermal and electrochemical reactions will be discussed, with a special focus on the electrochemical oxygen reduction reaction on Pt and Ag surfaces.

Even relatively simple chemical reactions can exhibit complex rate behaviors as a function of operating conditions. Studying the simple reaction between reactants A and B to form product AB, the rate of AB formation (or A/B consumption) can be expressed by the rate law (Eqn 2.1)

$$r = k a_A^{\alpha} a_B^{\beta} a_{AB}^{\gamma} \qquad (2.1)$$

where k is the reaction rate constant, a_i is the activity (related to concentration or partial pressure) of species i, and parameters α, β, and γ correspond to the reaction rate orders of species A, B, and AB. Rate constants and rate orders can be experimentally determined by systematically studying the dependence of rate on temperature and reactant/product concentrations. It has been empirically shown that rate constants have an exponential dependence on temperature described by the Arrhenius equation, where E_A is the activation barrier, T is the absolute temperature, R is the universal gas constant, and A is a pre-exponential factor.

$$k(T) = A * \exp\left(\frac{-E_A}{RT}\right) \qquad (2.2)$$

Figure 2.1 shows the energetics of an exothermic reaction proceeding through different reaction pathways. The activation barrier (E_A) corresponds to the energy difference between the highest energy (transition) state and reactant state during a chemical transformation. Intuitively, reactions with lower activation barriers will occur more frequently due to higher rate constants compared to pathways with higher barriers. Essentially, catalysts accelerate chemical reactions by interacting with molecules to lower activation barriers effectively creating new, faster pathways. Catalysts cannot affect thermodynamic properties such as heats of reaction or equilibrium constants. While improving reaction rates, catalysts introduce further complexity into reaction mechanism by introducing multiple elementary reaction steps. Provided a reaction mechanism, microkinetic modeling can describe macroscopic properties such as *r* and *k* in terms of microscopic parameters. Microkinetic modeling can also be used to evaluate the validity of proposed reaction mechanisms in conjunction with experimental results.

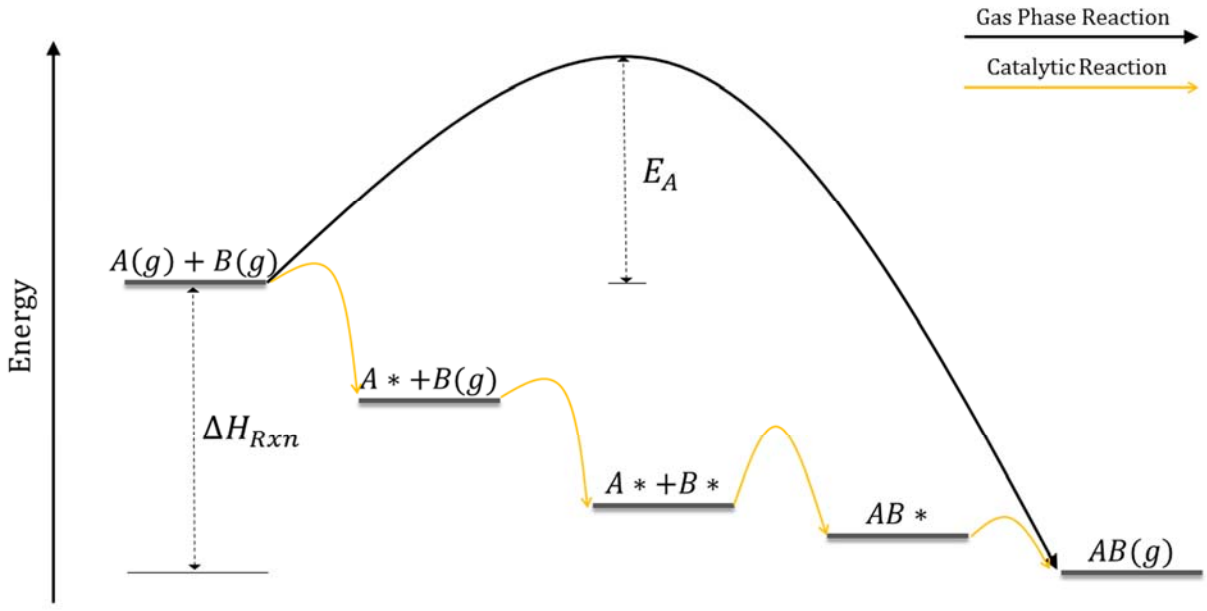

Figure 2.1. Potential energy surface for exothermic chemical reaction.

For example, if we assume the previously mentioned reaction $A + B \rightarrow AB$ proceeds on a catalyst surface following a Langmuir-Hinshelwood mechanism, we are interested in deriving an expression for the overall rate of reaction *r* in terms of the following elementary reactions summarized in Table 2.1.

Table 2.1. Rate expressions for A+B→AB reaction mechanism

Overall Reaction	$A(g) + B(g) \leftrightarrow AB(g)$	$r = k_f P'_A P'_B - k_r P'_{AB}$
Elementary Step 1	$A(g) + * \leftrightarrow A*$	$r_1 = k_{1f} P'_A[*] - k_{1r}[A*]$
Elementary Step 2	$B(g) + * \leftrightarrow B*$	$r_2 = k_{2f} P'_B[*] - k_{2r}[B*]$
Elementary Step 3	$A* + B* \leftrightarrow AB* + *$	$r_3 = k_{3f}[A*][B*] - k_{3r}[AB*][*]$
Elementary Step 4	$AB* \leftrightarrow AB(g) + *$	$r_4 = k_{4f}[AB*] - k_{4r} P'_{AB}[*]$

Since these elementary steps are reversible, we can represent the net rate of elementary step *j* as the difference between forward and reverse rates. These rates are dependent upon the forward and reverse rate constants (k_{jf} and k_{jr}) as well as the thermodynamic activities (effective concentrations) of chemical and surface species. Assuming the overall rate of reaction is controlled by a single rate limiting step, the *quasi-equilibrium approximation* can be applied to all other elementary steps thereby obtaining expressions for surface intermediate concentrations.

An overall rate expression can be evaluated by solving the expression for the rate limiting step. By treating the surface reaction (step 3) as the rate limiting step, Equation 2.3 can describe the rate of AB formation. Since steps 1, 2, and 4 are equilibrated, the difference between their forward and reverse rates is assumed to be negligible. Therefore the coverage (concentration) of a surface species I can be related to the partial pressure of the gas phase species through an equilibrium constant K_I, as defined in equation 2.4.

$$r = r_3 = k_{3f}[A*][B*] - k_{3r}[AB*][*] \quad (2.3)$$

$$K_I = \frac{[I*]}{[*]P_I'} \quad (2.4)$$

$$\frac{[A*]}{[*]} = K_A P_A' \qquad \frac{[B*]}{[*]} = K_B P_B' \qquad \frac{[AB*]}{[*]} = K_{AB} P_{AB}' \quad (2.5)$$

The total number of catalyst sites both empty and occupied is constant. An expression for the fractional coverage of empty surface sites $[*]$ can be evaluated by this site balance.

$$1 = [*] + [A*] + [B*] + [AB*] \quad (2.6)$$

$$[*] = \frac{1}{1 + \frac{[A*]}{[*]} + \frac{[B*]}{[*]} + \frac{[AB*]}{[*]}} = \frac{1}{1 + K_A P_A' + K_B P_B' + K_{AB} P_{AB}'} \quad (2.7)$$

Substituting in the expression for surface species coverages, the expression for the overall rate simplifies to Equation 2.7. Finally, the relative rates of forward (r_f) and reverse (r_r) rates can be determined by defining an approach to equilibrium, ζ. This term accounts for decreases in reaction rate resulting from chemical equilibrium. In the case of irreversible reactions, ζ becomes 0 simplifying the overall rate expression.

$$r = \frac{k_{3f} K_A K_B P_A' P_B' (1 - \zeta)}{[1 + K_A P_A' + K_B P_B' + K_{AB} P_{AB}']^2} = r_f (1 - \zeta) \quad (2.8)$$

$$\zeta = \frac{P_{AB}'}{P_A' P_B'} * \frac{1}{K_{eq}} = \frac{P_{AB}'}{P_A' P_B'} * \frac{K_4}{K_A K_B K_3} \quad (2.9)$$

Macroscopic parameters are determined by investigating the rate dependencies on temperature or partial pressures (activities). The overall reaction rate constant *k* can be determined from an Arrhenius plot of *ln r* against *1/T*. The slope of this line is proportional to the apparent

activation barrier. Rate order dependencies can be determined by evaluating the slope of *ln r* vs. *ln* a_i plots. We can then use the rate expression derived in equation 2.8 to predict these barriers and reaction orders (α_i) as a function of elementary reaction parameters using equations 2.10-11. The apparent activation barrier $H^{\ddagger}$ corresponds to the activation barrier for the overall reaction rate constant *k* used in equation 2.2.[1]

$$\frac{H^{\ddagger}}{RT^2} = \frac{\mathrm{d}\ln r}{dT} \qquad (2.10)$$

$$\alpha_i = \frac{d\ln r}{d\ln a_i} \qquad (2.11)$$

It is worth reiterating that these elementary rate constants (k_j), adsorbate equilibrium coefficients (K_I), and adsorbate coverages ($[I*]$) depend both on the reaction mechanism and on catalyst properties.

2.4. Microkinetic modeling of electrochemical reactions

Similarly, microkinetic analysis can be extended to electrochemical reaction mechanisms to understand how the overall reaction rates depend upon elementary steps. In electrochemical reactions, derivations are further complicated by the electrons' effect on system energetics.[2] Figure 2.2 shows the potential energy surfaces for a simple electrochemical process at different potentials. At equilibrium, the energies of reduced and oxidized states are equivalent with no net reaction. By increasing the electrochemical potential, the free energy of electrons are lowered, favoring oxidation. Conversely, lowering the electrochemical potential would favor the reduction. The free energy of the transition state, and therefore the activation barrier, is slightly affected by potential because it exists in a state between free and bound electrons. This energy is adjusted by a symmetry

factor β, a number between 0 and 1 indicative of how strongly the free energy of the transition state ($G^{\ddagger}$) depends on voltage.[3]

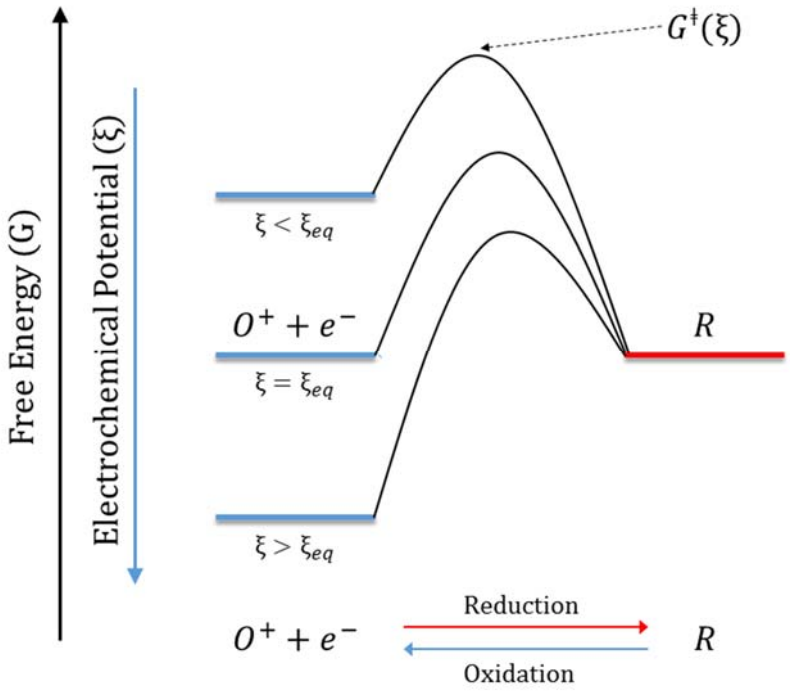

Figure 2.2. Potential Energy surface for an elementary electrochemical reaction.

Electrochemical kinetics are often described by the Bulter-Volmer equation, which relates the current i (the rate of electron formation/consumption) to electrochemical potential ξ. Throughout this thesis, positive currents will correspond to net oxidation rates while reduction rates will yield negative currents. Current is directly proportional to the overall rate of reaction, which is the difference between anodic and cathodic rates. Both oxidation and reduction rates have an exponential dependence upon potential. Specifically, these currents depend on the voltage difference between the applied potential and the equilibrium potential expressed by the Nernst equation.[3] This potential difference is often referred to as the overpotential (η). Negative overpotential promotes reduction while positive overpotential favors oxidation. When operating

at a potential far from equilibrium ($|\eta| >> 0$), contributions to current from one of the electrochemical reaction dominate.

$$i(\xi) = i_0 \left[\exp\left(\frac{\alpha_a nF}{RT} (\xi - \xi_{eq}) \right) - \exp\left(\frac{-\alpha_c nF}{RT} (\xi - \xi_{eq}) \right) \right] \qquad (2.12)$$

Current also depends upon temperature (T), number of electrons involved in transfer (n), Faraday (F) and gas (R) constants, the charge transfer coefficient (α), and the exchange current (i_0). The charge transfer coefficient is analogous to the activation barrier in a thermochemical reaction. It describes how changes in voltage affect the rates of anodic or cathodic currents. It is similar to the symmetry factor which describes elementary electrochemical reactions except the charge transfer coefficient is not limited between 0 and 1. The exchange current relates to the rate of forward and reverse reaction at equilibrium potential ξ_{eq}. Both charge transfer coefficients and exchange current depend upon electrocatalyst properties. Better performing electrodes will have higher current density and greater charge transfer coefficients.

Microkinetic modeling can also be applied to electrochemical reactions to understand how experimental parameters depend upon different elementary steps. This analysis can demonstrate why the apparent charge transfer coefficient changes with potential on Pt surfaces performing oxygen reduction. Often, the relationship between current and potential are plotted on a Tafel plot, where x and y axes correspond to $log\ |i|$ and η. The slope of this line (Tafel slope) corresponds to the change in overpotential required to improve current 10-fold and is inversely proportional to the charge transfer coefficient. Previously, microkinetic modeling has shown how changes in the apparent activation barrier can result from changes in the relative coverages of surface intermediates.[1] A similar phenomenon occurs on Pt electrocatalysts. At low potentials when the Pt surface is free of adsorbates, the Tafel slope is about -120 mV/decade. At higher potentials when

OH coverages become significant, the Tafel slope becomes -60 mV/decade.[4–7] Our group has performed microkinetic analysis on the ORR to determine the likely mechanism and rate-limiting steps by investigating the rate dependence on potential.[2] For brevity, only one mechanism will be presented in this chapter, however other mechanisms were also investigated.

$$O_2 + H^+ + e^- + * \rightarrow OOH* \quad (2.13a)$$

$$OOH* + * \rightarrow OH* + O* \quad (2.13b)$$

$$O* + H^+ + e^- \rightarrow OH* \quad (2.13c)$$

$$2\,(OH* + H^+ + e^- \rightarrow H_2O + *) \quad (2.13d)$$

Examining the proposed ORR mechanism in equation 2.13, the overall rate expression can be derived assuming one elementary step is rate limiting and all other steps are quasi-equilibrated. The apparent charge transfer coefficient can be determined by differentiating the rate expression with respect to potential. Analysis of these derivatives shows that the apparent charge transfer coefficient can be described by equation 2.14.[2] The first term of equation 2.14 corresponds to the potential dependence of the free energy of the transition state of the rate limiting step. The second term is related to the free energy of formation of reactant species of the rate limiting step. The third term corresponds to the free energy required to clean the surface sites of all species for the rate limiting reaction to occur. This expression is very similar to the general expression for apparent activation barriers shown in equation 2.15.[1]

$$\alpha = \beta n_{RLS} + \frac{1}{\upsilon}\sum_{RLS-reactants} n_i^f + N_* \sum_{adsorbates} n_i^{des}\theta_i \quad (2.14)$$

$$H_{app}^{\ddagger} = H_{RLS}^{\ddagger} + \frac{1}{\upsilon}\sum_{RLS-reactants} \Delta H_i^f + N_* \sum_{adsorbates} \Delta H_i^{des}\theta_i \quad (2.15)$$

Expressions for the apparent charge transfer coefficient α can be obtained assuming a particular elementary step is rate-limiting using equation 2.14. These expressions (shown in Table 2.2) can be evaluated as a function of intermediate coverages. At different electrochemical potentials, the relative coverages of different surface species can change, potentially leading to changes in the apparent charge transfer coefficient (or observed Tafel slopes). Assuming a symmetry factor of ½ and evaluating the Tafel slope on a clean electrode surface, the rate limiting step must either be the first proton/electron transfer to O_2 or be the chemical dissociation of O_2 in order to generate Tafel slopes greater than 100 mV/decade. On polycrystalline platinum electrodes, the Tafel slope changes from -60 mV/dec at high potentials characterized by high OH coverage ($\theta_{OH} = 1/3$) to -120 mV/dec at lower potentials where the Pt electrode is free of adsorbates ($\theta_* = 1$).[2] The ORR mechanism that best supports the Tafel behavior reported on Pt electrocatalysts is the pathway presented in equation 2.13, where the rate limiting step is the initial reduction reaction.[2]

Table 2.2. Apparent charge transfer coefficients assuming different elementary rate limiting steps.[2]

Rate Limiting Step	Apparent Charge Transfer Coefficient	Tafel Slope ($\theta_* = 1 \mid \theta_{OH} = \frac{1}{3}$)
$O_2 + H^+ + e^- + * \rightarrow OOH*$	$\beta_1 + \theta_{OH} + 2\theta_O + 3\theta_{OOH}$	120 / 72
$OOH* + * \rightarrow OH* + O*$	$1 + 2\theta_{OH} + 4\theta_O - 2\theta_{OOH}$	60 / 36
$O* + H^+ + e^- \rightarrow OH*$	$\beta_3 + 2 + \theta_{OH} - 2\theta_O - \theta_{OOH}$	24 / 21
$OH* + H^+ + e^- \rightarrow H_2O + *$	$\beta_4 + 1 - \theta_{OH} - \theta_{OOH}$	40 / 51

Tafel analysis studies of ORR activity on low Miller index Ag electrodes show shifts from -120 mV/dec at low overpotential to -70-100 mV/dec at higher overpotential on different Ag

facets.[8] OH coverage on silver electrodes has a weaker potential dependence compared to platinum electrodes, leading to less dramatic changes in Tafel slope. The high Tafel slope at low overpotentials on Ag is consistent with the ORR mechanism on Pt, where O_2 is the rate limiting step on a clean surface. Due to weaker interactions with OH on Ag, however, surface poisoning by OH on Ag is less of a problem than it is on a Pt surface. Further mechanistic insight can be gained by investigating the rate order dependence of ORR activity on pH and O_2 partial pressure. These results further validate our proposed ORR mechanism on Pt and Ag surfaces.

2.5. Chemisorption trends on catalytic surfaces

The interactions between adsorbates and a catalytic surface govern its catalytic activity. For many reactions, catalysts obey the Sabatier principle in which optimal catalytic behavior is achieved by materials that interact with reactants just strongly enough to activate the chemical transformation and yet interact with products weakly enough so that they are easily removed, increasing the availability of surface sites.

Early experimental work by Brønsted, Evans, and Polanyi have shown that activation barriers tend to linearly scale with heats of reaction.[9,10] These relationships have been shown to hold for elementary reactions on catalytic surfaces. Similarly, the adsorption energies of stable reactive intermediates have been shown to scale linearly, especially in the case of adsorbates that bind to the surface through the same central atom. As a consequence of these linear scaling relationships, the catalytic activity on different surfaces can be described by the adsorption energy of a key intermediate.[11,12] Slight changes to this chemical descriptor can have significant effects on catalytic performance.[13,14]

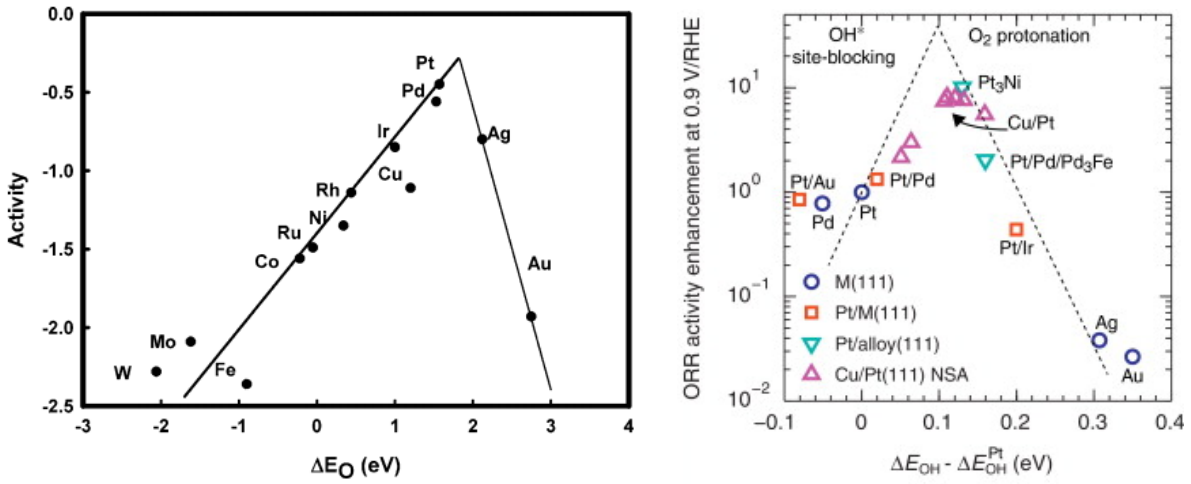

Figure 2.3. a) Volcano curve relationship of ORR activity on metal surfaces and O adsorption energy.[15] b) ORR activity of (111) alloy surfaces as a function of OH binding energy.[10]

Figures 2.3 demonstrate the volcano curve relationship between catalytic activity and a chemical reactivity descriptor. In Figure 2.3a, calculated ORR rates on different 111 metal surfaces is shown as a function of O adsorption energy.[15] It is clear that simply changing the element is not the best approach to maximize activity. In Figure 2.3b, measured ORR rates on various 111 alloy surfaces is shown as a function of OH adsorption energy.[10] Both activities and adsorption energies are normalized relative to the Pt(111) surface. Metals such as palladium (Pd) that bind OH stronger than Pt tend to show lower activities because of high OH coverages. Metals like silver and gold that bind OH much weaker than platinum tend to bind OH and O_2 too weakly, and therefore the ORR reaction rate is limited by these surfaces' ability to activate O_2. Alloying metals has been shown to be a promising way of selectively tuning the activity through manipulation of a chemical descriptor. The difficulty lies in understanding how changes in the nature of catalytic sites affect activity, so that promising alloy materials can be identified.

The d-band model has been extensively used to describe the trends in adsorption energies observed on transition metal and alloy surfaces.[16–18] This model relates relative differences in

adsorption energy to the electronic properties of surface atoms specifically the *d*-band structure. When molecules approach the surface, molecular orbitals first interact with valence *sp* electrons forming a stable surface bond. All *sp* bands of transition metals have similar structure therefore adsorbate-*sp* interactions will be identical. Differences in adsorption energies on these surfaces result from interactions with *d*-band states.

The *d*-band shape center (ε_d), width (W_d), and filling (*f*) are all strong functions of the element's position on the periodic table and its local chemical environment. Comparing elements within the same period (or row), lighter elements have fewer *d* electrons (smaller *f*), larger spatial extent of *d* orbitals (larger W_d), and higher *d*-band centers. Elements within the same group (column) have the same filling, but larger spatial extent of *d* orbitals, which increases W_d and decreases ε_d. Higher *d*-band centers are typically correlated with stronger adsorption energies because coupling between ads-*sp* state and high energy *d*-band leads to minimum population of ads-*d* antibonding states. This model helps explain periodic trends that chemical reactivity increase moving up and left in the periodic table. Adsorbates that follow this model typically have shorter surface bond distances resulting from stronger adsorption energies.

Unfortunately, the *d*-band model breaks down for electronegative adsorbates such as OH on surfaces with a filled or nearly-filled *d*-band like Pt and Pd skin alloys.[12] In these surfaces, the addition of elements into the subsurface layer induces both a shifting of *sp* electron density and *d*-band center. Electronegativity differences affect the adsorbate-surface bond distance and the *d*-*d* coupling changes the *d*-band width, which in turn shifts the *d*-band center since filling does not change.[13] Surfaces that exhibit weaker adsorption energies have high ε_d and short bond distances, which contradicts expectations from the *d*-band model. Interactions between highly electronegative adsorbates and surfaces have unfavorable interactions with *d*-states because their

repulsive term dominates adsorbate-*d* band coupling. A simple electron counting argument can be employed to identify adsorbate-skin alloy systems that follow or contradict *d*-band model predictions. Adsorbates gain 1 e^- by interacting with *sp* electrons before coupling with *d*-states. If either the adsorbate valence shell or surface *d*-band is filled, the coupling with *d*-states will be unfavorable, therefore the *d*-band model does not apply.

When designing ORR electrocatalysts, the differences in electronegativity must be accounted for on Pt and Ag based alloy electrocatalysts since the binding energies of OH (and O for silver) do not follow the simple *d*-band model treatment.

2.6. Conclusion

This chapter provides important insight into how elementary steps impact the overall reaction rates on catalytic surfaces. The catalytic activity of a material depends upon the strength of its interactions with adsorbate and product species. Difference in adsorption energies can be explained by the electronic structure of the material. Finally, the development of a superior ORR catalyst requires a slightly weaker OH-surface bond relative to a Pt(111) surface and a more reactive surface than Ag(111).

2.7. References

1. Lynggaard, H., Andreasen, A., Stegelmann, C. & Stoltze, P. Analysis of simple kinetic models in heterogeneous catalysis. *Prog. Surf. Sci.* **77,** 71–137 (2004).
2. Holewinski, A. & Linic, S. Elementary Mechanisms in Electrocatalysis: Revisiting the ORR Tafel Slope. *J. Electrochem. Soc.* **159,** H864–H870 (2012).
3. Bard, A. & Faulkner, L. Electrochemical Methods: Fundamentals and Applications, New York: Wiley, 2001. *Russ. J. Electrochem.* **38,** 1505–1506 (2002).
4. Murthi, V. S., Urian, R. C. & Mukerjee, S. Oxygen Reduction Kinetics in Low and Medium Temperature Acid Environment: Correlation of Water Activation and Surface Properties in Supported Pt and Pt Alloy Electrocatalysts. *J. Phys. Chem. B* **108,** 11011–11023 (2004).

5. Sepa, D. B., Vojnovic, M. V. & Damjanovic, A. Reaction intermediates as a controlling factor in the kinetics and mechanism of oxygen reduction at platinum electrodes. *Electrochim. Acta* **26,** 781–793 (1981).

6. Damjanovic, A. & Brusic, V. Electrode kinetics of oxygen reduction on oxide-free platinum electrodes. *Electrochim. Acta* **12,** 615–628 (1967).

7. Stamenković, V., Schmidt, T. J., Ross, P. N. & Marković, N. M. Surface Composition Effects in Electrocatalysis: Kinetics of Oxygen Reduction on Well-Defined Pt 3 Ni and Pt 3 Co Alloy Surfaces. *J. Phys. Chem. B* **106,** 11970–11979 (2002).

8. Holewinski, A. P. Kinetic Analysis of Electrochemical Oxygen Reduction and Development of Ag-alloy Catalysts for Low Temperature Fuel Cells. (Universiyt of Michigan, 2013).

9. Wang, S. *et al.* Universal Brønsted-Evans-Polanyi Relations for C–C, C–O, C–N, N–O, N–N, and O–O Dissociation Reactions. *Catal. Letters* **141,** 370–373 (2010).

10. Holewinski, A., Xin, H., Nikolla, E. & Linic, S. Identifying optimal active sites for heterogeneous catalysis by metal alloys based on molecular descriptors and electronic structure engineering. *Curr. Opin. Chem. Eng.* **2,** 312–319 (2013).

11. Viswanathan, V., Hansen, H. A., Rossmeisl, J. & Nørskov, J. K. Universality in Oxygen Reduction Electrocatalysis on Metal Surfaces. *ACS Catal.* **2,** 1654–1660 (2012).

12. Xin, H. & Linic, S. Communications: Exceptions to the d-band model of chemisorption on metal surfaces: The dominant role of repulsion between adsorbate states and metal d-states. *J. Chem. Phys.* **132,** 221101 (2010).

13. Xin, H., Holewinski, A. & Linic, S. Predictive Structure–Reactivity Models for Rapid Screening of Pt-Based Multimetallic Electrocatalysts for the Oxygen Reduction Reaction. *ACS Catal.* **2,** 12–16 (2012).

14. Xin, H., Schweitzer, N., Nikolla, E. & Linic, S. Communications: Developing relationships between the local chemical reactivity of alloy catalysts and physical characteristics of constituent metal elements. *J. Chem. Phys.* **132,** 111101 (2010).

15. Nørskov, J. K. *et al.* Origin of the overpotential for oxygen reduction at a fuel-cell cathode. *J. Phys. Chem. B* **108,** 17886–17892 (2004).

16. Hammer, B. & Norskov, J. K. Why gold is the noblest of all the metals. *Nature* **376,** 238–240 (1995).

17. Hammer, B., Morikawa, Y. & Nørskov, J. CO Chemisorption at Metal Surfaces and Overlayers. *Phys. Rev. Lett.* **76,** 2141–2144 (1996).

18. Hammer, B. & Nørskov, J. K. Electronic factors determining the reactivity of metal surfaces. *Surf. Sci.* **343,** 211–220 (1995).

Chapter 3

Theoretical and Experimental Methods

3.1. Summary

This chapter is a brief overview of various theoretical and experimental methods utilized during this project. The general theory and application of these techniques are designed to provide the reader with a basic understanding necessary to interpret the results presented in later chapters. More detailed descriptions of specific experimental conditions are located in these chapters. The chapter is organized in four sections: density functional theory calculations, electrochemical methods, nanoparticle synthesis strategies, and characterization techniques.

3.2. Density Functional Theory

Density Function Theory (DFT) is an invaluable tool to calculate and compare adsorption energies, electronic properties, and transition state energies for chemical reactions on different catalytic surfaces. The DFT formalism will not be discussed in great detail here, but there are a number of great references on the topic.[1–4] In general, DFT calculations solve Schrödinger's equation for a collection of atoms and moves their positions accordingly to minimize the total system energy. Instead of solving the many body problem for all of the single electron wave functions, system energy is treated as functional of electron density. For a given system, more accurate electron densities lead to lower energies closer to the true ground state. Once the electron density is optimized for a given geometry, the energy and forces on individual atoms can be calculated. These forces can inform better positions for atoms ultimately leading to the discovery

of stable system configuration. The calculation is converged when energy steps and total force on atoms in the system are below thresholds specified in the calculation constraints.

In these studies, DFT was utilized to calculate relative adsorption energies on different alloy surfaces, determine the equilibrium lattice spacing of Au-Cu alloys, and project localized density of states to assess the electronic structure of different alloys. All calculation reported were performed in the atomic simulation environment using the plane wave mode GPAW calculator. The differential binding energy of adsorbate *ads* relative to Pt (111) surface was determined using Equation 3.1, where $E_{ads+slab}$ and E_{slab} correspond to total energies with and without adsorbate.

$$\Delta\Delta E_{ads} = \Delta E_{ads,slab} - \Delta E_{ads,Pt111} = (E_{ads+slab} - E_{slab}) - (E_{ads+Pt111} - E_{Pt111}) \quad (3.1)$$

Equilibrium lattice parameters for AuCu alloys were determined by calculating the energies of periodic fcc unit cells at different lattices. Energies were plotted as function of volume and fit to a 3rd order inverse polynominal in order to calculate the volume with minimum energy. The cube root of this volume yields the equilibrium lattice spacing. Finally, *d*-band centers and widths can be calculated from the first and second moments of the occupied density of states. These values were numerically calculated using Equations 3.2-3.

$$\varepsilon_d = \int_{-\infty}^{\varepsilon_f} n(\varepsilon)(\varepsilon - \varepsilon_f) d\varepsilon \quad (3.2)$$

$$W_d = \sqrt{\sigma_d^2} = \sqrt{\int_{-\infty}^{\varepsilon_f} n(\varepsilon)(\varepsilon - \varepsilon_f)^2 d\varepsilon} \quad (3.3)$$

3.3. Electrochemical techniques

There are many electrochemical techniques used to measure and understand current-potential relationships on electrocatalysts. The following sections will include a brief discussion of theory, application, and data analysis associated with different techniques that were used over the course of this project. All of these technique utilized a potentiostat/galvanostat, which is a device that can simultaneously measure the working electrode current while controlling its potential, or vice versa. Specific experimental details can be found in subsequent chapters.

3.3.1. Rotating disk electrode

Mass transport effects must be considered when measuring reaction rates. Slow transport of reactants to the catalytic surface (relative to surface reaction rate) will lower observed reaction rates making it difficult to compare intrinsic catalyst performance. To mitigate these effects, catalysts were tested in a three-electrode electrochemical cell in the thin-film rotating disk electrode (RDE) configuration. The three-electrode set-up enables oxygen reduction rates to be measured as function of cathode potential (relative to a reference) independent of anode performance. The rotating disk electrode allows kinetic rates to be decoupled from mass transport effects through the Koutecky-Levich equation, which relates measured current i to kinetic and mass transport limiting currents, i_k and i_L.[5]

$$\frac{1}{i(\xi)} = \frac{1}{i_L} + \frac{1}{i_k(\xi)} \qquad (3.4)$$

The Levich equation describes the mass transport limiting current as a function of experimental conditions: rotation rate (ω), reactant concentration (C), temperature (T), number of electrons transfer (n), electrode surface area (A), diffusivity of reactant in electrolyte (D), and kinematic viscosity (υ). The limiting current is the maximum achievable reaction rate typically

observed at high overpotential. The magnitude of i_L depends on the square root of the rotation speed.

$$i_L = 0.620nFAD^{\frac{2}{3}}\omega^{\frac{1}{2}}\upsilon^{-\frac{1}{6}}C = B\omega^{\frac{1}{2}} \quad (3.5)$$

Selectivity towards toward the $4e^-$ oxygen reduction can be assessed by performing Levich analysis to determine the number of electrons involved in the reaction. In Levich analysis, the limiting currents for several different rotation rates are plotted against the square root of rotation rate in units of rad/s. The slope of this line should be a constant *B* described in equation 3.5. Using the experimental parameters summarized in Table 3, *n* can easily be determined. Alternatively, the reciprocal of *i* can be plotted against $\omega^{-1/2}$ to give a linear relation at an operating potential with slope of $1/B$.

Table 3. Experimental Levich equation parameters for various electrolytes

Electrolyte	C O_2 (M)	D (cm^2/s)	*v* (cm^2/s)	B (mA/cm^2 $rad/s^{1/2}$)
0.1M $HClO_4$[6]	0.00138	0.000019	0.00997	0.507
0.1M $HClO_4$[7]	0.00126	1.93E-05	0.01009	0.467
0.1M $HClO_4$[8]	0.00122	1.93E-05	0.01	0.453
0.05M H_2SO_4[9]	0.00122	1.93E-05	0.01	0.453
0.1 M KOH[10]	0.00118	1.90E-05	0.01	0.433
1M KOH[11]	0.000843	1.43E-05	0.01128	0.251
0.1M NaOH[12]	1.26E-03	1.93E-05	1.09E-02	0.461
0.1M KOH[13]	1.21E-03	1.86E-05	1.01E-02	0.437

3.3.2. Linear Sweep Voltammetry

Linear sweep voltammetry (LSV) is a technique that measures the current at the working electrode as a function of its linearly changing potential. Throughout this dissertation, linear sweep voltammetry experiments will refer to the measurement of ORR currents with a RDE in O_2 saturated electrolyte. The potential of the working electrode will change linearly relative to some

standard reference electrode: Ag/AgCl (3M KCl-sat AgCl) in perchloric acid ($HClO_4$), Hg/HgO (1M KOH) in sodium hydroxide (NaOH) and potassium hydroxide (KOH), and Hg/Hg_2SO_4 (sat K_2SO_4) in sulfuric acid (H_2SO_4). These electrodes have stable well established potentials, which can be used to compare catalytic performance on similar potential scales. Since the equilibrium potentials for both hydrogen evolution/oxidation reactions and oxygen reduction/evolution shift to lower potentials on the standard hydrogen electrode (SHE) scale with increasing pH, ORR rates will be compared on the reversible hydrogen electrode (RHE) scale. Independent of pH, the equilibrium potentials for the hydrogen oxidation and oxygen reduction reactions are located at 0 and 1.23 V_{RHE}, respectively.

3.3.3. Cyclic Voltammetry

Similar to LSV experiments, cyclic voltammetry (CV) measures currents as the electrode potential is scanned back and forth between potential limits. Typically, CVs are used to measure the interactions between the electrolyte and catalytic surface. The magnitude of such interactions depends upon catalyst reactivity and surface area. To remove ORR contributions to measured currents, the solution is sparged with argon (Ar) gas to displace dissolved O_2 and CVs are measured without rotation. Sample capacitance and electrochemical surface area (ECSA) can be quantified by CV experiments.

Capacitance is a property related a material's ability to store charge. Since our electro-catalysts are deposited onto high surface area carbon support, we must account for capacitive currents that result from the charging/discharging of electrode surface as potential changes. Faster scan speeds and higher nominal carbon loading will increase capacitance effects. Consequently, there will be a larger current offset between anodic (forward) and cathodic (reverse) scans as shown in Figure 3.1. Equation 3.6 can be used to show this difference corresponds to i_{cap} which is

directly proportional to C amount and potential scan rate. Capacitance effects can be corrected by subtracting i_{cap} to currents of anodic sweeps ($dV/dt > 0$) and adding i_{cap} to currents of cathodic sweeps.

$$q = CV \Rightarrow i_{cap} = \frac{dq}{dt} = \frac{dCV}{dt} = \frac{CdV}{dt} \qquad (3.6)$$

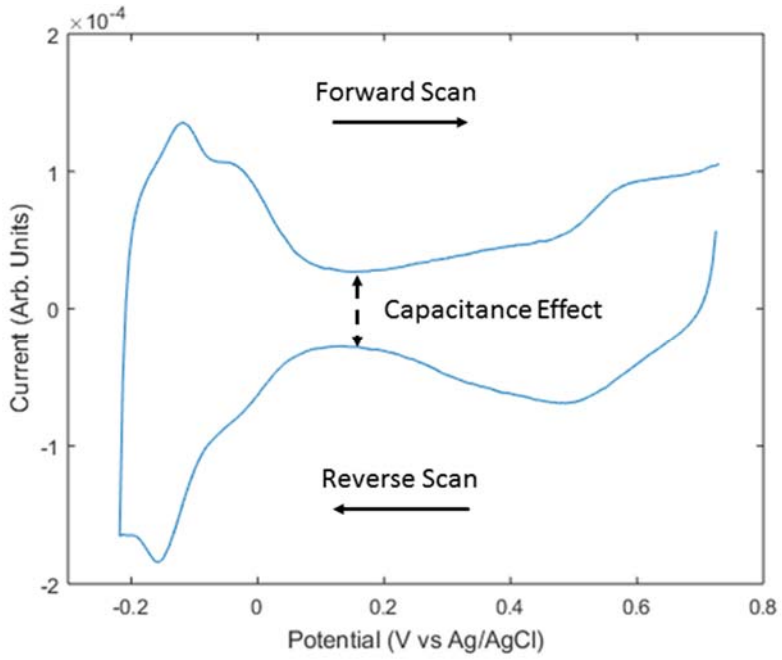

Figure 3.1. Typical cyclic voltammetry curve on Pt/C in 0.1M $HClO_4$.

Electrochemical surface area (active catalyst surface area) can also be measured by various cyclic voltammetry techniques. In general, a chemical probe is deposited onto the catalyst surface before being removed electrochemically. The current measures the rate of probe removal as function of potential (and time). Integration of this peak will quantify to total amount of charge associated with removing all probe molecules from the catalytic surface. This charge is directly proportional to ECSA, which can be easily determined with the appropriate conversion to cm^2

catalysts. As discussed in later sections, normalization of rates by catalyst surface area is required to accurately assess intrinsic catalytic activity across different samples.

3.3.4. Electrochemical Impedance Spectroscopy

Electrochemical impedance spectroscopy (EIS) is an electrochemical technique, which measures the response of an electrochemical system in response to an oscillatory potential or current function. Different processes in electrochemical systems can often be represented as circuit elements with characteristic parameters which affect overall system performance. EIS can be used measure the real and imaginary components of impedance ($Z=i/E$) as a function of AC signal. In this work, uncompensated resistance between working and reference electrodes was measured at the high frequency limit. This parameter was used to compensate for potential losses associated with solution resistance which is more pronounced at high currents.

3.3.5. Underpotential Deposition

Underpotential deposition (UPD) is a phenomenon characterized by the deposition of metal at monolayer or sub-monolayer coverages at a potential slightly above the bulk reduction potential. As previously discussed, typically reduction only occurs at potentials below the bulk reduction potential. However under specific conditions, it is more favorable for metal ions to deposit onto a substrate. In these processes, only a single atomic layer is deposited because bulk reduction remains unfavorable. This phenomenon is useful for measuring ECSA and epitaxially depositing atomic layers of different metals. Lead (Pb) has been shown to underpotentially deposit on Ag surfaces at sub-monolayer coverages. In this work, Pb_{UPD} was oxidized to measure Ag nanoparticle surface areas. Copper (Cu) underpotential has been well studied on Au electrodes. Since Cu is smaller relative to Au, a complete monolayer will form. This Cu_{UPD} layer can act as a sacrificial

template for the deposition of more noble metals such as platinum, palladium, gold, and silver by a galvanic replacement reaction during the preparation of Pt_{ML} electrocatalysts.

3.3.6. Data analysis for specific activity and normalized polarization measurements

This section will describe all the data processing steps required to produce Tafel polarization and normalized polarization curves. Data from a Pt/C experiment in 0.1M $HClO_4$ will be analyzed. First, voltage corrections are applied by shifting voltage to the RHE scale and correcting for uncompensated resistance effects. Capacitance corrections are applied to current by subtracting i_{cap}. Kinetic currents are measured as a function of potential using the Koutecky-Levich equation. When positive kinetic currents are measured, there is negligible ORR activity so the kinetic current (i_k) is set to $0\ mA$ at these potentials. Koutecky-Levich analysis breaks down as i approaches i_L so these potentials are not reported in Tafel plots. The nominal ORR activity (kinetic current) must then be normalized by the electrochemically determined ECSA to yield the kinetic current density j_k. Tafel plots compare the potential dependence of ORR rates by plotting $log\ |j_k|$ and ξ. In order to compare the relative activities of different catalyst samples using polarization curves, these samples must be compared on an equal surface area basis. Kinetic currents are directly proportional to ECSA so samples with higher ECSA will naturally show earlier activity onset compared to lower ECSA samples even though these samples might be less active on a surface area basis. Polarization curves can be compared on equal surface area basis by multiplying the kinetic current density by the electrode surface area A and calculating the normalized current i_N using the Koutecky-Levich equation. Finally, the normalized current is divided by electrode surface area to enable comparison of experiments with different sized RDEs.

3.4. Catalyst Synthesis

The activity of a catalytic surface site is a strong function of its local environment. The primary objective in a catalytic system is to maximize the availability of desired sites. Overall performance depends upon the collective behavior of all sites within the system. Therefore, strong control over the relative abundance of different sites is required for the development and assessment of meaningful structure-property relationships. Different synthetic approaches can be employed to selectively control the size, shape, and composition of catalytic nanoparticles informing the design of superior catalysts.

In recent years, there has been a wealth of novel chemical syntheses developed to create highly monodisperse populations of metal nanoparticles with specific morphology and compositional structure. In this section, general synthesis approaches for the shape-selective and alloy nanoparticle synthesis as well as their challenges will be briefly described. Specific experimental details can be found in the methods section in later chapters or appropriate references.

3.4.1. Control of Nanoparticle Shape and Size

The size and shape of nanoparticles control the relative distribution of surface atoms with differing coordination. Less coordinated sites are typically less stable and more chemically reactive than defect-free terrace sites. For example, only Au nanoclusters show any reactivity towards CO oxidization, unlike their bulk materials. Judicious selection of solvent, metal precursor, reducing agent, capping agents, and experimental conditions can lead the preferential formation of nanoparticles with desired morphology.

Relative sizes of nanoparticles are largely governed by the rate of precursor reduction and particle nucleation, which are strong properties of reductant strength and precursor concentration. Nanoparticle formation can be treated as a series of sequential reactions where metal precursor M^+

is first reduced to form a solvated metal atom M^0, which combines with other atoms to form a nanoparticle. Figure 3.2 depicts the relative concentration of metal clusters over reduction time. Initially, there is a rapid reduction rate until the concentration of M^0 becomes high enough that nucleation begins. Typically fast reduction processes create many nucleation centers leading to a large number of small particles. A slow reduction rate creates fewer seeds so leading the growth are larger nanoparticles. After all of the precursor has been reduced, nanoparticles and clusters can undergo Ostwald ripening and other dissolution/deposition mechanisms to change relative particle sizes to minimize total free energy.

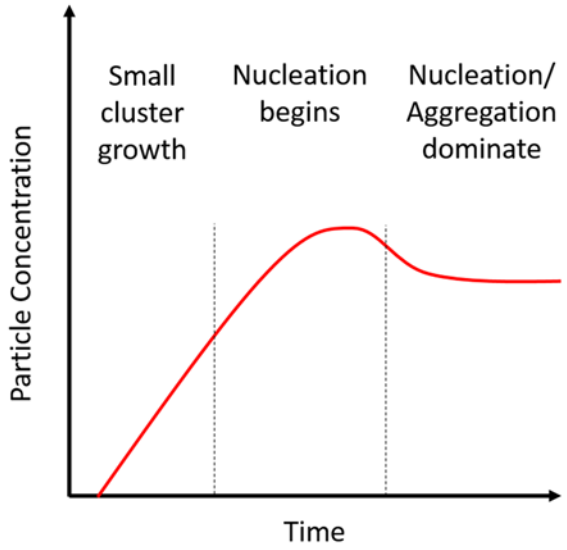

Figure 3.2. Concentration profile of reduced clusters during a chemical synthesis.

The shape selective synthesis of metal nanoparticles requires the use of chemical additives (capping agents) to preferentially stabilize particular termination facets. The presence of capping agents promote the growth and diffusion of atoms on other surfaces eventually creating morphology terminations in the preferred surface facet. Thermodynamics ultimately determines nanoparticle morphology by forming particles that minimize free energy. Without capping agents, quasi-spherical nanoparticles covered by low Miller index surfaces form because spheres

maximize the number of high-coordinated atoms within the core and minimizing surface atoms. In the case of silver nanocubes, a capping agent (polyvinylpyrrolidone, PVP) interacts strongly with the Ag (100) terrace sites enabling the formation of particles primarily terminated by these sites. Removing capping agents or changing solvent can induce irreversible changes to more stable configurations.

3.4.2. Control of Alloy Nanoparticle Structure

There is a wide array of synthesis strategies to create alloy nanoparticles with different structures. Depending upon the desired structure and properties of constituent elements, different strategies of precursor addition and reduction should be employed. These structures will each have distinct properties which are dependent upon a simple combination of the properties of the pure metal components. The relative difference in reduction potentials and miscibility of the metals largely affect structure.

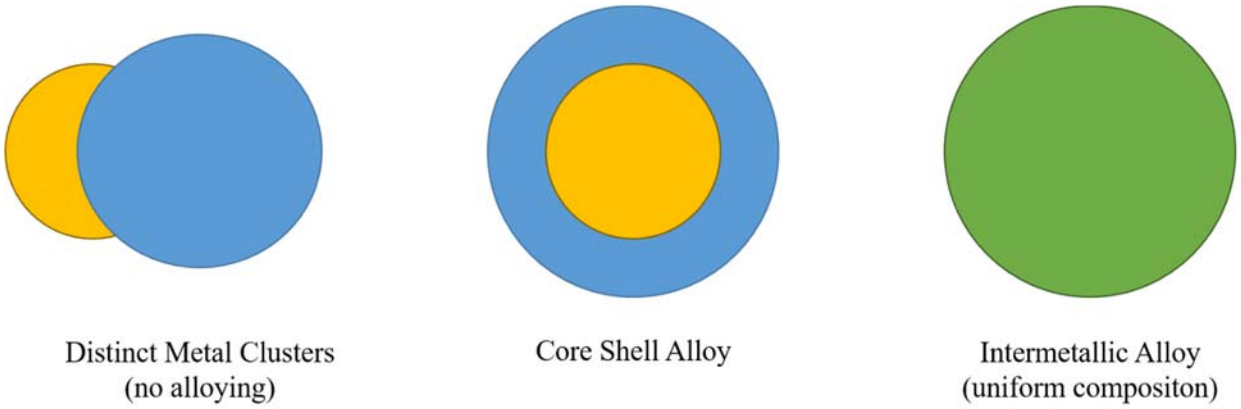

Figure 3.3. Representations of different alloy nanoparticle structures

Co-reduction of metal precursors in solution produce an assortment of different particle structures depicted in Figure 3.3. Co-reduction of immiscible metals with a strong reducing agent will form distinct nanoparticles or clusters. Highly miscible metals will easily form homogeneous alloys where constituent elements are perfectly mixed. If one metal is more easily reduced, it is

possible to form core-shell particles in which the more noble metal populates the core while the other metal deposits on surface layers.

Alternatively, core-shell particles can be prepared by a seed-mediated method in which previously prepared nanoparticles act as substrate on which a second metal deposits. Galvanic replacement (electro-less deposition) occurs when ions of a metal with high reduction potential contact a metal that is more easily oxidized. A spontaneous redox reaction occurs to deposit the more noble metal by dissolving the more reactive metal. This reaction can be mitigated by using a strong reducing agent which reduces metal before dissolution of the core can occur.

Fast reduction of a bimetallic precursor can be used to prepare alloys between very immiscible elements. In this approach, compatible metal precursors are combined to form an ionic matrix containing multiple metals. The precursor is rapidly reduced and quenched before segregation of elements can occur. This technique has been employed in the preparation of Au-3*d* and Ag-3*d* metal alloys.

Finally, the local composition of elements in near-surface layers can be manipulated through different conditioning protocols. In Pt-3*d*, electrochemical etching with subsequent thermal treatment causes surface layers to become Pt rich.[14,15] Additionally, diffusion of selected elements can be induced by strongly interacting adsorbates. Heating a PtCu electrode in a CO environment leads to diffusion of Pt to surface.[16] Similarly heating in an inert, reducing, or oxidizing environment can induce various surface reconstructions in alloys.[17] A variety of these synthesis approaches were utilized throughout this work, but colloidal syntheses offers the greatest control.

3.5. Characterization Techniques

Since the structure of catalytic sites largely governs the performance of heterogeneous catalysts, many analytic and spectroscopic techniques were used to verify the bulk and surface structure of nanoparticle catalysts. In the following sections, the general theory and basic applications of each technique is briefly discussed. Specific data analysis relevant to our research will be described in greater detail in later chapters.

3.5.1. UV-visible spectroscopy (UV-vis)

UV-visible light spectroscopy (UV-vis) is a technique to measure different optical properties such as extinction (scattering and absorption) and transmission of a sample as a function of a particular wavelength of light. Operating in transmission mode, the spectrophotometer uses a diffraction grating to filter photons of a particular wavelength. This light is sent through the sample chamber and the intensity of transmitted light is measured with a CCD detector and recorded. If there is a sample in the path of the beam, there will be a drop in transmission because some of the light will either be scattered or absorbed. Extinction (E), which results from of all these scattering and absorption events, can be measured by comparing the transmission of light through the sample (T) with the initial beam intensity (T_0). An alternative definition for extinction is Beer's Law (also shown in equation 3.7), where intrinsic extinction coefficient ε, *b* is the path length, and *c* is the concentration of adsorbing/scattering species.

$$E = -\log\left(\frac{T}{T_0}\right) = \varepsilon bc \quad (3.7)$$

In this research, UV-vis spectroscopy is used to compare the optical properties of different samples containing suspensions of plasmonic nanoparticles. Coinage metal (Au, Ag, and Cu) nanoparticles are known to exhibit localized surface plasmon resonance (LSPR) in the visible light region.[18] This phenomena occurs when light, which is an electromagnetic wave, interacts with

loosely-held *sp* electrons in the nanoparticle to displace the electrons from their equilibrium positions relative to atomic nuclei. These electrons experience a restorative Coulombic force promoting system relaxation. Particular frequencies, or wavelengths, of light can induce standing waves of oscillating free electrons increasing the extinction of those photons. The size, shape, composition, and local environment greatly impact the optical properties of plasmonic particle samples.[18–21] To isolate contributions from plasmonic nanoparticles, sample data is measured relative to the extinction of pure solvent in sample cuvette at identical measurement conditions. Due to slight differences in absolute extinction resulting from differences in concentration, normalized extinction data is often used to compare UV-vis spectra from different samples. In this work, UV-vis experiments were used to monitor the size and shape of different Ag nanoparticle and the relative composition in AuCu alloy nanoparticles following synthesis and centrifugation.

3.5.2. Raman spectroscopy

Raman spectroscopy is a technique used to measure vibrational modes present in a sample. Raman spectroscopy is complementary to Fourier transform infrared spectroscopy (FTIR). Unlike FTIR, which is selective to asymmetric vibrations that cause changes in the dipole moment, Raman spectroscopy is selective towards symmetric vibrations that cause changes in the polarizability of the molecule. This technique employs high intensity lasers to excite a population of molecules to a short-lived virtual state. The vast majority of molecules then relax back to their original vibrational state, elastically scattering the photon with the same energy as the incident wavelength. This process is known as Rayleigh scattering. However, a few molecules will relax from the virtual state to an excited vibrational state ($\Delta v = 1$) releasing a photon with slightly less energy shifted by the energy equivalent to the excited vibrational mode. Vibrational spectra are obtained by detecting inelastically scattered electrons.

In this work, we utilized surface-enhanced Raman spectroscopy (SERS) to identify species chemically bound to the surface of a catalyst. Compared to traditional Raman experiments, SERS can greatly enhance the measured Raman signal by many orders of magnitude.[22,23] Previously, our group has shown plasmonic nanoparticles can be used to enhance particular vibrational modes by concentrating both Rayleigh and Stokes scattered light near the particle surface, making SERS a strong probe for identifying adsorbed compounds.[19] In this work, SERS was used to identify the presence of surface capping agents used in the colloidal synthesis of catalytic nanoparticles.

3.5.3. Inductively coupled plasma optical emission spectroscopy

Inductively coupled plasma optical emission spectroscopy (ICP) is an analytic technique for identifying trace amounts of dissolved metals in solution. In this technique, the analyte is injected into a chamber containing Ar plasma. Upon addition, electrons and ions collide with metal atoms from the analyte to emit photons with energies characteristic of specific electronic transitions. The atomic emission spectrum is specific to each element and the signal intensity is directly proportional to its concentration. Using an optical spectrometer to measure the intensity of characteristic wavelengths, the concentration of an individual element can be determined by comparing the signal intensity against standard solutions with known concentration.

ICP samples are prepared by dissolving catalysts in strong acid (concentrated nitric acid for Ag and aqua regia for Pt and Au alloys). These concentration solutions are often diluted (10-fold) to prevent acids from reacting with plastic sample vessels (15mL centrifuge tubes). Standard solutions used to generate calibration curves relating the intensity of emission peak to the concentration of a particular element. Yttrium (1 – 2 ppm Y) solution was added to all solutions as an internal standard. We utilize this technique to determine the relative composition of different elements in alloy nanoparticles as well as estimating the weight loading of metals on the support.

X-ray diffraction

X-ray diffraction (XRD) crystallography is a characterization technique capable of identifying bulk structural properties of a material by examining the diffraction patterns of elastically scattered x-rays. In this technique, the sample (typically pressed pellet of powder) is irradiated with a monochromatic x-ray source and x-ray intensity is measured as a function of the grazing angle (θ) parallel to the sample plane. Scattered x-rays can undergo either constructive or destructive interferences depending upon the spacing of different crystal planes. Only constructively-scattered x-rays generate measureable signal at specific angles. Structural properties such as lattice spacing or crystal symmetry affect the position and relative intensity different diffraction peaks. If the symmetry or space group of the material is known, the lattice parameter can be determined from experimental data using Bragg's law (equation 3.8), where λ is the wavelength of incident x-ray, θ is the scattering or grazing angle, and *d* is the spacing between crystal planes. The interatomic plane spacing *d* is relating to the lattice parameter *a* through the miller indices parameters (*hkl*) as described in equation 3.9.

$$\lambda = 2d \sin\theta \qquad (3.8)$$

$$d = \frac{a}{\sqrt{h^2 + k^2 + l^2}} \qquad (3.9)$$

Experimental x-ray diffraction patterns can also be compared with standards in various databases to identify the relative abundance of different materials or phases present in the sample. In this work, XRD is used to measure relative expansion or compression of lattice parameters in different AuCu nanoparticles compared to pure Au and Pt samples.

3.5.4. Electron microscopy

Electron microscopy is a powerful characterization technique enabling the characterization of materials on very small length scales. Electron microscopes operates similarly to typical optical microscopes except rather than using light, electrons are used to image samples in electron microscopes. Since the characteristic wavelength of energetic electrons is much smaller than the wavelength of light, electrons can be used to image nanoparticle and atomic features that are too small to be imaged with visible light. There are different operating modes in electron microscopy, but transmission and scanning transmission electron microscopy will be briefly described below.

In transmission electron microscopy (TEM), the electron beam is focused using a series of electromagnetic lenses as it travels down the optical axis. The majority of the beam is able to pass through thin TEM samples since atoms are largely composed of empty space, making collisions infrequent. In bright field mode, the transmitted (unperturbed) electrons are used to image the sample. In these images, the background appears bright due to the high signal of transmitted electrons. Differences in intensity arise when electrons must travel through thicker or denser materials, which are more likely to scatter or absorb electrons compared to the background. Alternatively, images can be generated by collecting only scattered electrons. In these dark field images, only areas that scatter electrons appear bright while the background remains dark. The size, shape, and intensity of the electron beam can manipulated by changing lens properties. Special care must be taken to avoid creating distortions when moving the beam (relative to sample), changing magnification, or changing positions of various detectors and apertures. TEM is very useful for imaging collections of nanoparticles to assess the distribution of particle sizes or morphology. In this work, TEM is used to characterize nanoparticles of different shape, size, and composition before and after testing.

Scanning transmission electron microscopy (STEM) is similar to TEM except the electron beam has been focused into a small probe (~1 Å width), which is used to image the surface. The probe quickly scans the field of view to generate bright and dark field images, typically at slightly higher resolution and magnification compared to conventional TEM. When analyzing heavy elements such as Au or Pt, sometimes a high angle annular dark field (HAADF) detector is required to image the sample using highly scattered electrons. Additionally, atomic resolution of particles can be obtained using aberration-corrected STEM. These corrections account for high order perturbations in the probe shape induced by non-idealities in the electromagnetic lenses. Accounting for spherical aberrations enables higher resolution imaging on nanoparticles and small clusters as shown in Figure 3.4.

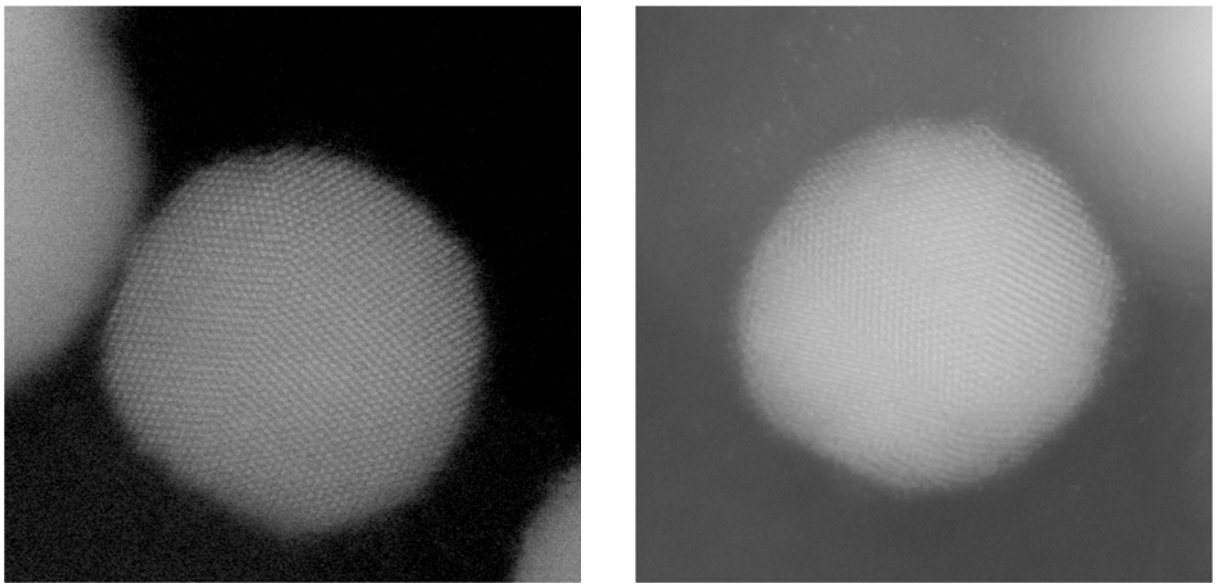

Figure 3.4. Aberration-corrected HAADF-STEM micrographs of Pt alloy electrocatalysts.

STEM can also be coupled with spectroscopic techniques such as electron energy loss spectroscopy (EELS) and energy-dispersive x-ray spectroscopy (EDS) to identify elemental distributions within the sample. EELS measures the frequency of inelastically scattered electrons, specifically collisions causing core level excitations since these transitions strongly depend on the

element. Unfortunately, similarities between Au and Pt EELS spectra make it difficult to distinguish these two elements. EDS is a complementary technique to EELS for identifying elemental structure in materials. As discussed for EELS, the highly-energetic electrons in the beam can inelastically scatter with core-level electrons creating a vacancy or hole. An electron from a higher energy level can fill the hole simultaneously relaxing a high-energy photon (x-ray) characteristic to that electronic transition. In EDS, the relative abundance of these x-rays is used to determine the relative abundance of different atoms. In this work, aberration-corrected STEM-EDS was used to verify the core-shell structure of Pt alloy electro-catalysts.

3.5.5. X-ray photoelectron spectroscopy

X-ray photoelectron spectroscopy (XPS) is a surface sensitive chemical analysis technique in which an x-ray source irradiates a sample to eject electrons. XPS measures the number and kinetic energy of photo-emitted electrons to identify the abundance of different elements. The kinetic energy is sensitive to the local environment. Slight differences in ionization energy can be used to identify different oxidation states present at surface layers. In this work, XPS was performed to measure sulfur (S) concentration on supported Ag nanoparticles.[24]

3.5.6. X-ray absorption spectroscopy

X-ray absorption spectroscopy (XAS) is used to gather electronic and geometric information about the structure of a material by measuring changes in the x-ray absorption as a function of energy. XAS experiments require intense and tunable x-ray sources available at synchrotron sources. Using a similar design to UV-vis experiments, the transmission or fluorescence of x-rays can be measured as a function of energy relative to intensity of incident x-rays irradiating the sample. Increased x-ray absorption corresponds to the excitations of core-level electrons of a particular atom, which is also dependent upon sample thickness. Figure 3.5 shows a

typical XAS spectra for Pt foil sample. The sharp increase in signal around 11565 eV is referred to as the Pt L_3 because it arises from a Pt $2p_{3/2}$ e^- excitation. Examination of the near edge structure or (XANES) region gives important insight into chemical information of excited atoms. The edge location and peak shape are strongly dependent upon the oxidation state and the degeneracy of unoccupied states above the Fermi level available for the excited electron. Structural information can be gained by studying the oscillations in the extended far-edge (XAFS) region. These oscillations result from scattering of x-rays with neighboring atoms. After properly normalizing XAS data (accounting for thickness effects), the data can be fit using modeling software to determine bond distances, coordination number, and local geometry of the excited atom.

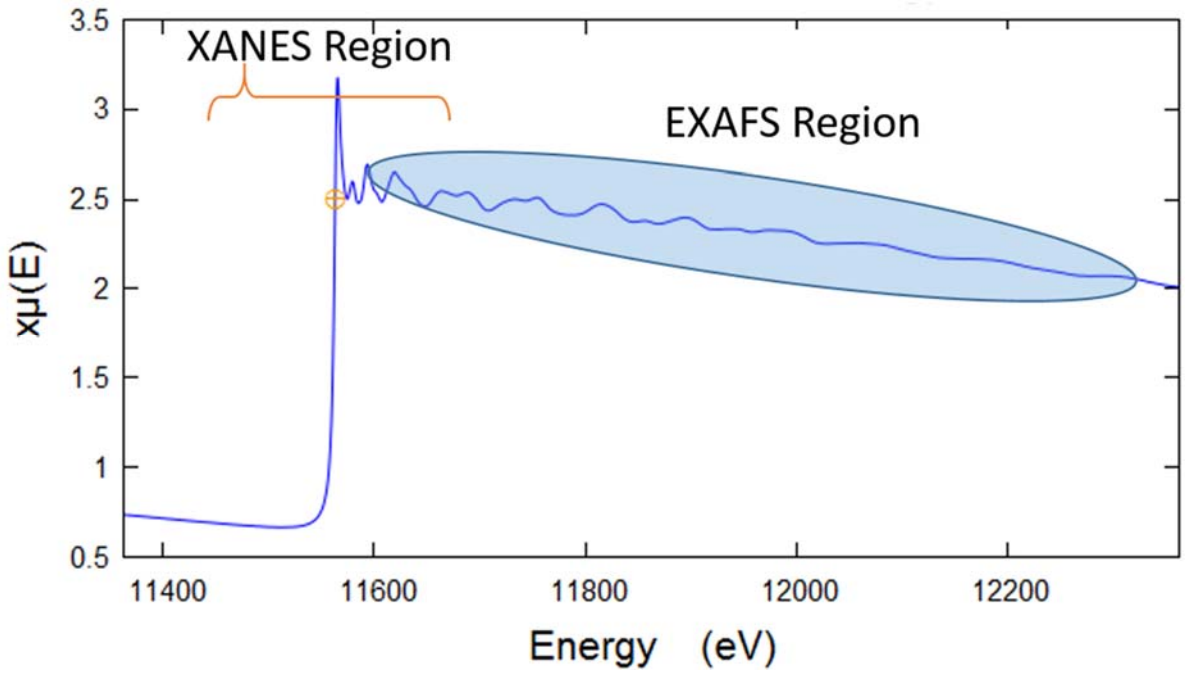

Figure 3.5. X-ray absorption spectra of Pt metal foil.

In this work, all experiments were performed at the Advanced Photon Source (APS) located at Argonne National Laboratory. Specifically, we were interested in studying the Pt L_3 and Au L_3 edges located at 11564 and 11919 eV of Pt alloy electrocatalysts. All experiments were carried out in fluorescence mode using Ar ion detection chambers at the ID-10B beamline hutch.

XAS data was normalized using the Athena software package. Artemis was used to perform Feffit calculations and data fitting analysis. Details regarding the proper implementation of these programs can be found at the following references.[25–27]

3.6. References

1. Kitchin, J. *Modeling materials using density functional theory*. (2012). at <http://kitchingroup.cheme.cmu.edu/dft-book/dft.pdf>
2. Asthagiri, A. & Janik, M. J. *Computational Catalysis*. (Royal Society of Chemistry, 2013). at <https://books.google.com/books?id=qHZIAgAAQBAJ&pgis=1>
3. Sholl, D. & Steckel, J. A. *Density Functional Theory: A Practical Introduction*. (John Wiley & Sons, 2011). at <https://books.google.com/books?hl=en&lr=&id=_f994dmAdv0C&pgis=1>
4. Xin, H. First-principles Modeling of the Surface Reactivity of Transition Metals with Perturbed Electronic Properties. (University of Michigan, 2011).
5. Bard, a & Faulkner, L. Allen J. Bard and Larry R. Faulkner, Electrochemical Methods: Fundamentals and Applications, New York: Wiley, 2001. *Russ. J. Electrochem.* **38,** 1505–1506 (2002).
6. Adzic, R. R. *et al.* Platinum Monolayer Fuel Cell Electrocatalysts. *Top. Catal.* **46,** 249–262 (2007).
7. Sasaki, K. *et al.* Recent advances in platinum monolayer electrocatalysts for oxygen reduction reaction: Scale-up synthesis, structure and activity of Pt shells on Pd cores. *Electrochim. Acta* **55,** 2645–2652 (2010).
8. Lu, Y., Wang, Y. & Chen, W. Silver nanorods for oxygen reduction: Strong effects of protecting ligand on the electrocatalytic activity. *J. Power Sources* **196,** 3033–3038 (2011).
9. Markovic, N. M., Gasteiger, H. A. & Ross, P. N. Oxygen Reduction on Platinum Low-Index Single-Crystal Surfaces in Sulfuric Acid Solution: Rotating Ring-Pt(hkl) Disk Studies. *J. Phys. Chem.* **99,** 3411–3415 (1995).
10. Erikson, H., Sarapuu, A., Tammeveski, K., Solla-Gullón, J. & Feliu, J. M. Shape-Dependent Electrocatalysis: Oxygen Reduction on Carbon-Supported Gold Nanoparticles. *ChemElectroChem* **1,** 1338–1347 (2014).
11. Zinola, C. F., Castro Luna, A. M., Triaca, W. E. & Arvia, A. J. Kinetics and mechanism of the electrochemical reduction of molecular oxygen on platinum in KOH: influence of preferred crystallographic orientation. *J. Appl. Electrochem.* **24,** 531–541 (1994).
12. Holewinski, A., Idrobo, J.-C. & Linic, S. High-performance Ag-Co alloy catalysts for electrochemical oxygen reduction. *Nat. Chem.* **6,** 828–34 (2014).
13. Blizanac, B. B., Ross, P. N. & Marković, N. M. Oxygen reduction on silver low-index

single-crystal surfaces in alkaline solution: rotating ring disk(Ag(hkl)) studies. *J. Phys. Chem. B* **110,** 4735–41 (2006).

14. Koh, S., Toney, M. F. & Strasser, P. Activity–stability relationships of ordered and disordered alloy phases of Pt3Co electrocatalysts for the oxygen reduction reaction (ORR). *Electrochim. Acta* **52,** 2765–2774 (2007).

15. van der Vliet, D. F. *et al.* Mesostructured thin films as electrocatalysts with tunable composition and surface morphology. *Nat. Mater.* **11,** 1051–8 (2012).

16. Bondarenko, A. S., Stephens, I. E. L., Bech, L. & Chorkendorff, I. Probing adsorption phenomena on a single crystal Pt-alloy surface under oxygen reduction reaction conditions. *Electrochim. Acta* **82,** 517–523 (2012).

17. Tao, F. *et al.* Reaction-driven restructuring of Rh-Pd and Pt-Pd core-shell nanoparticles. *Science* **322,** 932–4 (2008).

18. Linic, S., Christopher, P., Xin, H. & Marimuthu, A. Catalytic and photocatalytic transformations on metal nanoparticles with targeted geometric and plasmonic properties. *Acc. Chem. Res.* **46,** 1890–9 (2013).

19. Marimuthu, A., Christopher, P. & Linic, S. Design of Plasmonic Platforms for Selective Molecular Sensing Based on Surface-Enhanced Raman Spectroscopy. *J. Phys. Chem. C* **116,** 9824–9829 (2012).

20. Marimuthu, A., Zhang, J. & Linic, S. Tuning selectivity in propylene epoxidation by plasmon mediated photo-switching of Cu oxidation state. *Science* **339,** 1590–3 (2013).

21. Christopher, P., Xin, H. & Linic, S. Visible-light-enhanced catalytic oxidation reactions on plasmonic silver nanostructures. *Nat. Chem.* **3,** 467–72 (2011).

22. Qian, X.-M. & Nie, S. M. Single-molecule and single-nanoparticle SERS: from fundamental mechanisms to biomedical applications. *Chem. Soc. Rev.* **37,** 912–20 (2008).

23. Kneipp, K., Kneipp, H. & Kneipp, J. Surface-enhanced Raman scattering in local optical fields of silver and gold nanoaggregates-from single-molecule Raman spectroscopy to ultrasensitive probing in live cells. *Acc. Chem. Res.* **39,** 443–50 (2006).

24. Van Cleve, T., Gibara, E. & Linic, S. Electrochemical Oxygen Reduction Reaction on Ag Nanoparticles of Different Shapes. *ChemCatChem* (2015). doi:10.1002/cctc.201500899

25. Schweitzer, N. M. Evaluating the Effect of a Strong Metal-Support Interaction on the Activity of Molybdenum Carbide Supported Platinum Water-Gas Shift Catalysts. (University of Michigan, 2010).

26. Ravel, B. & Newville, M. ATHENA, ARTEMIS, HEPHAESTUS: Data Analysis for X-ray Absorption Spectroscopy using IFEFFIT. *J. Synchrotron Radiat.* **12,** Journal of synchrotron Radiation (2005).

27. Newville, M. Fundamentals of XAFS. *Consortium for Advanced Radiation Sources* (2004).

Chapter 4

Atomistic engineering of superior ORR electro-catalysts by tailoring local chemical environment of Pt surface sites

4.1. Summary

The electrochemical oxygen reduction reaction (ORR) is the limiting half-reaction for low-temperature hydrogen fuel cells. While Pt is the most active single component electro-catalyst for the reaction, its high cost and relatively low ORR rates represent significant obstacles for the commercial application of the technology. So far, most research to overcome these limitations has focused on the alloys of Pt and 3*d* metals (Ni, Co, and Fe) which offer higher reactions rates and lower cost, albeit with lower stability. Herein, we synthesized, characterized and tested alloy materials belonging to a new family of electro-catalysts. The multilayer alloy materials contain AuCu alloy core of precise composition, surrounded by two Au layers and covered by a catalytically active Pt surface monolayer. Their performance relative to commercial Pt standards approaches a fourfold improvement in area-specific activity. The new family of alloy materials was identified using quantum chemical calculations. Characterization studies support the hypothesis that the activity improvement originates from a combination of a Au-Pt ligand effect, in which Au atoms perturb Pt surface sites, and local strain effect manipulated by tailoring the composition of the AuCu alloy core. Finally, the long-term stability of Pt alloy catalysts was assessed using established accelerated degradation protocols.

4.2. Introduction

Low temperature proton exchange membrane fuel cells are promising devices for portable power generation and transportation applications.[1] A critical obstacle to the commercialization of this technology is the significant voltage loss associated with the activation of the oxygen reduction reaction (ORR), $O_2 + 4(H^+ + e^-) \rightarrow 2\ H_2O$, even when costly Pt nanoparticle electro-catalysts are used.[2,3] These inefficiencies are manifested in high over-potentials required to achieve high current and power densities. In practical terms this means that significant amounts of Pt metal are required in fuel cells, making the overall cost prohibitively expensive.[2] Techno-economic analysis suggests that low temperature fuel cell technology would be commercially viable if the rates of ORR reactions on Pt-based nanoparticle electro-catalysts were higher by ~ 2-10 times on Pt mass basis compared to commercial Pt/C electrocatalysts which contain Pt nanoparticles with 3 – 5 nm diamter.[2,4–6] This objective can be accomplished by designing Pt alloy electro-catalysts that are inherently more active that pure Pt (on the surface area basis) and that contain smaller fractions of Pt atoms.

Studies have shown that an excellent descriptor of the ORR activity of metal electro-catalysts is the binding energy of the OH adsorbate.[7–12] It has been demonstrated that the optimal Pt-based metal catalysts (meeting the previously mentioned techno-economic target) should bind OH approximately 0.1 eV more weakly (less exothermic) compared to the Pt(111) surface, which is the best performing pure Pt surface facet.[8,10,11,13] It has been shown that one approach to accomplish this optimal OH binding is to synthesize Pt-3*d* metal alloys, where Pt is combined with 3*d* transition metals.[14–18] In particular, Pt/Co and Pt/Ni alloys have received considerable attention.[14,16,18–20] Various nano-architectures of these alloy materials, including alloy nanoparticles, de-alloyed mesoporous networks, and skeletal nano-structures, have been tested,

showing 2 – 3 times enhancements in the ORR rates on a per surface area basis compared to the commercial, pure Pt nanoparticle electro-catalysts at potentials of interest (between 0.7 and 0.9 V with respect to the reversible hydrogen electrode, RHE).[18,21–27] The models used to describe these alloys include a core containing Pt/3*d* alloy surrounded by a monolayer shell of pure Pt as shown in Figure 4.1.[15,23,28] While these Pt/3*d* alloys come close to meeting the techno-economic ORR activity targets, a possibly significant obstacle to their deployment is their potential lack of stability in highly acidic, high potential conditions of ORR. The main concerns are related to high thermodynamic driving forces for the leaching (dissolution as ions) of the 3*d* metal atoms through the thin Pt surface overlayer.[29]

The almost exclusive focus on the studies of the Pt/3*d* metal alloys has to a large degree been stimulated by the lack of other Pt alloy compositions that can meet the required criterion of elevated ORR rates compared to pure Pt. It would be beneficial to expand the family of Pt alloy materials which can meet or exceed the above-mentioned techno-economic targets beyond the Pt/3*d* alloys. Our group has previously performed high-throughput quantum computational screening to identify Pt alloys that meet the requirement of weaker OH binding energy by ~ 0.1 eV compared to the Pt (111) surface.[9,10,12,30,31] These studies showed that in addition to the Pt/3*d* alloys, the optimal OH binding environment relative to pure Pt could be accomplished by another family of Pt alloys. This family of alloys contains a catalytically active Pt surface monolayer, deposited on Au atom layers epitaxially grown on a metal alloy core (see Fig 1). The metal alloy core is used to control the lattice spacing of the top layer Pt atoms. We showed that an interplay of the ligand Au-Pt effect and the strain effect, controlled through the metal alloy core, yields materials that bind OH approximately 0.1 eV weaker than pure Pt(111) surface. [9,10,12] Another potentially appealing feature of these layered, Au-containing alloys is that the Au interlayers

between the Pt surface layer and the core could act as a chemically stable buffer that protects the elements in the internal core structure from leaching.

Herein, we synthesized, characterized and tested an alloy material belonging to this family of electro-catalysts in the form of alloy nanoparticles. The nanoparticles contain AuCu alloy core of precise composition, surrounded by two Au layers and covered by a Pt surface monolayer. We rigorously tested the ORR polarization behavior of these alloy nanoparticle electro-catalysts using rotating disk thin electrode (RDE) voltammetry, showing that these materials exhibit up to 3.5 times higher ORR rates on per surface area basis compared to the commercial Pt nanoparticles (~5nm diameter). We believe that this family of alloy materials offers a new direction to the field which has almost exclusively been focused on the Pt/3*d* alloys.

4.3. Experimental and Theoretical Methods

4.3.1. Syntheses of Au_xCu_{1-x}/C

AuCu nanoparticles were prepared by thermally reducing gold (III) chloride trihydrate ($AuCl_3 \cdot 3H_2O$, Sigma Aldrich) and copper acetylacetonate ($Cu(acac)_2$, Fisher) precursors in 20 mL of oleylamine under reflux conditions. Typically, 150 mg of $AuCl_3 \cdot 3H_2O$ was added to 100 mL round bottom flask containing 20 mL of oleylamine heated to 40°C. The reflux condenser was sealed and fed a positive pressure of Ar. The flask was heated to 110°C with magnetic stirring and left for 4 hours to completely reduce $AuCl_3$ to Au nanoparticles. The flask was then removed from the silicone oil bath and allowed to cool for at least 10-15 minutes. Then, 20-30 mg of $Cu(acac)_2$ was added to Au nanoparticle solution. The flask was lowered back into the oil bath and gradually heated to 280°C under excess flow of Ar through the condenser. After 1 hour at 280°C, the flask was removed from the heated oil bath and allowed to cool. The nanoparticle suspension was rinsed

with methanol (Fisher) and nanoparticles were collected by centrifugation (8 minutes at 8000 rpm). Following three methanol washes, the nanoparticles were resuspended in n-hexane (Sigma).

The alloy nanoparticles were deposited onto pre-treated carbon (Vulcan XC72R-Cabot) at roughly 20 wt% loading in hexane and allowed to mix under continuous stirring for at least 24 hours. After mixing, supported nanoparticles would settle and samples were collected by rinsing the sample with isopropanol and concentrating the sample by centrifugations (another 3 washes at 8000 rpm for 8 minutes). The supported nanoparticles (AuCu/C) were collected in pure ethanol and allowed to dry in oven overnight. The supported cores were characterized by XRD, ICP-AAS, and TEM/STEM to verify synthesis of intermetallic alloy nanoparticles. Powders were thermally treated for 5 hours in air at 185°C prior to electrochemical preparation.

4.3.2. Synthesis of $Au_xCu_{1-x}@Au_2@Pt$

Atomic layers of Au and Pt were epitaxially grown on supported AuCu cores via galvanic replacement of a sacrificial Cu adlayer to achieve the desired nanostructure represented in Fig. 1b. Cu monolayers were deposited onto Au using the copper underpotential deposition (Cu UPD) phenomenon.[32–35] In short, the electrode was held at a set potential slightly above the bulk Cu^{2+}/Cu redox potential (-0.35 V against $Hg/HgSO_4$ (sat. K_2SO_4) reference electrode) in 0.05M H_2SO_4 solution containing 5mM $CuSO_4$. At this potential, only a monolayer (atomic layer) was deposited onto Au surface because the deposition of multiple Cu layers was unfavorable. Multiple sweeps to higher potentials were performed to verify that similar amounts of Cu were deposited on consecutive scans. After removing the electrode under potential control, the electrode was rinsed with ultrapure water (18.2 MΩ·cm (Millipore)) and deposited into a solution containing either 1μM $AuCl_3$ or K_2PtCl_4. 2/3 ML of Au or 1 ML Pt will deposit for every 1 ML of Cu removed so 3 deposition cycles are required for Au and another for Pt monolayer to prepare the

AuCu@Au_2@Pt structure. After depositing Au/Pt over a few minutes, the electrode was rinsed to remove excess metal precursors before continuing depositions or beginning electrochemical testing. Samples were characterized with electron microscopy before and after ORR activity and electrochemical surface area measurements.

4.3.3. Synthesis of Pt_{House}/C

Pt nanoparticles were prepared by thermally reducing potassium tetrachloroplatinate (K_2PtCl_4, Sigma-Aldrich) in ethylene glycol (JT Baker) in the presence of polyvinylpyrrolidone (PVP M_W =10k, Sigma-Aldrich). 15 mL of ethylene glycol was heated for 1 hr at 150°C in silicone oil bath. Pt and PVP solutions were prepared by dissolving 130 mg of K_2PtCl_4 and 150 mg of PVP in separate vials containing 2 mL and 8 mL of ethylene glycol. The Pt solution was added instantaneous to the hot ethylene glycol then the PVP solution was added dropwise over the course of several minutes. The solution was allowed to react for 1 hr before being removal from the oil bath. Nanoparticles were collected by centrifugation in acetone (8000 rpm for 20 minutes) and ethanol (9000 rpm for 30 minutes). Pt nanoparticles were redispersed in pure ethanol and deposited on carbon support. Commercial 3nm and 5nm Pt/C standards were purchased by Alfa Aesar and Sigma-Aldrich, respectively.

4.3.4. Electrochemical testing (RDE and CV measurements)

Electrochemical measurements were performed at room temperature in a custom-made, all-Telfon three-electrode cell with a Gamry Instruments Reference 3000 potentiostat/galvanostat/frequency response analyzer. The working electrodes were prepared by sonicating the catalysts powders in absolute ethanol (Fisher) at 0.75 mg mL^{-1} for > 1 hr. A uniform film of catalysts was achieved by depositing four 10 μL droplets onto a 5 mm glassy carbon electrode insert (Pine Instruments) at a rotation around 600 rpm using the inverted RDE. All

electrochemical measurements were performed in 0.1 M $HClO_4$. The reference electrode was Ag/AgCl in 3 M KCl with saturated AgCl (Radiometer Analytical) and counter electrodes (Pt wire, Alfa Aesar) were both in isolated compartments connected by capillaries to the working electrode chamber.

Electrolyte solutions of 0.1 M $HClO_4$ were prepared from ultrapure water and 70% perchloric acid (Merck Suprapur). A consistent uncompensated resistance of ~25 Ω was measured with high-frequency impedance, and was corrected for in the polarization curves. All potentials are reported relative to the reversible hydrogen electrode which is calibrated against the H_2 oxidation equilibrium at the pH of the solution. Reported currents have been corrected for capacitance and uncompensated solution resistance. Sample capacitance was measured by comparing the differences in the limiting current (around 0.3-0.5 V_{RHE}) between forward and reverse scans during the electrode conditioning scans in O_2 saturated electrolyte at 100 mV s^{-1} between 0.05 and 1.0 V_{RHE}.

Cyclic voltammetry was performed in Ar-purged electrolyte at 50 mV s^{-1}. ORR polarization curves were measured in O_2- saturated electrolyte at rotation rates of 400, 900, 1600, and 2500 rpm. CO-stripping voltammetry was performed immediately following post-polarization CV scans by holding the working electrode at 0.05 V_{RHE} as CO was bubbled (5 minutes) followed by an Ar gas purge (20 minutes) to remove excess CO from solution. The electrode potential was then scanned to 1.0 V_{RHE} at 10 mV s^{-1}. Determination of ECSA is discussed in greater detail in section 4.6.

4.3.5. Characterization Techniques

UV-visible extinction spectroscopy (UV-vis) experiments were performed using a Thermo Scientific Evolution 300 UV-Vis spectrophotometer with a Xenon lamp source to measure the

extinction spectra of dilute AuCu nanoparticle suspensions in hexane. UV-vis spectra were collected between 300 and 1000 nm at a rate of 240 nm min^{-1} and were normalized by the extinction peak signal intensity to facilitate comparison of samples with different concentrations. XRD measurements were conducted in a Rigaku rotating anode diffractometer with a monochromated Cu Kα X-ray source at a scan rate of 5° min^{-1}. Ion coupled plasma optical emission spectroscopy was performed on samples dissolved in aqua regia (3:1 mixture of concentrated HCl and HNO_3) using a Perkin-Elmer Optima 2000DV with Winlab software to determine the molar composition of bulk AuCu nanoparticles. Au and Cu signals were normalized by 2 ppm Yttrium internal standard and concentrations were measured three times using calibrated standards of 0, 1, 2, 5, 10, 20, and 40 ppm Au and Cu solutions.

Aberration-corrected STEM imaging and sub-nm resolution STEM-EDS were performed at the Center for Nanophase Materials Sciences at Oak Ridge National Laboratory with a JEOL 2200FS TEM/STEM equipped with a CEOS aberration (probe) corrector and operated at a 200 kV accelerating voltage. The microscope was operated in high angle annular dark field (HAADF)-STEM imaging mode and was equipped with a Bruker AXS X-Flash 5030 silicon drift detector. The probe size was ~0.7 Å and the probe current was ~30 pA during HAADF-STEM imaging. When collecting the EDS spectrum image data, the probe current was increased to ~280 pA and the probe size was ~2 Å.

4.3.6. Theoretical methods

All DFT calculations were carried out with the GPAW plane wave code (https://wiki.fysik.dtu.dk/gpaw/) using the generalized gradient approximation and revised Perdew, Burke and Ernzerhof exchange correlation functional. All surface calculations used a five-layer 2 × 2 fcc [111] periodic unit cell separated by 12 Å of vacuum space in the [111] direction

and a dipole layer to decouple the slabs electrostatically. The bottom two layers were fixed and the top three layers and all adsorbates were relaxed until the sum of forces was below 0.05 eV $Å^{-1}$. Ultrasoft pseudopotentials were used to represent the ionic cores, with the valence electron density determined through iterative diagonalization of the Kohn–Sham Hamiltonian using Pulay mixing. Unit cells were sampled with a 6 × 6 × 1 Monkhorst–Pack *k*-point grid, and the plane-wave basis-set energy cutoff was 340 eV. An electronic temperature of 0.1 k_BT was used, with final energies extrapolated to 0 K. Lattice constants for Au, Cu, Pt, and AuCu alloys were calculated using a 4 atom unit cell with a 8 x 8 x 8 k-point grid.

4.4. DFT calculations of OH adsorption energies on model and alloy systems

The electrochemical reduction of O_2 involves 4 electron/proton transfer steps to reduce oxygen to water. It has been demonstrated that in this process O_2 undergoes the initial electron/proton transfer to form an adsorbed OOH intermediate.[36] This high energy intermediate dissociates to generate O and OH intermediates, which are further reduced on the electro-catalyst surface by the subsequent proton/electron transfer steps and removal from the surface as H_2O. On Pt electrodes at high operating ORR potentials, OH is the most abundant surface intermediate, effectively blocking catalytic surface sites and preventing O_2 activation, thereby lowering the overall rate of oxygen reduction. For this reason, a more active metal catalyst would bind OH less strongly relative to Pt without making the other steps kinetically slower. As described above, detailed kinetic analysis has shown that this objective can be accomplished if the Pt surface is changed in a way that it binds OH by approximately 0.1 eV less strongly than Pt(111).[8–10,12]

We used Density Functional Theory (DFT) calculations to compute the binding energy of OH on the alloy materials relative to the Pt(111) surface. The Pt(111) surface was modeled as five layers of Pt with the equilibrium Pt-Pt lattice spacing. The alloys were modelled as slabs

containing a surface monolayer of Pt, covering two Au layers on top of two additional Pt layers ($Pt_2@Au_2@Pt$). The top three layers were fully relaxed in the *z*-direction in all systems. Data in Figure 4.1a show the differences in the OH adsorption energy on the $Pt_2@Au_2@Pt$ model alloy systems relative to Pt (111) ($\Delta\Delta E_{OH}=E_{alloy+OH}-E_{alloy}-(E_{Pt+OH}-E_{Pt})$) as a function of the *xy* lattice spacing of the alloy. The DFT calculations showed that the OH adsorption energy on these alloys at the equilibrium lattice of Pt is 0.2-0.3 eV weaker (less exothermic) than on pure Pt. The change in the OH binding energy in these systems relative to pure Pt is mainly due to the Au-Pt ligand effect, where electronic interactions between the Pt surface atoms and Au atoms under the Pt surface layer impact the electronic structure of Pt and therefore the OH adsorption energy. The destabilization of OH in these systems is greater than desired (> 0.1 eV); however, this can be modulated by slightly expanding the lattice of the alloy compared to the pure Pt lattice. The data in Figure 4.1e show that the lattice should be expanded by approximately 2 % relative to pure Pt to reach the optimal OH binding environment. We find that while the OH binding energies are slightly affected by the number of subsurface Au layers used in our model systems, the overall conclusions are unchanged.

The question is how to design electro-catalyst materials that can best mimic the model alloys used in the DFT calculations. In particular, control over the lattice spacing (i.e., the strain effect) in the alloy is a significant obstacle to their synthesis. One approach to control the lattice spacing is to use alloys of highly miscible metals, which can span a large range of lattice spacing as the core of nanoparticles onto which Au and Pt atoms are deposited. A promising alloy to accomplish this objective is AuCu. These two metals form an almost ideal alloy mixture where the lattice spacing scales linearly with the relative Au and Cu concentrations in the alloy. The data in Figure 4.1f show the relative lattice expansion for AuCu alloys compared to pure Pt for the

experimentally-measured and DFT-calculated lattice parameters as a function of Au mole fraction in the AuCu alloy.[37] The data suggest that 2-3 % expansion of the lattice constant compared to pure Pt is accomplished for AuCu alloys with the Au content between 70 and 90 %.

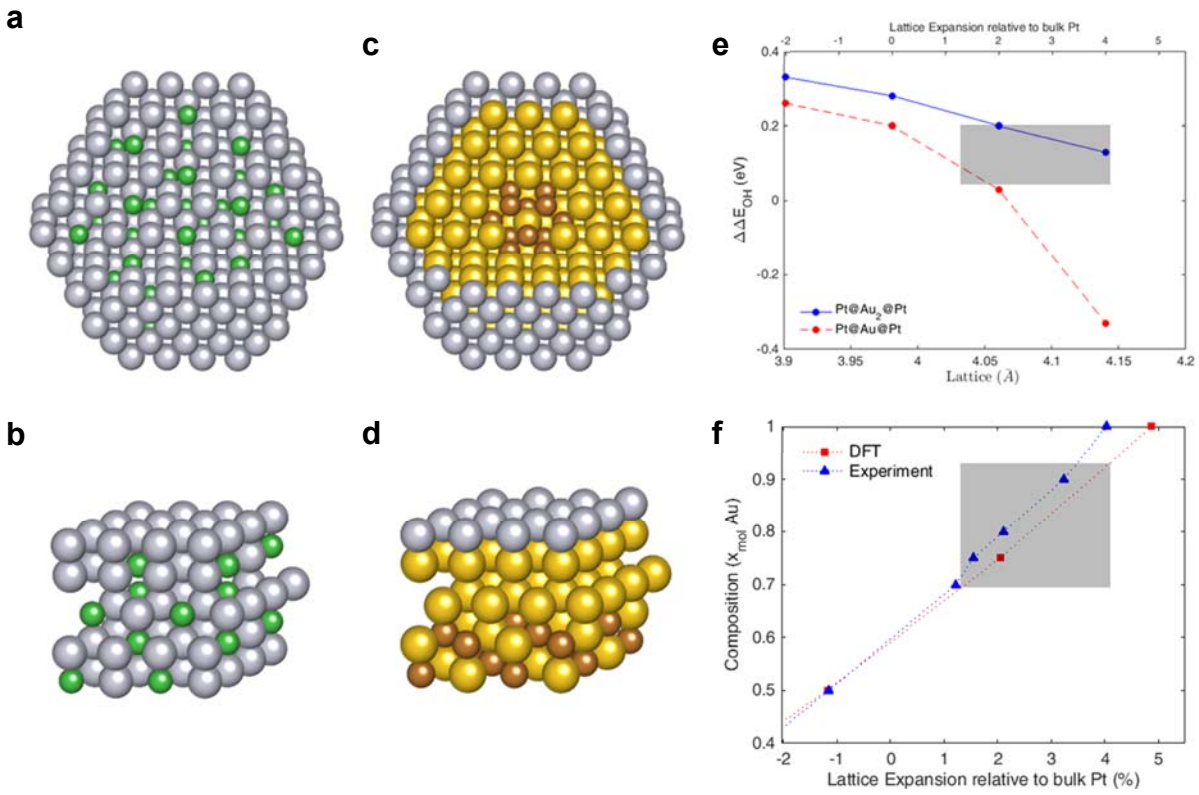

Figure 4.1. Representations of Pt_3Ni and AuCu@Au_2@Pt electrocatalysts as nanoparticles (a,c) and (111) surface slab (b, d). e) DFT-calculated OH binding energies as a function of the x-y lattice constant on various 111 surfaces: Pt_3@Au@Pt and Pt_2@Au_2@Pt. f) Molar composition of Au in Au/Cu alloys as a function of experimental[37] and DFT-calculated lattice parameters. The shaded regions highlight alloy surfaces that bind OH by 0.05 - 0.2 eV weaker than Pt, which should exhibit superior performance compared to Pt.

Guided by these findings we synthesized AuCu alloy nanoparticles, containing 75 and 85% molar fraction of Au with the balance Cu, using a thermal reduction approach.[38] These nanoparticles were supported on a carbon support and electrochemically treated to deposit two layers of Au atoms and finally one layer of Pt atoms on the AuCu cores, yielding nanoparticle

electro-catalysts that mimic the model system shown in Figure 4.1. The synthesis procedure is described in greater detail in the sections 4.3.1-2.

4.5. Catalyst Characterization

Prior to the electrochemical deposition of Au and Pt over-layers, the AuCu core nanoparticles were characterized. The data in Figure 4.2 show the UV-Vis extinction spectra for various compositions of AuCu alloy nanoparticles. The high wavelength extinction feature is the consequence of the excitation of localized surface plasmon resonance (LSPR). The data show that pure Au nanoparticles exhibit an LSPR extinction feature at ~510 nm, which is characteristic for Au nanoparticles of ~ 10 nm diameter.[39] As the content of Cu in the nanoparticles increases the LSPR peak is red-shifted to higher wavelengths. This LSPR red shift is an unambiguous characteristic of the formation of AuCu alloy nanoparticles.[40] The red shift is accompanied by the increase in the low wavelength extinction. This is the consequence of inter-band ($d \rightarrow sp$) electronic transitions in Cu atoms which are of lower energy (higher wavelength) than the corresponding transitions in Au.[40]

AuCu nanoparticles supported on carbon (AuCu/C) were also characterized using X-ray diffraction (XRD). The data in Figure 4.3 show the diffraction patterns for $Au_{75}Cu_{25}$, as well as pure Au and Pt nanoparticles. The XRD data show no evidence of distinct Au or Cu phases in alloys. The diffraction peaks of $Au_{75}Cu_{25}$ are located between equivalent peaks of Au and Pt samples, suggesting that the alloy has an intermediate lattice parameter. The analysis of (111), (200), and (220) peak locations using Bragg's law indicated that the lattice constants of $Au_{75}Cu_{25}$ and Pt samples were ~ 4.03 Å and 3.91 Å, respectively, making the $Au_{75}Cu_{25}$ lattice about 3 % larger than Pt.

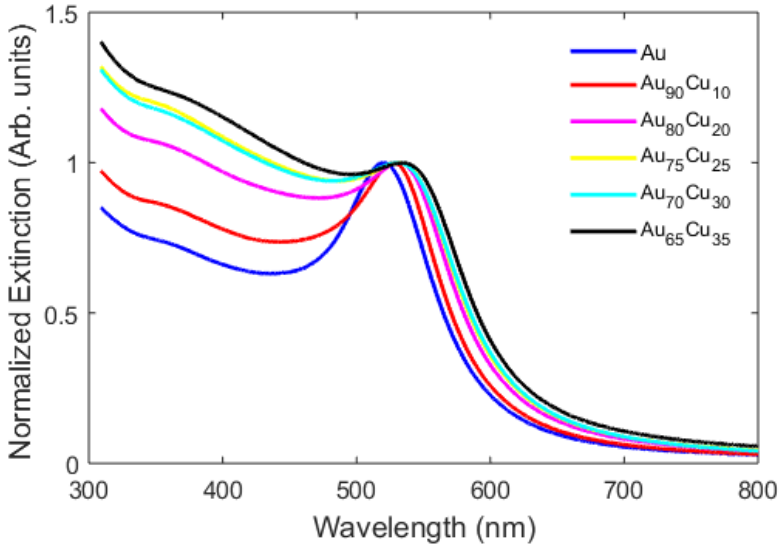

Figure 4.2. Normalized UV-Vis extinction spectra for various AuCu nanoparticle suspensions in hexane.

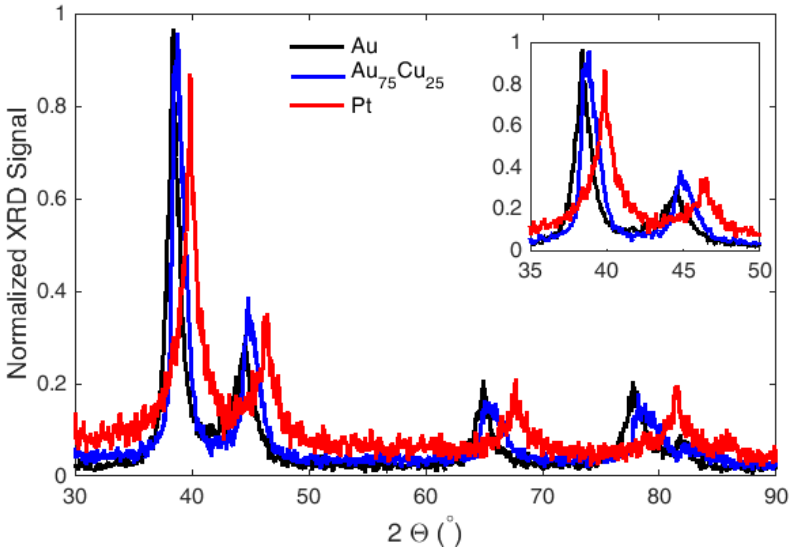

Figure 4.3. X-ray diffraction patterns for Au, $Au_{75}Cu_{25}$, and Pt nanoparticles supported on Vulcan XC72R carbon support.

Alloy nanoparticle samples were characterized by transmission electron microscopy (TEM) to assess changes in particle morphology following the electrochemical deposition of Au and Pt atomic layers. Prior to the deposition, AuCu nanoparticles on Vulcan XC72R support (Figure 4.4a) were found to be roughly spherical with an average diameter of 10.9 nm (standard

deviation of 1.7 nm). After the electrochemical deposition, AuCu@Au_2@Pt nanoparticles maintained their spherical shape (Figure 4.4b), but found to be slightly larger with average diameter of (14.1nm ± 3.28 nm). The molar composition of the AuCu electro-catalysts cores was measured using ion coupled plasma optical emission spectroscopy, and it was found to match the nominal metal loadings.

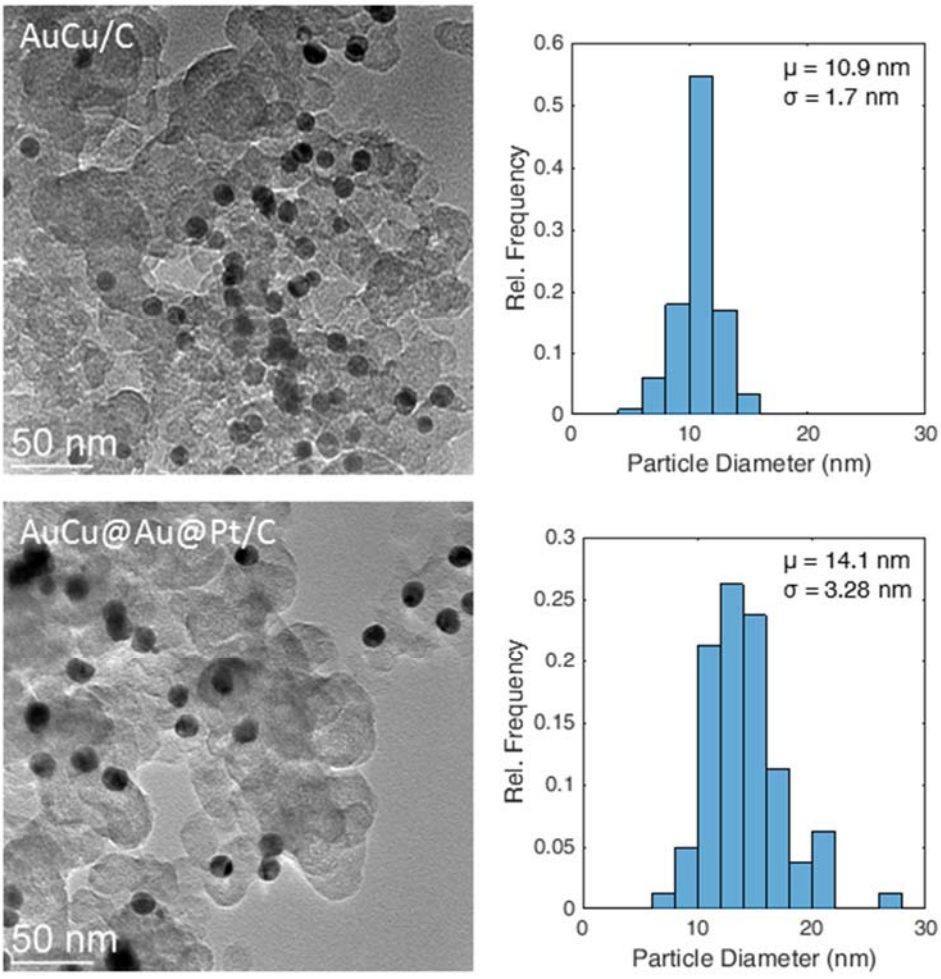

Figure 4.4. Representative TEM micrographs of AuCu/C (a) and AuCu@Au@Pt/C (b) catalysts with corresponding particle-size histograms (c and d).

After supporting the AuCu nanoparticles on carbon, two layers of Au and Pt were deposited electrochemically on these nanoparticles by the galvanic replacement of under-potentially deposited Cu layers (Cu UPD) (see Methods). The polarization behavior of these Pt alloys was tested under ORR conditions as described below. The bright field (BF) scanning transmission electron microscopy (STEM) micrograph in Figure 4.5a shows a collection of ($Au_{75}Cu_{25}$@Au_2@Pt)/C nanoparticles after the performance tests. Images in Figures 3b and 3c display elemental maps of Au, Pt, and Cu in the nanoparticle electro-catalysts acquired using energy dispersed x-ray spectroscopy (EDS) in the STEM after the ORR performance test. The elemental mapping shows the nanoparticles maintain their structural integrity after electrochemical testing; Pt atoms are detected at the surface of the nanoparticles with Au and Cu occupying the core of the nanoparticles.

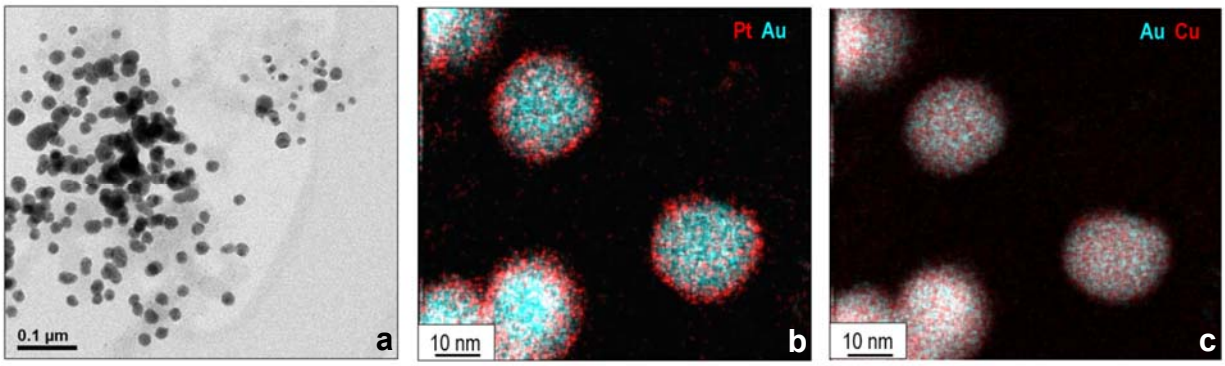

Figure 4.5. a) BF-STEM micrograph depicting a collection of $Au_{75}Cu_{25}$@Au_2@Pt nanoparticles on carbon support. b) and c) EDS elemental maps show the distribution of Pt, Au, and Cu throughout sample.

4.6. Determination of electrochemical surface area on Pt alloys

Accurate determination of the electro-catalytic activity per site (i.e., the turnover frequency) requires rigorous measurement of the real surface area of the electrode. Most commonly, the electrochemical surface area (ECSA) of Pt and Pt-based nanostructures is

determined from the integration of stripping charge of the hydrogen underpotential deposition (H_{UPD}) peak in cyclic voltammetry (0-0.45 V vs. RHE).4 This charge is then readily converted to surface area using the conversion factor 210 μC/cm^2 (assuming complete, monolayer H coverage).[41] However, due to the linear scaling relations that exist, the ECSA measurements based on H_{UPD} can underestimate true surface area (suppress H_{UPD} features) for surfaces with modified electronic structures that bind the different adsorbates less strongly, such as the $Au_xCu_y@Au_2@Pt$ surfaces in this study. This suppression leads to an overrating of H_{UPD}-based specific activity, which is unfortunately rather prevalent in the literature.[42,43]

Therefore, we resorted to an alternative method, the removal (stripping) of an adlayer of CO. In this process, CO was first adsorbed onto the surface of the electrode immersed in the same solution of 0.1 M $HClO_4$ following ORR activity testing. CO was bubbled into the cell at 30 sccm for ~5 min while keeping the electrode at a constant potential of 0.05 V_{RHE}. To remove excess (un-adsorbed) CO from the electrolyte, the solution was purged with Ar for ~20 min while the electrode was still held at 0.05 V. At this point, the potential was swept from 0.05 V to 1.0 V at a rate of 10 mV/s. Distinct CO oxidation peak appeared at ~0.8 V. The potential was then scanned back to 0.05, then cycled again between these two bounds for 4 additional times, followed by a final anodic sweep to 1.0 V. The usual CV features on Pt (e.g., H_{UPD} and oxide formation) were completely suppressed until all adsorbed CO was removed in the first anodic sweep. Subsequent voltammograms taken in the absence of CO, beginning with the first cathodic sweep, exhibited the usual characteristics. Data in Figure 4.6a shows representative CO stripping results collected from Pt alloy test.

Integration of the CO stripping peak allowed the determination of the ECSA assuming 420 μC/cm^2.[41] In order to eliminate the contribution of the double layer charging and oxide formation,

the second anodic sweep (with no CO oxidation features) was subtracted from the first anodic sweep (with the distinct CO oxidation peak). Furthermore, capacitance and uncompensated solution resistance corrections were performed. After accounting for these corrections the area under the CO oxidation curve is integrated with the appropriate linear baseline correction (typically between 0.65 and 0.9 V_{RHE}).

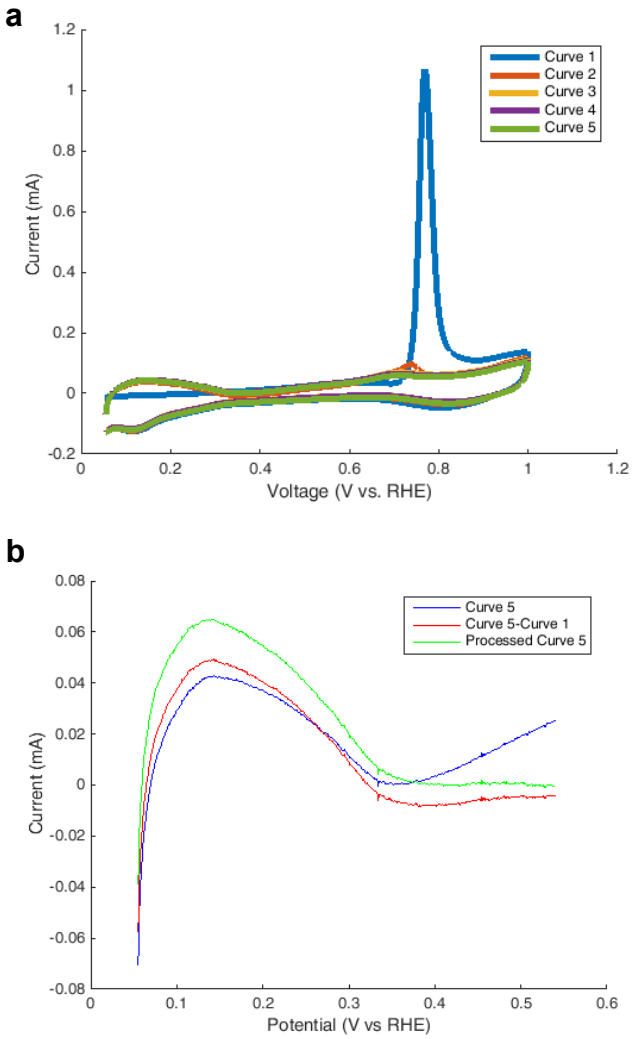

Figure 4.6. a) Cyclic voltagrams of CO adsorpted Pt alloy sample measured in Ar-purged 0.1M $HClO_4$ electrolyte between 0.05 and 1.0 V_{RHE} at scan rate of 10mV/s. b) The blue line shows the uncorrected raw data from Curve 5 in part a, the red line corresponds to capacitance correction by subtracting measured currents during first scan in this experiment, and the green curve corresponds to the red curve with a linear baseline to make the clean Pt region flat at 0 prior to integration.

Similar analysis was performed to determine H_{UPD} areas using the first scan (CO-poisoned surface) as reference for capacitance corrections on H_{UPD} scans. This capacitive correction makes it easier to determine the flat double layer region which could then be used to find an appropriate baseline for integration when determining H_{UPD} surface area. The curves presented in Figure 4.6b correspond to raw currents (blue), capacitance corrected currents (red), and capacitance with background-corrected currents. Performing a simple integration with horizontal line at end of HUPD region (0-0.45 V_{RHE}), it is clear that $ECSA_{green} \geq ECSA_{red} > ECSA_{blue}$. We chose to normalize activities using the most rigorous correction methods because these ECSAs were more consistent with ESCA calculated by CO stripping and Cu UPD measured on Pt nanoparticles.

4.7. Electrochemical Performance

Data in Figure 4.7 show the electrochemical ORR polarization behavior of nanoparticle electro-catalysts without Pt and Au layers (*i.e.*, only the AuCu core), with the Au layers but without Pt (AuCu@Au_2/C), and with both Pt and Au layers deposited onto the AuCu cores (AuCu@Au_2@Pt/C) normalized by electrode geometric surface area (A = 0.196 cm^2). Measurements were performed in the thin-film rotating disk electrode (RDE) configuration at rotation rates of 400, 900, 1600, and 2500 rpm. The data show that both bare AuCu and Au-coated AuCu electrocatalysts exhibited poor ORR activity and selectivity, manifested in high overpotential losses and low limiting current densities. The data in Figure 4.7 also show that upon the deposition of a Pt layer, the ORR reaction rate (i.e., the current) is dramatially increased. Analysis of limiting current densities as a function of RDE rotation rates using the Levich approach showed that the Pt alloys exhibited 4 e^- oxygen reduction with almost exclusive H_2O selectivity.

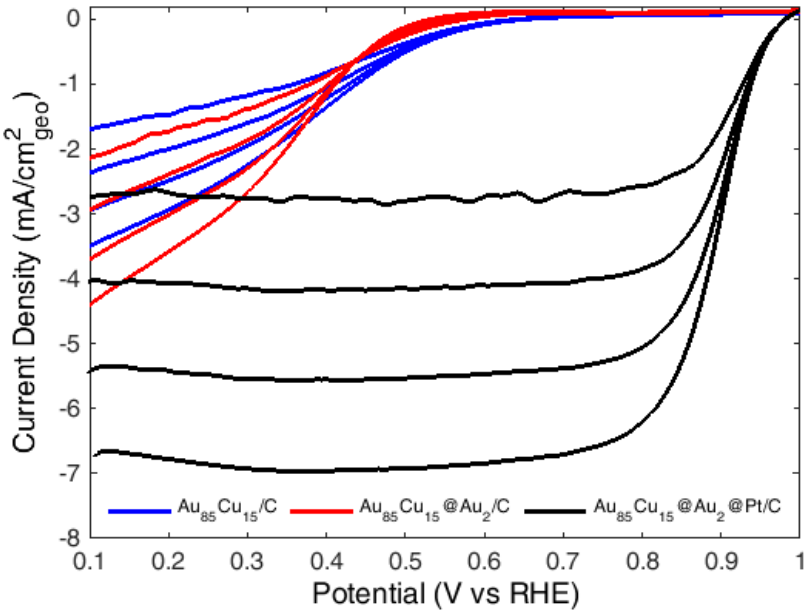

Figure 4.7. Raw current, i.e., oxygen reduction rates (normalized by the geometric electrode surface area) of $Au_{85}Cu_{15}$/C, $Au_{85}Cu_{15}$@Au_2/C, and $Au_{85}Cu_{15}$@Au_2@Pt/C as a function of potential (V vs. RHE) at rotation rates of 400, 900, 1600, and 2500 rpm.

Kinetic current densities were calculated using the Koutecky-Levich equation. First, kinetic current was computed using $|i_k(V)| = (1/|i(V)| - 1/|i_L|)^{-1}$, where i is the measured current, i_k is the kinetic current, and i_L is the limiting current measured between 0.3 and 0.6 V_{RHE}. To quantitatively assess the kinetic activities of the alloys and compare these to the systems containing commercial Pt electro-catalysts, it is critical to rigorously measure the surface area of the nanoparticle electro-catalysts. The electrochemical surface area (ECSA) of the electro-catalysts was determined using two approaches, CO stripping and H under potential deposition (H_{UPD}) voltammetry. The kinetic current was then normalized by the ECSA to obtain kinetic current density. Data in Figure 4.8 show the kinetic current density as the function of potential for pure Pt and the alloy materials. The data show that across the entire potential range of interest the alloys outperform the commercial Pt standard. The data also show that pure Pt and the Pt alloy

electrocatalysts exhibit similar Tafel behavior, suggesting that ORR proceeds through a similar mechanism on these electro-catalysts.[36]

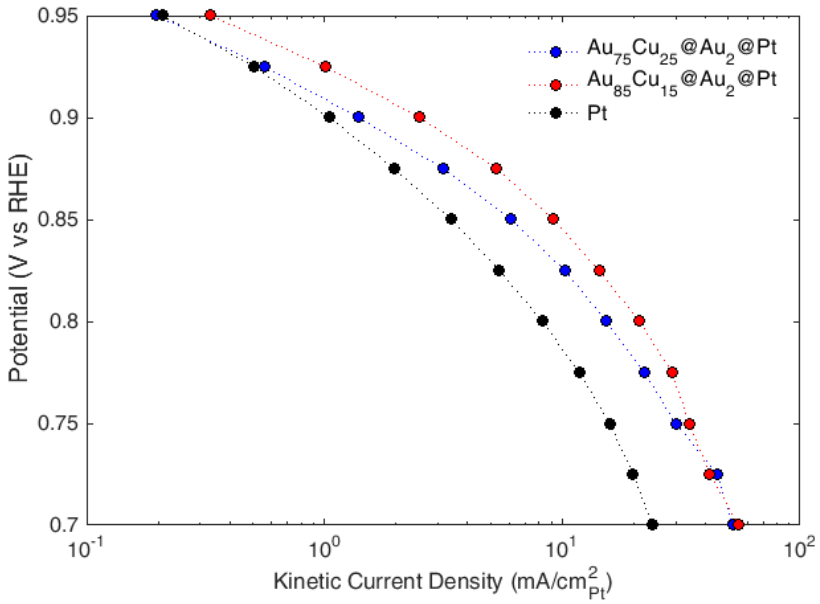

Figure 4.8. Tafel plots of specific kinetic current densities of the alloys and Pt electrocatalysts.

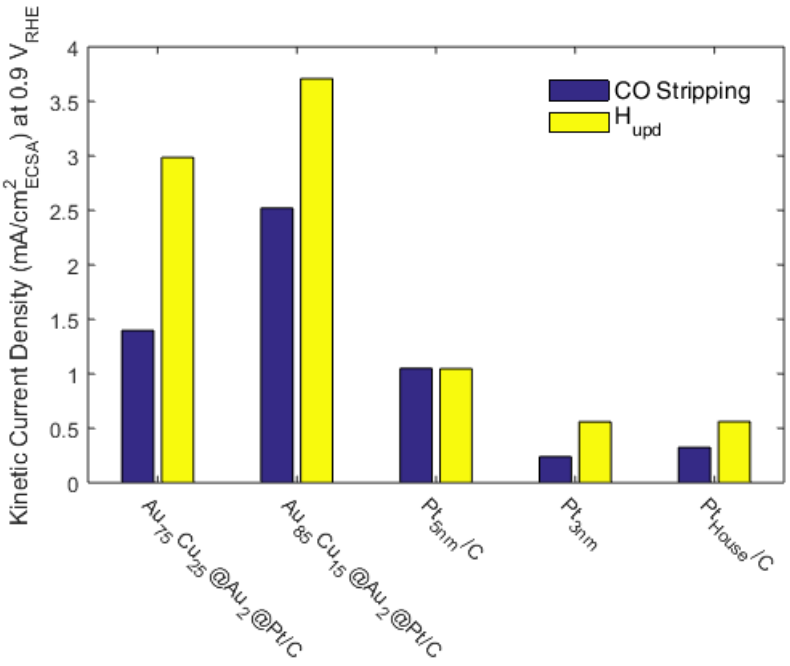

Figure 4.9. Specific kinetic current density of Pt and Pt alloy electrocatalysts at 0.9V_{RHE} in 0.1 M $HClO_4$ normalized by H_{UPD} and CO surface areas.

Data in Figure 4.9 show the kinetic current densities of $Au_{75}Cu_{25}$@Au_2@Pt/C, $Au_{85}Cu_{15}$@Au_2@Pt/C, and Pt/C measured at 0.9 $V_{RHE.}$ The data show that the current for the commercial Pt/C (5 nm) is roughly 1.0 mA/cm^2, which is consistent with other reports in the literature showing that if rigorously measured, the 5 nm Pt nanoparticle electro-catalysts exhibit ORR activities between 0.8-1.2 mA/cm^2 at these conditions.[44] The data also show that both alloy samples exhibit superior ORR performance compared to the commercial Pt standard. For example, the ORR rates on $Au_{85}Cu_{15}$@Au_2@Pt/C nanoparticle electro-catalysts are ~ 2.5 and 3.7 times greater than on pure Pt based on the CO-stripping and H_{UPD} ECSAs, respectively. We note that the surface areas of Pt-based ORR electro-catalysts are often underestimated in the literature, resulting in overestimated activities, since these are usually measured using the H_{UPD} oxidation technique, which, due to different binding energies of H atoms on the Pt alloys compared to pure Pt samples and the proximity of H_{UPD} potentials to the H_2 evolution and OH adsorption potentials, can induce significant errors in the surface area measurements.[42,43] Figure 4.9 also shows the measured kinetic current densities for a pure Pt nanoparticle electro-catalyst prepared in house using identical precursors and carbon support used in the synthesis of alloy samples. These catalysts exhibit the ORR rates similar to commercial 3nm Pt standards, which are consistent with their size.[2,44,45] It is also important to comment on the impact of the size of nanoparticles on the activity. It is well established that polycrystalline Pt film electrodes exhibit the highest reported intrinsic ORR activity for Pt electrodes, measured to be between 1.7-2.0 mA/cm^2 at 0.9 V_{RHE} based on the H_{UPD} surface areas.[46,47] Even this high limit of the Pt performance is well below the activities reported on our alloy nanoparticle electro-catalysts.

We hypothesized that the main reason for the improved performance of the Au-Cu-Pt electro-catalysts compared to pure Pt was weaker OH binding on alloys. The data in Figure 4.10 shows cyclic voltammograms (normalized by H_{UPD} ECSA) for Pt and the alloy electro-catalysts measured in Ar-purged 0.1M $HClO_4$. All samples exhibit the main features characteristic of Pt electrodes: H adsorption at low potentials (0.0 – 0.4 V_{RHE}), increasing OH coverage around 0.7 V_{RHE}, and further surface oxidation at higher potentials. Compared to Pt, both alloys exhibit weaker surface OH features and the onset of surface oxidation at higher potential, which is consistent with a weaker binding of oxygenated surface intermediates. The data in Figure 4.11 shows the CO stripping curves for the electro-catalyst measured in 0.1M $HClO_4$ on the RHE potential scale. On both Pt alloys the CO oxidation takes place at slightly lower potentials relative to pure Pt, which is also consistent with weaker binding of CO and other intermediates (potentially including OH) involved in the CO stripping process on the alloys.[42,43]

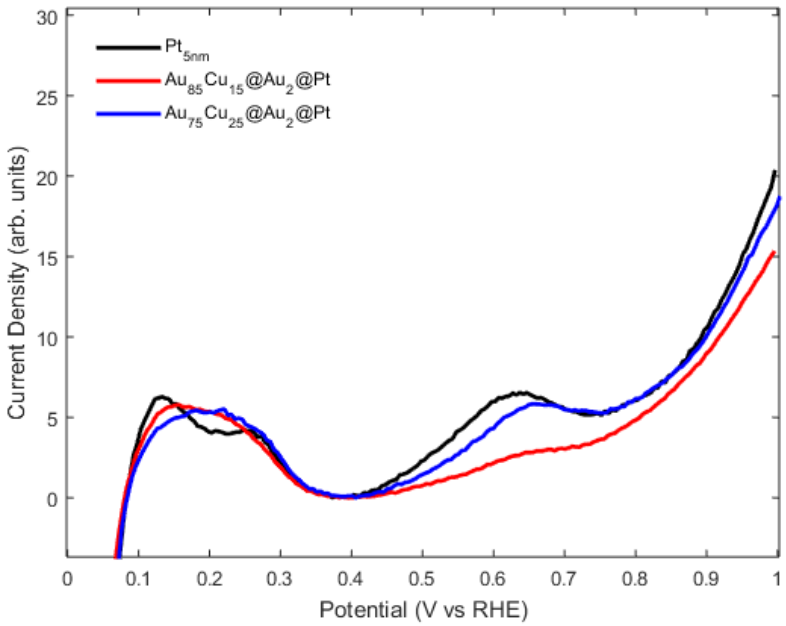

Figure 4.10. CVs of Pt and the alloy electro-catalysts measured in Ar-purged 0.1 M HClO4 electrolyte normalized on an equal H_{UPD} area basis

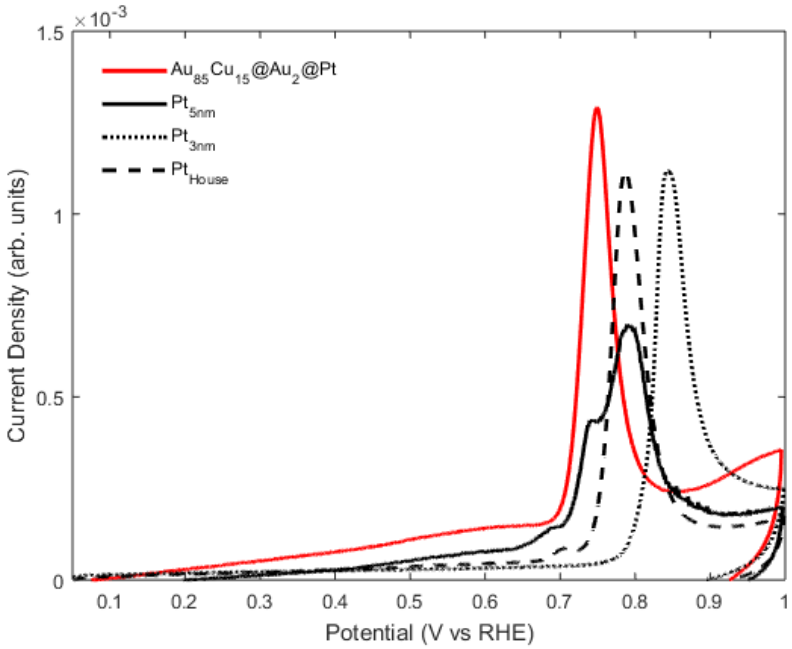

Figure 4.11. CO stripping voltammograms for Pt and Pt alloy electro-catalysts measured in 0.1 M $HClO_4$.

4.8. Long-term Stability testing

The longterm stability of Pt alloy and commercial Pt catalysts were assessed using a DOE protocol for accelerated durability test (ADT).[48] In these systems, the electrocatalysts were attached to the carbon support using Nafion to minimize particle detachment issues. The addition of Nafion was shown to reduce the specific ORR activity on both Pt and Pt alloy samples by roughly half compared earlier results reported in Figures 4.8-9. The electrodes were aged by repeated voltage cycling between 0.6 and 1.0 V_{RHE} at 50mV s^{-1} in O_2-saturated electrolyte. The ORR activity and ECSA were measured at cycles 1, 1,000, 5,000, 10,000, 20,000, and 30,000. Accumulation of surface contaminants and evaporation of solution can degrade ORR activity, so the electrochemical cell was rinsed and refreshed with clean electrolyte immediately before each activity measurements at 5,000, 10,000, 20,000, and 30,000 cycles. Data in Figure 4.12a show that kinetic current densities of Pt/C and $Au_{85}Cu_{15}@Au_2@Pt/C$ at 0.9 V_{RHE} were relativelly stable.

On the other hand, data in Figure 4.12b show that the loss of elecroochemical surface area is higher in alloys compared to pure Pt. This loss of surface area appears to result from a combination of electro-catalyst particle detachment from the support and the loss of Pt in the process of electrolyte refreshing. This is less problematic for pure Pt samples since the nominal loading of Pt is significantly higher compared to the loading of Pt in alloys (i.e., even the samples that exhibit Pt loss still have significant Pt amount on the surface).

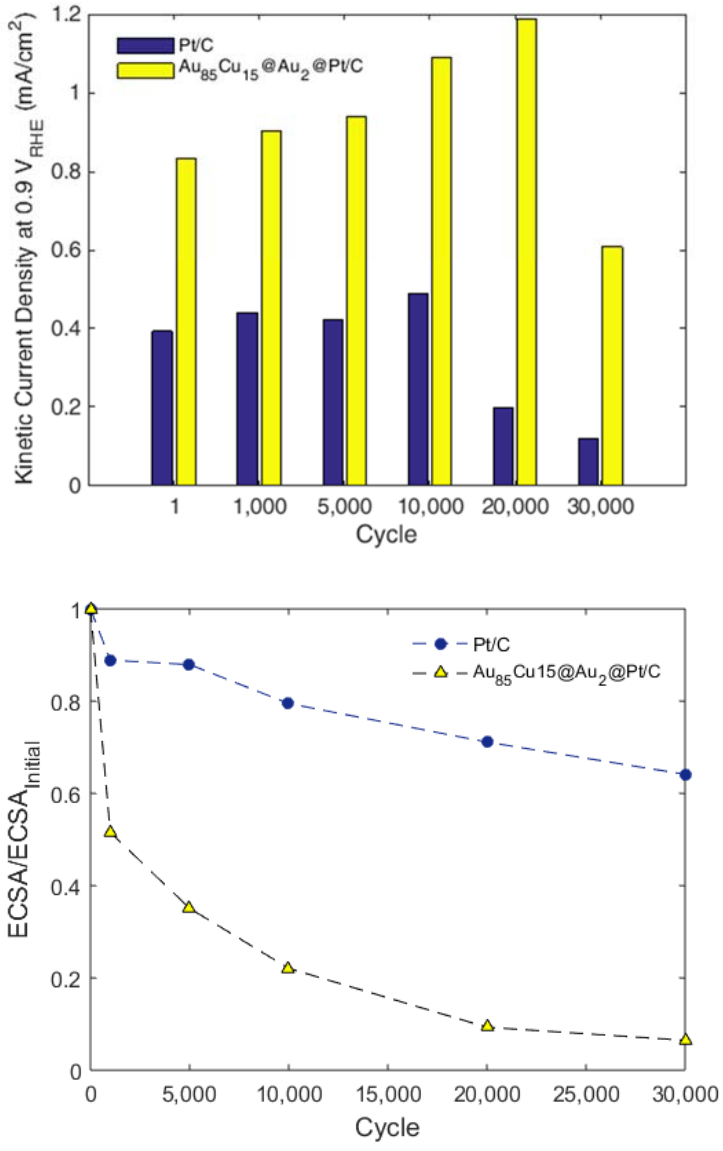

Figure 4.12. Electro-catalyst stability tests for Pt/C and $Au_{85}Cu_{15}$@Au_2@Pt/C shows degradation of specific activity and electrochemical surface area as a function of potential cycling.

4.9. Conclusions

In summary, we demonstrate that the activity of Pt alloy electro-catalysts in ORR can be improved by tuning the ligand and strain effect to produce Pt surface sites that optimize the strength of interaction between the reacting adsorbates and functioning electro-catalyst. In this particular case, we designed optimal Pt surface sites by combining the Au-Pt ligand effect with the strain effect that was manipulated by engineering of the core of nanoparticles with atomically precise composition and lattice constant. We belive that this approach holds great promise in the design of the next generation of ORR electro-catalysts and that the Au/Cu/Pt multilayer materials reported herein represent an alternative to well established Pt/3d alloy electro-catalysts.

4.10. References

1. Debe, M. K. Electrocatalyst approaches and challenges for automotive fuel cells. *Nature* **486,** 43–51 (2012).
2. Gasteiger, H. A., Kocha, S. S., Sompalli, B. & Wagner, F. T. Activity benchmarks and requirements for Pt, Pt-alloy, and non-Pt oxygen reduction catalysts for PEMFCs. *Applied Catalysis B: Environmental* **56,** 9–35 (2005).
3. Stephens, I. E. L., Bondarenko, A. S., Grønbjerg, U., Rossmeisl, J. & Chorkendorff, I. Understanding the electrocatalysis of oxygen reduction on platinum and its alloys. *Energy Environ. Sci.* **5,** 6744 (2012).
4. Wagner, F. T., Lakshmanan, B. & Mathias, M. F. Electrochemistry and the Future of the Automobile. *J. Phys. Chem. Lett.* **1,** 2204–2219 (2010).
5. Gasteiger, H. A. & Marković, N. M. Chemistry. Just a dream--or future reality? *Science* **324,** 48–9 (2009).
6. Gasteiger, H. a. *et al.* Fuel Cell Basics. *Hydrog. energy* (2010).
7. Anderson, A. B. O2 reduction and CO oxidation at the Pt-electrolyte interface. The role of H2O and OH adsorption bond strengths. *Electrochim. Acta* **47,** 3759–3763 (2002).
8. Nørskov, J. K. *et al.* Origin of the overpotential for oxygen reduction at a fuel-cell cathode. *J. Phys. Chem. B* **108,** 17886–17892 (2004).
9. Xin, H., Holewinski, A., Schweitzer, N., Nikolla, E. & Linic, S. Electronic Structure Engineering in Heterogeneous Catalysis: Identifying Novel Alloy Catalysts Based on Rapid Screening for Materials with Desired Electronic Properties. *Top. Catal.* **55,** 376–390 (2012).

10. Xin, H., Holewinski, A. & Linic, S. Predictive Structure–Reactivity Models for Rapid Screening of Pt-Based Multimetallic Electrocatalysts for the Oxygen Reduction Reaction. *ACS Catal.* **2,** 12–16 (2012).

11. Viswanathan, V., Hansen, H. A., Rossmeisl, J. & Nørskov, J. K. Universality in Oxygen Reduction Electrocatalysis on Metal Surfaces. *ACS Catal.* **2,** 1654–1660 (2012).

12. Holewinski, A., Xin, H., Nikolla, E. & Linic, S. Identifying optimal active sites for heterogeneous catalysis by metal alloys based on molecular descriptors and electronic structure engineering. *Curr. Opin. Chem. Eng.* **2,** 312–319 (2013).

13. Markovic, N. M., Gasteiger, H. A. & Ross, P. N. Oxygen Reduction on Platinum Low-Index Single-Crystal Surfaces in Sulfuric Acid Solution: Rotating Ring-Pt(hkl) Disk Studies. *J. Phys. Chem.* **99,** 3411–3415 (1995).

14. Paulus, U. A. *et al.* Oxygen Reduction on Carbon-Supported Pt−Ni and Pt−Co Alloy Catalysts. *J. Phys. Chem. B* **106,** 4181–4191 (2002).

15. Stamenkovic, V. R. *et al.* Improved oxygen reduction activity on Pt3Ni(111) via increased surface site availability. *Science* **315,** 493–7 (2007).

16. Ball, S. C., Hudson, S. L., Theobald, B. R. & Thompsett, D. PtCo, a Durable Catalyst for Automotive PEMFC? in *ECS Transactions* **11,** 1267–1278 (ECS, 2007).

17. Neyerlin, K. C., Srivastava, R., Yu, C. & Strasser, P. Electrochemical activity and stability of dealloyed Pt–Cu and Pt–Cu–Co electrocatalysts for the oxygen reduction reaction (ORR). *J. Power Sources* **186,** 261–267 (2009).

18. Stamenković, V., Schmidt, T. J., Ross, P. N. & Marković, N. M. Surface Composition Effects in Electrocatalysis: Kinetics of Oxygen Reduction on Well-Defined Pt 3 Ni and Pt 3 Co Alloy Surfaces. *J. Phys. Chem. B* **106,** 11970–11979 (2002).

19. Koh, S., Leisch, J., Toney, M. F. & Strasser, P. Structure-Activity-Stability Relationships of Pt−Co Alloy Electrocatalysts in Gas-Diffusion Electrode Layers. *J. Phys. Chem. C* **111,** 3744–3752 (2007).

20. Cui, C., Gan, L., Heggen, M., Rudi, S. & Strasser, P. Compositional segregation in shaped Pt alloy nanoparticles and their structural behaviour during electrocatalysis. *Nat. Mater.* **12,** 765–71 (2013).

21. van der Vliet, D. F. *et al.* Mesostructured thin films as electrocatalysts with tunable composition and surface morphology. *Nat. Mater.* **11,** 1051–8 (2012).

22. Stamenkovic, V. R. *et al.* Trends in electrocatalysis on extended and nanoscale Pt-bimetallic alloy surfaces. *Nat. Mater.* **6,** 241–7 (2007).

23. Stamenkovic, V. R., Mun, B. S., Mayrhofer, K. J. J., Ross, P. N. & Markovic, N. M. Effect of Surface Composition on Electronic Structure, Stability, and Electrocatalytic Properties of Pt-Transition Metal Alloys: Pt-Skin versus Pt-Skeleton Surfaces. *J. Am. Chem. Soc.* **128,** 8813–8819 (2006).

24. Choi, S. Il *et al.* Synthesis and characterization of 9 nm Pt-Ni octahedra with a record high activity of 3.3 A/mgPt for the oxygen reduction reaction. *Nano Lett.* **13,** 3420–3425 (2013).

25. Choi, S. Il *et al.* Controlling the size and composition of nanosized Pt-Ni octahedra to optimize their catalytic activities toward the oxygen reduction reaction. *ChemSusChem* **7,** 1476–1483 (2014).

26. Chen, C. *et al.* Highly crystalline multimetallic nanoframes with three-dimensional electrocatalytic surfaces. *Science* **343,** 1339–43 (2014).

27. Wang, D. *et al.* Structurally ordered intermetallic platinum-cobalt core-shell nanoparticles with enhanced activity and stability as oxygen reduction electrocatalysts. *Nat. Mater.* **12,** 81–7 (2013).

28. Stamenkovic, V. *et al.* Changing the activity of electrocatalysts for oxygen reduction by tuning the surface electronic structure. *Angew. Chem. Int. Ed. Engl.* **45,** 2897–901 (2006).

29. Menning, C. A., Hwu, H. H. & Chen, J. G. Experimental and theoretical investigation of the stability of Pt-3d-Pt(111) bimetallic surfaces under oxygen environment. *J. Phys. Chem. B* **110,** 15471–7 (2006).

30. Xin, H., Schweitzer, N., Nikolla, E. & Linic, S. Communications: Developing relationships between the local chemical reactivity of alloy catalysts and physical characteristics of constituent metal elements. *J. Chem. Phys.* **132,** 111101 (2010).

31. Schweitzer, N., Xin, H., Nikolla, E., Miller, J. T. & Linic, S. Establishing Relationships Between the Geometric Structure and Chemical Reactivity of Alloy Catalysts Based on Their Measured Electronic Structure. *Top. Catal.* **53,** 348–356 (2010).

32. Sasaki, K. *et al.* Recent advances in platinum monolayer electrocatalysts for oxygen reduction reaction: Scale-up synthesis, structure and activity of Pt shells on Pd cores. *Electrochim. Acta* **55,** 2645–2652 (2010).

33. Zhang, J., Sasaki, K., Sutter, E. & Adzic, R. R. Stabilization of platinum oxygen-reduction electrocatalysts using gold clusters. *Science* **315,** 220–2 (2007).

34. Wang, J. X. *et al.* Oxygen reduction on well-defined core-shell nanocatalysts: particle size, facet, and Pt shell thickness effects. *J. Am. Chem. Soc.* **131,** 17298–302 (2009).

35. Shao, M., Sasaki, K., Marinkovic, N., Zhang, L. & Adzic, R. Synthesis and characterization of platinum monolayer oxygen-reduction electrocatalysts with Co–Pd core–shell nanoparticle supports. *Electrochem. commun.* **9,** 2848–2853 (2007).

36. Holewinski, A. & Linic, S. Elementary Mechanisms in Electrocatalysis: Revisiting the ORR Tafel Slope. *J. Electrochem. Soc.* **159,** H864–H870 (2012).

37. Okamoto, H., Chakrabarti, D. J., Laughlin, D. E. & Massalski, T. B. The Au−Cu (Gold-Copper) system. *J. Phase Equilibria* **8,** 454–474 (1987).

38. Yang, J., Chen, X., Yang, X. & Ying, J. Y. Stabilization and compressive strain effect of AuCu core on Pt shell for oxygen reduction reaction. *Energy & Environmental Science* **5,** 8976 (2012).

39. Huang, X. & El-Sayed, M. A. Gold nanoparticles: Optical properties and implementations in cancer diagnosis and photothermal therapy. *J. Adv. Res.* **1,** 13–28 (2010).

40. Motl, N. E., Ewusi-Annan, E., Sines, I. T., Jensen, L. & Schaak, R. E. Au−Cu Alloy Nanoparticles with Tunable Compositions and Plasmonic Properties: Experimental Determination of Composition and Correlation with Theory. *J. Phys. Chem. C* **114,** 19263–19269 (2010).

41. Rudi, S., Cui, C., Gan, L. & Strasser, P. Comparative Study of the Electrocatalytically Active Surface Areas (ECSAs) of Pt Alloy Nanoparticles Evaluated by Hupd and CO-stripping voltammetry. *Electrocatalysis* **5,** 408–418 (2014).

42. van der Vliet, D. F. *et al.* Unique electrochemical adsorption properties of Pt-skin surfaces. *Angew. Chem. Int. Ed. Engl.* **51,** 3139–42 (2012).

43. Bandarenka, A. S. *et al.* Design of an active site towards optimal electrocatalysis: overlayers, surface alloys and near-surface alloys of Cu/Pt(111). *Angew. Chem. Int. Ed. Engl.* **51,** 11845–8 (2012).

44. Pedersen, C. M. *et al.* Benchmarking Pt-based electrocatalysts for low temperature fuel cell reactions with the rotating disk electrode: oxygen reduction and hydrogen oxidation in the presence of CO (review article). *Electrochim. Acta* (2015). doi:10.1016/j.electacta.2015.03.176

45. Perez-Alonso, F. J. *et al.* The effect of size on the oxygen electroreduction activity of mass-selected platinum nanoparticles. *Angew. Chem. Int. Ed. Engl.* **51,** 4641–3 (2012).

46. Garsany, Y., Singer, I. L. & Swider-Lyons, K. E. Impact of film drying procedures on RDE characterization of Pt/VC electrocatalysts. *J. Electroanal. Chem.* **662,** 396–406 (2011).

47. Garsany, Y., Baturina, O. A., Swider-Lyons, K. E. & Kocha, S. S. Experimental methods for quantifying the activity of platinum electrocatalysts for the oxygen reduction reaction. *Anal. Chem.* **82,** 6321–8 (2010).

48. Koenigsmann, C. *et al.* Enhanced electrocatalytic performance of processed, ultrathin, supported Pd-Pt core-shell nanowire catalysts for the oxygen reduction reaction. *J. Am. Chem. Soc.* **133,** 9783–95 (2011).

Chapter 5

Enhancing ORR activity on Pt monolayer electrocatalysts through selective tuning of ligand and lattice effects

5.1. Summary

In this chapter, we describe the design of Pt monolayer alloy ORR catalysts with novel structure, which enables specific control over chemical ligand and lattice strain effects that influence the activity of Pt surface atoms. Guided by quantum chemical calculations, we prepared Au_xCu_{1-x}@Au@Pt nanoparticle electrocatalysts where OH affinity and catalytic activity are manipulated by changing the composition of the nanoparticle core. In these materials, increased Cu content leads to a compressive strain relative to pure Au that weakens OH binding energies. By tuning the strength of OH-surface bond, different alloys can exhibit superior or inferior ORR activity compared to Pt standards. This chapter will focus on how the interactions between the Pt surface layer and the nanoparticle core modify catalytic activity across this alloy series. Experimental results are discussed which validate the structure-activity relationships proposed by DFT calculations.

5.2. Introduction

Platinum-based electrocatalysts are utilized in low temperature fuel cells to improve the kinetics of both hydrogen oxidation and oxygen reduction reactions.[1–3] Unfortunately, overpotential losses associated with the oxygen reduction reaction (ORR) at the cathode greatly limit overall fuel cell performance.[2] The Department of Energy has establish a variety of benchmarks that highlight the need to develop cheaper, more active, and stable

ORRelectrocatalysts compared to state-of-the-art support Pt nanoparticles.[4] In general, the mass activity of Pt-based ORR catalysts must be increased 2-10 fold in order for fuel cells to become an economically viable alternative to internal combustion engines.[2]

One strategy to achieve improved performance is to maximize the atomic utilization of Pt by concentrating Pt atoms at the surface where they can catalyze the reaction.[5–12] Pt monolayer catalysts have an atomic surface layer of Pt, and therefore all atoms can participate in the ORR. Assuming there is no change in the specific catalytic activity (activity normalized by surface area), the mass activity of 8 nm Pt monolayer spherical electrocatalysts can be up to 10 times higher compared to pure Pt nanoparticles when neglecting the cost of the particle core. The interactions between the Pt surface layer and the core can also improve the activity and stability of Pt monolayer catalysts compared to pure Pt catalysts.

The electronic properties of the Pt surface, which ultimately govern its catalytic activity, are extremely susceptible to changes in the local chemical environment;[7,13–19] it is essential to understand how catalytic behavior of Pt monolayer electrocatalysts will change in response to alloying effects. Both chemical ligand and lattice strain effects have been shown to improve the oxygen reduction activity of Pt alloy electrocatalysts. By replacing Pt in the subsurface layer with another element, a chemical ligand effect can be induced even when there is no geometric induced strain.[16] Each element has different spatial extent of *d*-orbitals and electronegativity. Differences in these properties have been shown to affect electronic properties of the Pt surface by changing the *d*-band structure (width and center) and adsorbate-surface bond distance through partial *sp*-electron charge transfer.[20] These perturbations in electronic structure can cause Pt monolayer electrocatalysts to interact slightly more weakly with OH intermediates thereby improving the intrinsic ORR activity of surface atoms compared to pure Pt.[17,20] Pt monolayer alloys with

subsurface 3*d* metals like Ni and Co have slightly lower OH affinities compared to pure Pt and therefore exhibit superior ORR activity.[17,21] Other alloys containing subsurface Ru, Re, Os, and Ir have a ligand effect that strengthens the OH-surface bond leading to inferior ORR performance.[7,17] The magnitude of the ligand effect is strongly dependent on the subsurface elements.

Lattice strain effects acting on Pt surface atoms can also influence trends in adsorption energies. If an alloy has a compressed lattice relative to Pt, the orbitals of surface atoms will have greater overlap which will lead to stronger interactions between surface atoms and weaker interactions with adsorbates.[15–17] Conversely, Pt surfaces with expanded lattices bind adsorbates stronger due to weaker interactions between surface atoms. The sensitivity of OH binding energy to Pt-Pt spacing is heavily dependent on the subsurface element and the composition of the alloy core. Unfortunately, it is very difficult to selectively control lattice and ligand effects when preparing Pt alloys because the relative strengths of these effects are heavily dependent on the composition and near-surface structure. Herein, we develop a family of Pt alloy electrocatalysts with constant ligand effect whose activity is modified by the lattice strain effect induced by the particle core composition. Results of electrochemical tests and nanoparticle characterization support ORR activity trends predicted by quantum chemical calculations.

5.3. Theoretical and Experimental Methods

5.3.1. DFT calculations

All DFT calculations were carried out with the GPAW plane wave code (https://wiki.fysik.dtu.dk/gpaw/) using the generalized gradient approximation and revised Perdew, Burke and Ernzerhof exchange correlation functional. All surface calculations used a five-layer 2 × 2 fcc [111] periodic unit cell separated by 15 Å of vacuum space in the [111] direction and a dipole layer to decouple the slabs electrostatically. The bottom two layers were fixed and

the top three layers and all adsorbates were relaxed until the sum of forces was below 0.05 eV $Å^{-1}$. Ultra-soft pseudopotentials were used to represent the ionic cores, with the valence electron density determined through iterative diagonalization of the Kohn–Sham Hamiltonian using Pulay mixing. An electronic temperature of 0.1 k_BT was used, with final energies extrapolated to 0 K. Lattice constants for Au, Cu, Pt, and AuCu alloys were calculated using bulk fcc crystal unit cells containing 4 atoms with a 8 x 8 x 8 *k*-point grid. The adsorption energies for O, OH, OOH, and CO on various alloy surfaces were measured relative to the unperturbed Pt111 surface at ¼ surface coverage. All adsorbates except O bind to Pt surface through the top site while O prefers the three-fold fcc site. For adsorption energy calculations, unit cells were sampled with a $6 \times 6 \times 1$ Monkhorst–Pack *k*-point grid, and the plane-wave basis-set energy cutoff was 340 eV. Projected density of states were calculated to determine *s*, *p*, and *d*-band structure on relaxed Pt alloy surfaces with 24 x 24 x 1 *k*-points.

5.3.2. Synthesis of AuCu@Au@Pt/C Electrocatalysts

In this study, Pt alloy electrocalysts were prepared by following the procedure described in Chapter 4. In general, AuCu alloy cores were synthesized by thermally reducing gold (III) chloride trihydrate ($AuCl_3 \cdot 3H_2O$, Sigma Aldrich) and copper acetylacetonate ($Cu(acac)_2$, Fisher) precursors in 20 mL of oleylamine in an Ar-purged reflux condenser. The nominal loadings of Au and Cu precursors were varied to maintain constant metal loading across samples. In this study, the activities of alloy cores between 65 – 100 % Au content were compared.

The rinsed alloy nanoparticles were deposited onto pre-treated carbon (Vulcan XC72R-Cabot) at roughly 20 wt% Au loading in hexane and allowed to mix under continuous stirring for at least 24 hours. After mixing, supported nanoparticles would settle and samples were collected by rinsing the sample with isopropanol (IPA) and concentrating sample by centrifugations (another

3 washes at 8000 rpm for 8 minutes). The supported nanoparticles (AuCu/C) were collected in pure ethanol and allowed to dry in the oven overnight. The supported cores were characterized by XRD, ICP-AAS, and TEM/STEM to verify synthesis of intermetallic alloy nanoparticles. Powders were thermally treated for 5 hours in air at 185°C prior to electrochemical preparation in order to remove excess oleylamine from nanoparticle surface.

Atomic layers of Au and Pt were epitaxially grown on supported AuCu cores via galvanic replacement of a sacrificial Cu adlayer to achieve the desired nanostructure represented in Fig. 1b. Cu monolayers were deposited onto Au using the copper underpotential deposition (Cu UPD) phenomena.[22–24,12] Multiple sweeps to higher potentials were performed to verify similar amount of Cu were deposited on consecutive scans. After removing the electrode under potential control, the electrode was rinsed with ultrapure water (18.2 MΩ·cm (Millipore)) and deposited into a solution containing either 1μM $AuCl_3$ or K_2PtCl_4. 2/3 ML of Au or 1 ML Pt will deposit for every 1 ML of Cu removed so 3 deposition cycles are required for Au and another for the Pt monolayer to prepare the AuCu@Au_2@Pt structure. After depositing Au/Pt over a few minutes, the electrode was rinsed to remove excess metal precursors before continuing depositions or beginning electrochemical testing. Samples were characterized with electron microscopy before and after ORR activity and electrochemical surface area measurements.

5.3.3. Electrochemical Testing

Electrochemical measurements were performed at room temperature in a custom-made, all-Telfon three-electrode cell with a Gamry Instruments Reference 3000 potentiostat/galvanostat/frequency response analyzer. The working electrodes were prepared by sonicating the catalyst powders in absolute ethanol (Fisher) at 0.75 mg mL^{-1} for > 1 hr. A uniform film of catalysts was achieved by depositing four 10 μL droplets onto a 5 mm glassy carbon

electrode insert (Pine Instruments) at a rotation around 600 rpm using the inverted RDE. All electrochemical measurements were performed in 0.1 M $HClO_4$. The reference electrode was Ag/AgCl in 3 M KCl with saturated AgCl (Radiometer Analytical) and counter electrodes (Pt wire, Alfa Aesar) were both in isolated compartments connected by capillaries to the working electrode chamber.

Electrolyte solutions of 0.1 M $HClO_4$ were prepared from ultrapure water and 70% perchloric acid (Merck Suprapur). A consistent uncompensated resistance of ~25 Ω was measured with high-frequency impedance, and was corrected for in the polarization curves. All potentials are reported relative to the reversible hydrogen electrode which is calibrated against the H_2 oxidation equilibrium at the pH of the solution. Reported currents have been corrected for capacitance and uncompensated solution resistance. Sample capacitance was measured by comparing the differences in the limiting current (around 0.3-0.5 V_{RHE}) between forward and reverse scans during the electrode conditioning scans in O2 saturated electrolyte at 100 mV s^{-1} between 0.05 and 1.0 V_{RHE}.

Cyclic voltammetry was performed in Ar-purged electrolyte by scanning the potential between 0.05 and 1.00 V_{RHE} at 50 mV s^{-1}. ORR polarization curves were measured in O_2-saturated electrolyte at rotation rates of 400, 900, 1600, and 2500 rpm. ORR rates were recording during a linear potential sweep between 0.05 and 1.00 V_{RHE} at 50mV s^{-1}. CO-stripping voltammetry was performed immediately following post-polarization CV scans by holding the working electrode at 0.05 V_{RHE} as CO was bubbled (5 minutes) followed by an Ar gas purge (20 minutes) to remove excess CO from solution. The electrode potential was then scanned to 1.0 V_{RHE} at 10 mV s^{-1}.

5.3.4. Catalyst Characterization

UV-visible absorption spectroscopy (UV-vis) experiments were performed using a Thermo Scientific Evolution 300 UV-Vis spectrophotometer with a Xenon lamp source to measure the extinction spectra of dilute AuCu nanoparticle suspensions in hexane. UV-vis spectra were collected between 300 and 1000 nm at a rate of 240 nm min^{-1} and were normalized by the extinction peak signal intensity to facilitate comparison of samples with different concentrations. XRD measurements were conducted in a Rigaku rotating anode diffractometer with a monochromated Cu Kα X-ray source at a scan rate of 5° min^{-1}. Ion coupled plasma optical emission spectroscopy was performed on samples dissolved in aqua regia (3:1 mixture of concentrated HCl and HNO3) using a Perkin-Elmer Optima 2000DV with Winlab software to determine the molar composition of bulk AuCu nanoparticles. Au and Cu signals were normalized by 2 ppm Yttrium internal standard and concentrations were measured three times using calibrated standards of 0, 1, 2, 5, 10, 20, and 40 ppm Au and Cu solutions.

Aberration-corrected STEM imaging and sub-nm resolution STEM-EDS were performed at the Center for Nanophase Materials Sciences at Oak Ridge National Laboratory with a JEOL 2200FS TEM/STEM equipped with a CEOS aberration (probe) corrector and operated at a 200 kV accelerating voltage. The microscope was operated in high angle annular dark field (HAADF)-STEM imaging mode and was equipped with a Bruker AXS X-Flash 5030 silicon drift detector. The probe size was ~0.7 Å and the probe current was ~30 pA during HAADF-STEM imaging. When collecting the EDS spectrum image data, the probe current was increased to ~280 pA and the probe size was ~2 Å.

X-ray absorption spectroscopy studies were performed on the MRCAT 10-ID-B beamline located at Argonne National Laboratory's Advanced Photon Source (ANL-APS). Data was collected at Pt L_3 (11564 eV) and Au L_3 (11919 eV) edges. Scans of XANES and XAFS regions

were collected in fluorescence mode using Ar ion chambers. Thin films of supported electrocatalysts on Kapton tape were positioned 45° relative to the beam path. This configuration enabled the simultaneous measurement of reference foil spectra in transmission mode and sample fluorescence. Zn and Ga foils were used as filters for Pt and Au fluorescence measurements. XAS data processing and analysis were performed using Athena and Artemis software packages following standard analysis procedures to normalize absorption spectra and scattering parameter fitting.

5.4. Adsorption energy trends on Pt monolayer surface

In order to control chemical ligand and lattice strain effects on Pt monolayer electrocatalysts, we designed nanoparticles with a layered structure to independently tune these effects. Since the chemical ligand effect strongly depends upon the immediate subsurface layers, Pt surface atoms are deposited onto a buffer layer (in this case Au), which electronically isolates surface atoms from the core. The nanoparticle core impacts activity by largely determining the interatomic spacing between surface atoms. Previous studies have shown that epitaxial layers several atoms thick are insufficient to drastically dampen lattice strain effects.[5,10,11] As a consequence, the lattice strain effect only depends on the lattice parameter of the core.

In this study, Pt monolayer catalysts with a subsurface Au buffer were studied for several reasons. First, Au is highly resistant to oxidization, even at PEM conditions. This property will help prevent dissolution of less noble metals from the particle core. Second, there is a ligand effect on these Au/Pt skin alloys which significantly destabilizes OH adsorption on Pt surface.[17,25] Finally compared to other alloy systems, the OH binding energy is highly sensitive to the lattice effect, leading to dramatic differences in catalytic activity for different alloy cores.

A Pt monolayer on a Au core has been shown to exhibit inferior ORR activity compared to pure Pt electrodes. This is a result of the large lattice expansion induced on Pt surface atoms by the Au core. For Au@Pt catalysts, the attractive lattice effect overcomes the destabilizing ligand effect to create a stronger OH-surface bond. In order to weaken the OH-surface interaction, a slight lattice compression must be induced by the core. However, if the core becomes too compressed, the OH adsorption will weaken too far and ORR activity will diminish due to difficulties with the O_2 activation step. For compatibility reasons discussed in Chapter 4, Pt alloy nanoparticles with different AuCu alloy cores were analyzed.

In order to better understand the role of ligand and lattice effects on Au@Pt alloy surfaces, several DFT calculations were performed to assess the role of Au buffer layer thickness on OH binding energy at several different lattice constants. The data in Figure 5.1 show that the introduction of the first Au subsurface layer dramatically destabilizes OH adsorption by at least 0.2 eV compared to pure Pt slabs with similar lattice stain. The addition of a second Au layer destabilizes adsorption energies slightly compared to single Au layer structures. However, there are only minute differences between Pt monolayer surfaces with two Au subsurface layers and those deposited on a pure Au slab. This result indicates that atoms within the particle core (not located in first 2 subsurface layers) have little impact on the ligand effect. DFT calculations on various $Au_xCu_{1-x}@Au_2@Pt$ surfaces show similar OH binding energies compared to Au@Pt and $Pt@Au_2@Pt$ surfaces. Comparison of the slopes in Figure 5.1 shows that Pt has a less pronounced lattice strain effect compared to Pt@Au@Pt and $Pt@Au_2@Pt$, consistent with previous Pt-alloy screening studies. Similar lattice strain effect trends were observed for Pt monolayer catalysts deposited onto various AuCu cores.

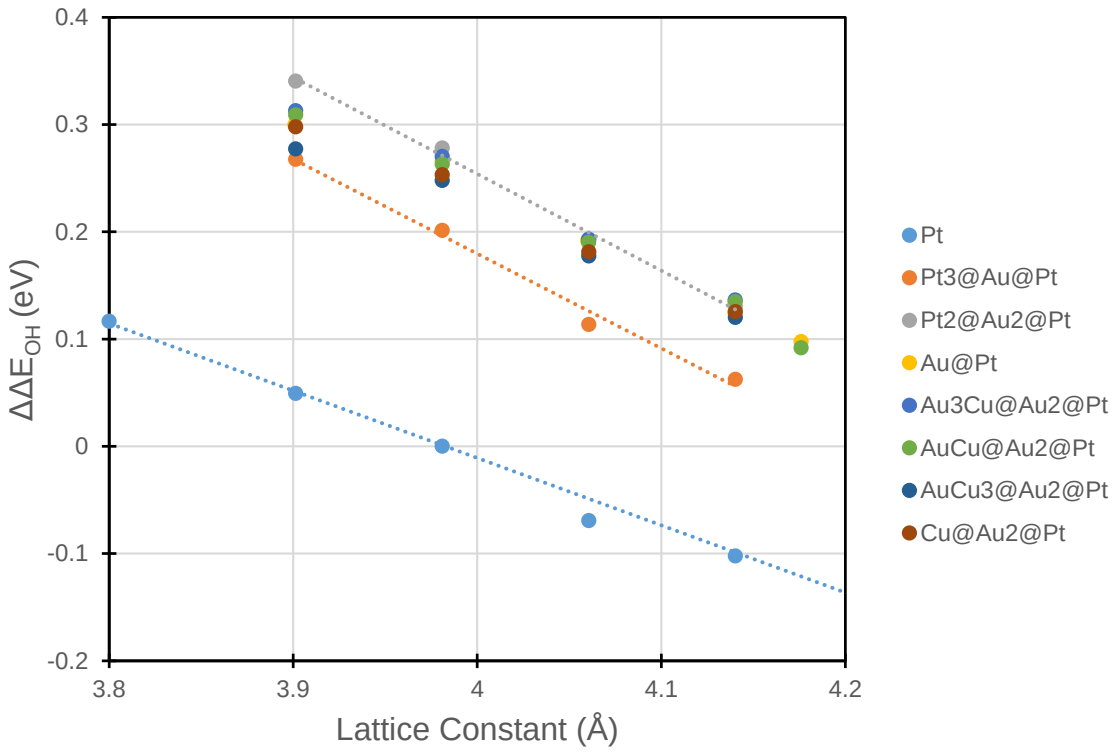

Figure 5.1. Relative OH adsorption energy on various Pt alloy (111) slabs as a function of lattice spacing.

Equilibrium lattice constants were calculated for Au, Au_3Cu, Au_2Cu_2, $AuCu_3$, and Cu alloys and the adsorption energies for Pt_{ML} alloy surfaces were calculated as a function of Au buffer layer thickness on AuCu cores. The data in Figure 5.2 compares the adsorption energy of O, OH, OOH, and CO on different Pt monolayer 111 surfaces with 0, 1, or 2 Au subsurface layers deposited on different AuCu alloy cores. The introduction of subsurface Au layers strengthen the adsorbate-surface bond compared to Au_xCu_{1-x}@Pt because the AuCu core interacts more strongly with Pt surface layer than Au buffer layers. For the alloy cores, the thickness of the Au buffer layer does not significantly impact adsorption energies indicating that a single atomic layer of Au atoms may be sufficient to dampen Pt surface and AuCu core interactions. Of note, Cu@Au@Pt and $Cu@Au_2$@Pt surface calculations were performed, but these results are not included because

severe lattice strain on the Au layers would induce surface reconstruction as the adsorbate binds to the surface.

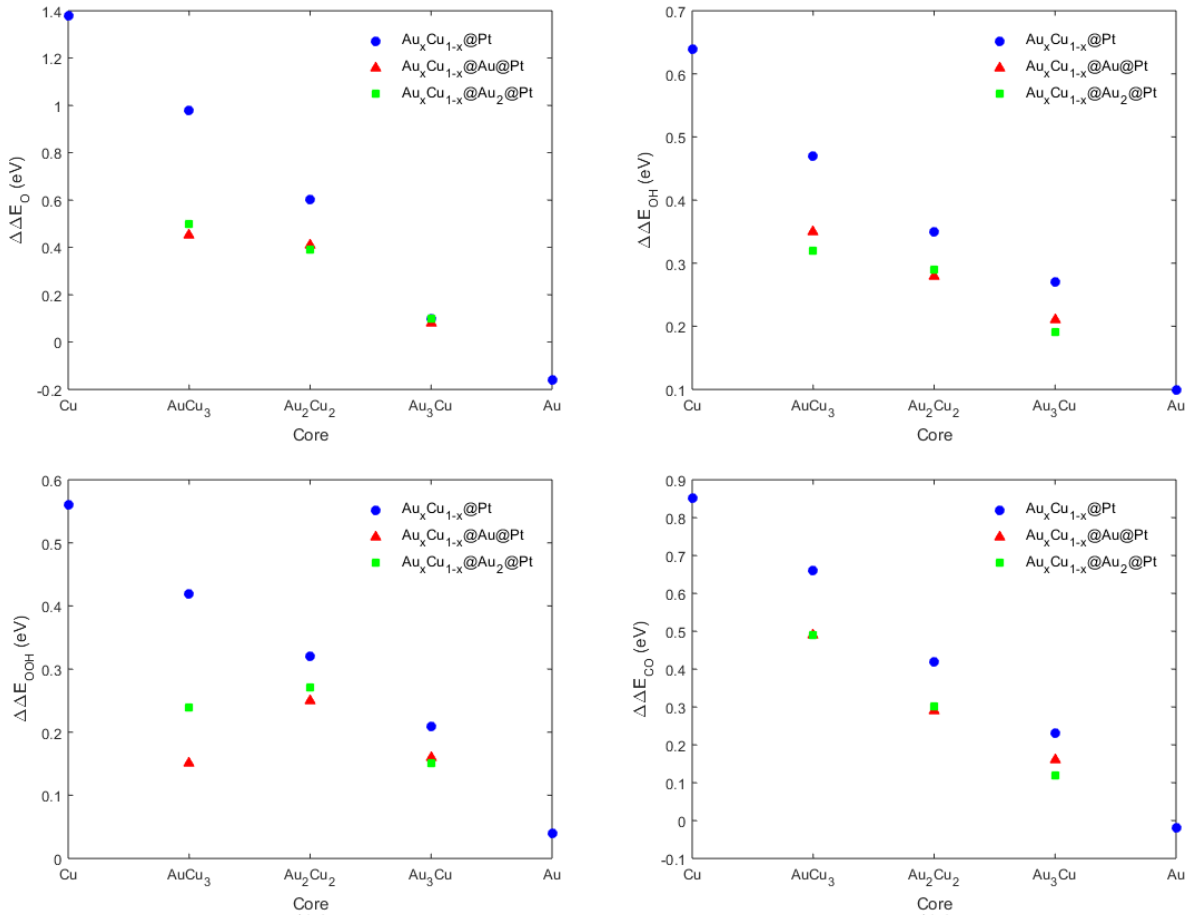

Figure 5.2. Adsorption energies of O, OH, OOH, and CO species on $Au_xCu_{1-x}@Au_y@Pt$ catalysts.

Across the AuCu@Au@Pt alloy series, it has been shown the subsurface Au layers are vital to control the strength of the chemical ligand effect and the composition of the AuCu core can independently tune the lattice strain effects. Interactions between the Pt surface atoms and subsurface Au atoms weaken bonds between adsorbates on Pt surfaces compared to unperturbed Pt, however compressive strain must be induced to achieve the optimal OH affinity (around ~ 0.1 - 0.2 eV weaker than Pt(111) surface) in order to maximize ORR activity. In this work, the activity

of Pt_{ML} nanoparticle electrocatalysts with Au buffer and AuCu alloy cores will be manipulated as a function of core composition. Specifically, cores with 65 – 100 % Au content will be investigated, because samples with higher Cu content were not stable during and following the electrochemical preparation and testing.

5.5. Characterization of AuCu and AuCu/C samples

Various characterization techniques such as UV-vis extinction spectroscopy, powder X-ray diffraction, ion-coupled plasma atomic emission spectroscopy, and electron microscopy were utilized to verify the catalyst nanostructure at various intervals during synthesis and testing. The interpretation of these results follows similar reasoning to results described in Chapter 4, therefore there will only be a brief discussion of these characterization results highlighting the trends observed over a larger range of concentrations. Details of synthesis procedure and experimental measurements were previously described in Section 5.3.

Following the colloidal synthesis of AuCu nanoparticle cores, the optical properties of these materials were measured. The data in Figure 5.3 show the UV-Vis extinction spectra for various compositions of AuCu alloy nanoparticles. The high wavelength extinction feature is the consequence of the excitation of localized surface plasmon resonance (LSPR). The data show that pure Au nanoparticles exhibit an LSPR extinction feature at ~510 nm, which is characteristic for Au nanoparticles of ~ 10 nm diameter.[26] As the content of Cu in the nanoparticles increases the LSPR peak is red-shifted to higher wavelengths. This LSPR red shift is an unambiguous characteristic of the formation of AuCu alloy nanoparticles.[27] The red shift is accompanied by an increase in the low wavelength extinction. This is the consequence of inter-band ($d \rightarrow sp$) electronic transitions in Cu atoms, which are of lower energy (higher wavelength) than the corresponding transitions in Au.[27]

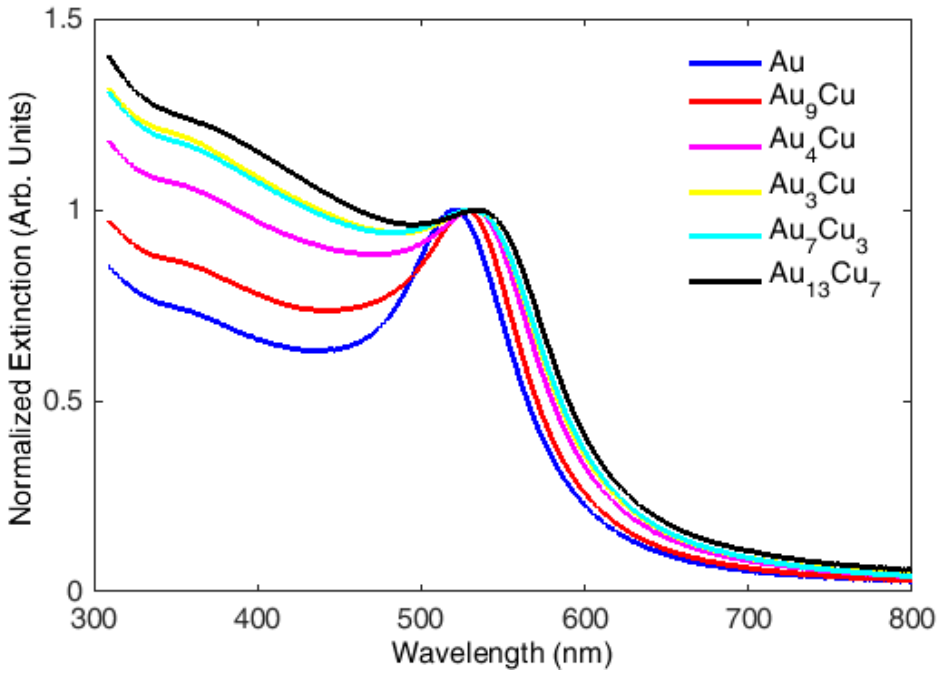

Figure 5.3. Normalized UV-vis light extinction spectra of AuCu nanoparticles in hexane.

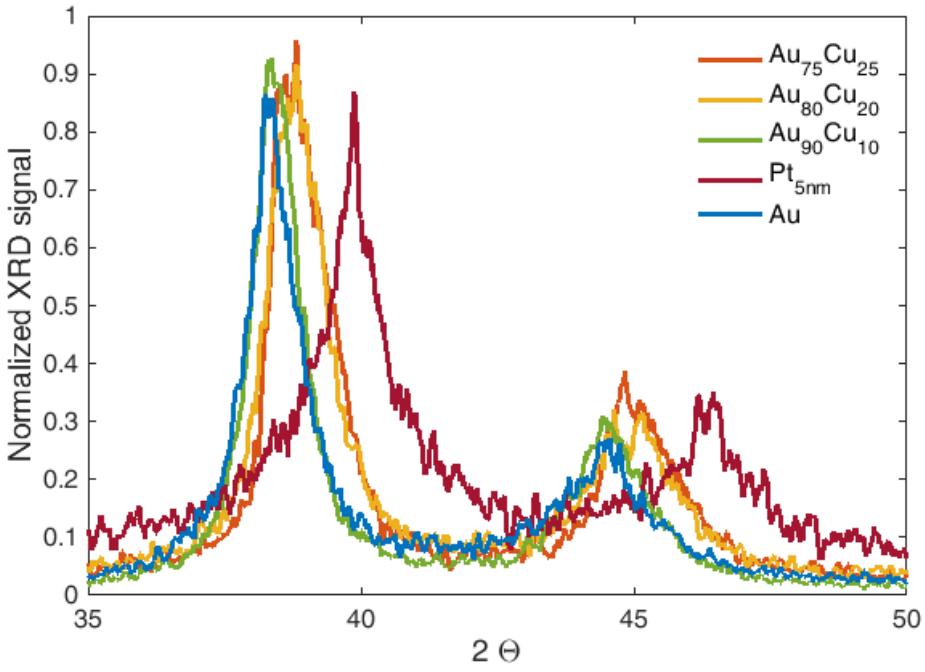

Figure 5.4. Powder x-ray diffraction patterns of supported AuCu catalysts compared to pure Au and Pt nanoparticles.

AuCu nanoparticles supported on carbon (AuCu/C) were also characterized using powder X-ray diffraction (XRD). The data in Figure 5.4 show the diffraction patterns for several AuCu alloys as well as pure Au and Pt nanoparticles. Diffraction patterns of AuCu alloys show no evidence of distinct bulk Au or Cu phases. Samples with higher Cu content have more compressed lattices relative to Au as indicated by diffraction peaks located at higher angles. Analysis of diffraction peak locations demonstrate that alloys have lattice parameters in between those of Pt and Au.

5.6. STEM/EDS imaging of AuCu@Au$_2$@Pt/C

After supporting the AuCu nanoparticles on carbon, Au and Pt layers were deposited electrochemically on these nanoparticles by the galvanic replacement of under-potentially deposited Cu layers. The electrocatalyst nanostructure was verified using bright field scanning transmission electron microscopy (BF-STEM) coupled with energy-dispersive X-ray spectroscopy (EDX) to determine the spatial distributions of Au, Cu, and Pt atoms. Elemental maps of as-prepared catalysts show that the Pt signal is concentrated on the edges of the particle while Au and Cu are intermixed within the particle core. Characterization on different Pt alloys samples after ORR activity and ECSA measurements indicates catalyst nanostructure was maintained after exposure to ORR conditions. Only after extended stability testing experiments, there was evidence of Pt dissolution and particle aggregation.

5.7. Electrochemical Performance of AuCu@Au$_2$@Pt/C

ORR activity measurements were performed in the thin-film rotating disk electrode (RDE) configuration at rotation rates of 400, 900, 1600, and 2500 rpm. Kinetic current densities were calculated using the Koutecky-Levich equation. First, kinetic current was computed using $|i_k(V)| = (1/|i(V)| - 1/|i_L|)^{-1}$, where i is the measured current, i_k is the kinetic current, and i_L is the limiting

current measured between 0.3 and 0.6 V_{RHE}. To quantitatively assess the kinetic activities of the alloys and compare these to the systems containing commercial Pt electro-catalysts, it is critical to rigorously measure the surface area of the nanoparticle electro-catalysts. The electrochemical surface area (ECSA) of the electro-catalysts was determined using CO stripping measurements. The kinetic current was then normalized by these ECSA to obtain kinetic current density (j_k). Data in Figure 5.5 show the kinetic current density as the function of potential for pure Pt and the alloy materials. The data show that across the entire potential range of interest the alloys outperform the commercial Pt standard. The data also show that pure Pt and the Pt alloy electrocatalysts exhibit similar Tafel behavior, suggesting that ORR proceeds through a similar mechanism on these electrocatalysts.[28]

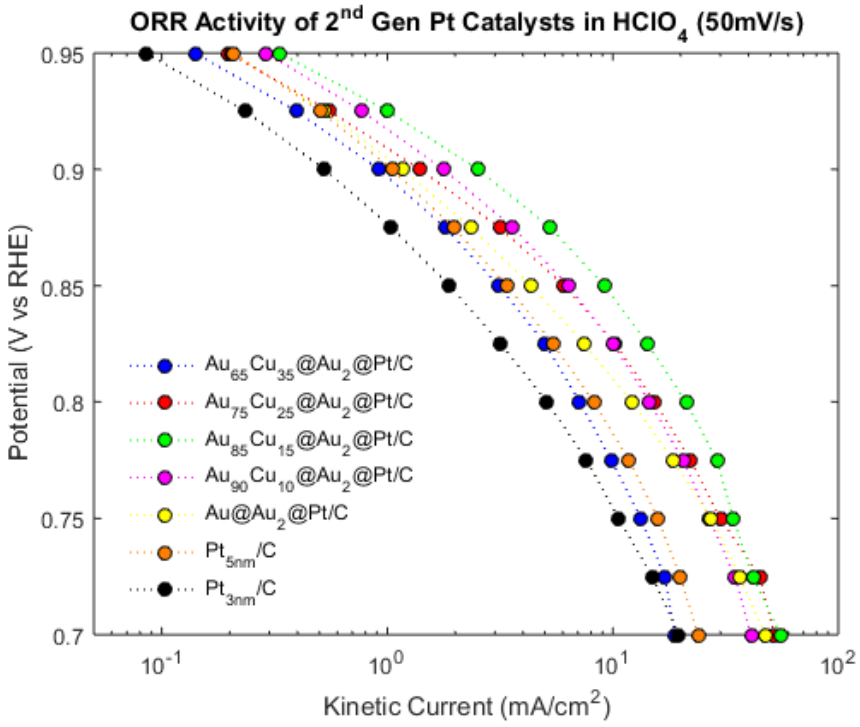

Figure 5.5. Tafel plots comparing the ORR activity of Pt alloys with pure Pt standards as a function of electrochemical potential.

Data in Figure 5.6 show the kinetic current densities of Pt alloys and Pt/C standards measured at 0.9 V_{RHE}. The data show that the current for the commercial Pt/C (5 nm) is roughly

1.0 mA/cm^2, which is consistent with other reports in the literature showing that if rigorously measured, the 5 nm Pt nanoparticle electro-catalysts exhibit ORR activities between 0.8-1.2 mA/cm^2 at these conditions.[29] The data also show that most alloy samples exhibit superior ORR performance compared to the commercial Pt standard. It is also important to account for the impact of the size of nanoparticles on the activity. The larger size of Pt alloy nanoparticles (10-15 nm diameter) compared to Pt standards (2-5 nm diameter) would lead to higher specific activities due to particle size effects, resulting from the lower concentration of under-coordinated sites on larger particles. Pt nanoparticles larger than 10 nm exhibit similar specific activities compared to polycrystalline electrodes. In order to truly account for specific activity enhancements due to alloying effects independent of size effects, our Pt alloys should be compared against polycrystalline ORR activity. Pt film electrodes exhibit the highest reported intrinsic ORR activity for Pt electrodes, measured to be between 1.7-2.0 mA/cm^2 at 0.9 V_{RHE}.[30,31]

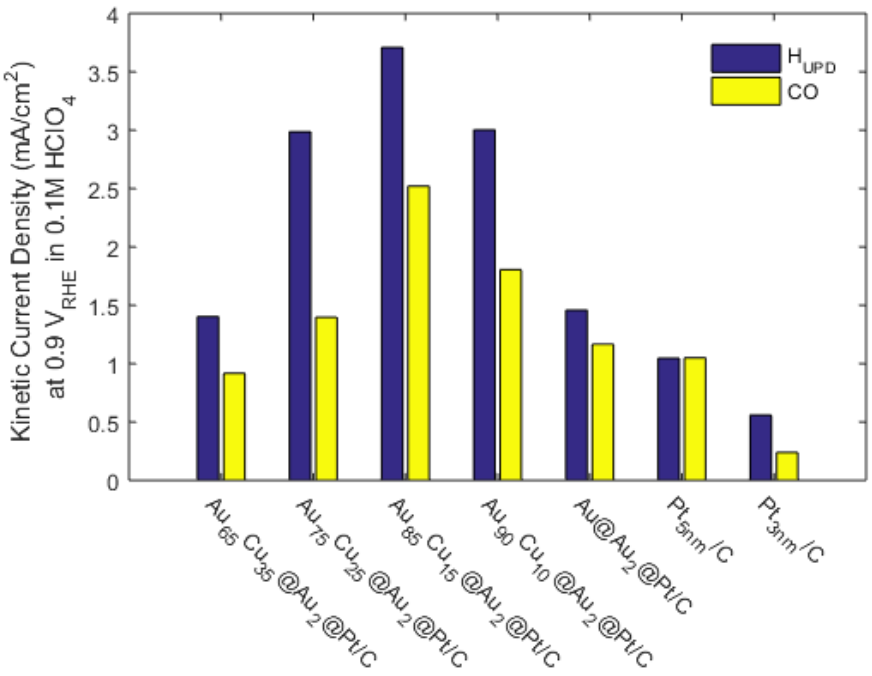

Figure 5.6. Specific current densities of electrocatalysts measured at 0.9 V_{RHE}.

Correcting for particle size effects, Au@Pt electrocatalysts exhibit inferior ORR activity compared to similarly sized Pt nanoparticles. By slightly increasing the Cu content within the nanoparticle core, the ORR activity improves for $Au_{90}Cu_{10}@Au_2@Pt$ and $Au_{85}Cu_{15}@Au_2@Pt/C$ samples. After a critical core composition, further compression of the alloy core has a detrimental impact on ORR activity as shown by $Au_{75}Cu_{25}@Au_2@Pt/C$ and $Au_{65}Cu_{35}@Au_2@Pt/C$ samples. The activity trends reported for our Pt alloy samples are consistent with previously established relationships between OH affinity and ORR activity. These results are also consistent with our expectations from our theoretical model.

We hypothesized that the main reason for the performance trend of the Au-Cu-Pt electro-catalysts results from weakening OH-surface interactions with more compressed alloy cores. The data in Figure 5.7 shows cyclic voltammograms (normalized by ECSA) for Pt and the alloy electro-catalysts measured in Ar-purged 0.1M $HClO_4$. All samples exhibit the main features characteristic of Pt electrodes: H adsorption at low potentials (0.0 – 0.4 V_{RHE}), increasing OH coverage around 0.7 V_{RHE}, and further surface oxidation at higher potentials. Compared to Pt, both alloys exhibit weaker surface OH features and the onset of surface oxidation occurs at higher potential, which is consistent with a weaker binding of oxygneted surface intermediates.

The data in Figure 5.8 shows the CO stripping curves for the electro-catalyst measured in 0.1M $HClO_4$ on the RHE potential scale. Pt alloys with higher Cu content exhibit the CO oxidation peaks located at slightly lower potentials relative to pure Pt, which is also consistent with weaker binding of CO and other intermediates (potentially including OH) involved in the CO stripping process on the alloys.[32,33] Conversely, Au@Pt catalysts consistently show CO stripping peaks at significantly higher potentials compared to Pt/C standards indicating strong interactions with CO and OH adsorbates.

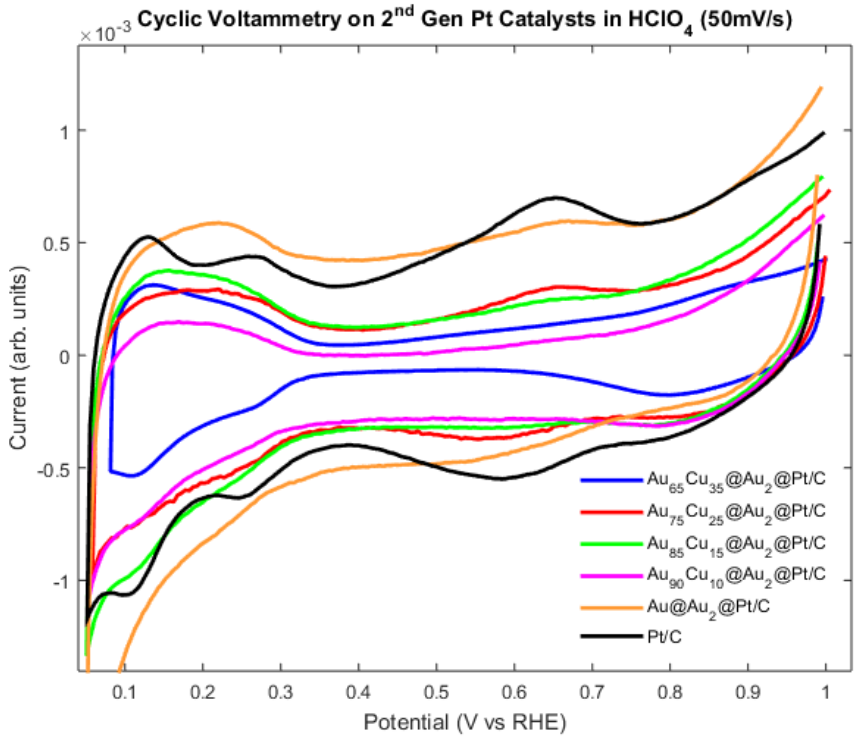

Figure 5.7. Cyclic voltammetry curves on Pt alloy electrocatalysts in 0.1M $HClO_4$.

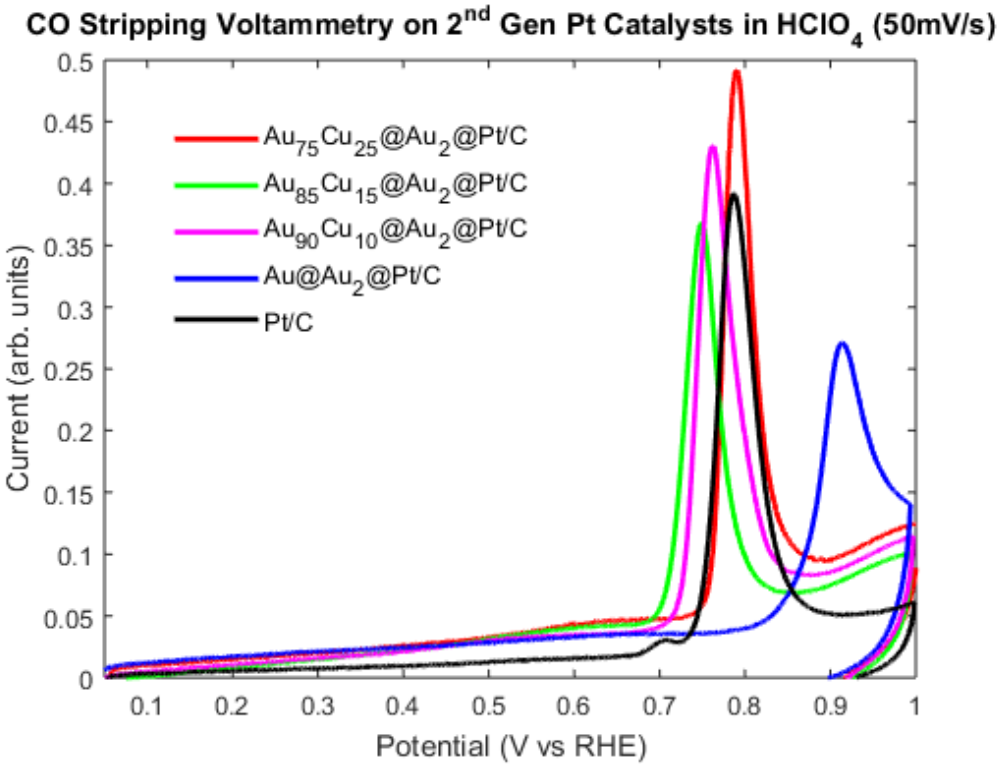

Figure 5.8. CO stripping spectra of Pt alloy electrocatalysts.

5.8. Perturbations in electronic structure of $Au_xCu_{1-x}@Au_2@Pt/C$

Perturbations in the electronic structure of Pt surface atoms induced by ligand and lattice effects can be measured by *ex-situ* X-ray absorption spectroscopy measurements. Changes in *d*-band width or Pt Fermi energy will coincide with changes in Pt edge peak shape and location, respectively.[34] Examining the oscillations in the EXAFS regions will reveal information about the local geometry of catalytic sites such as the coordination number to different species and their respective bond distances. The X-ray absorption of supported Pt monolayer electrocatalysts with core compositions between 70 and 100 % Au were measured and compared against Pt/C.

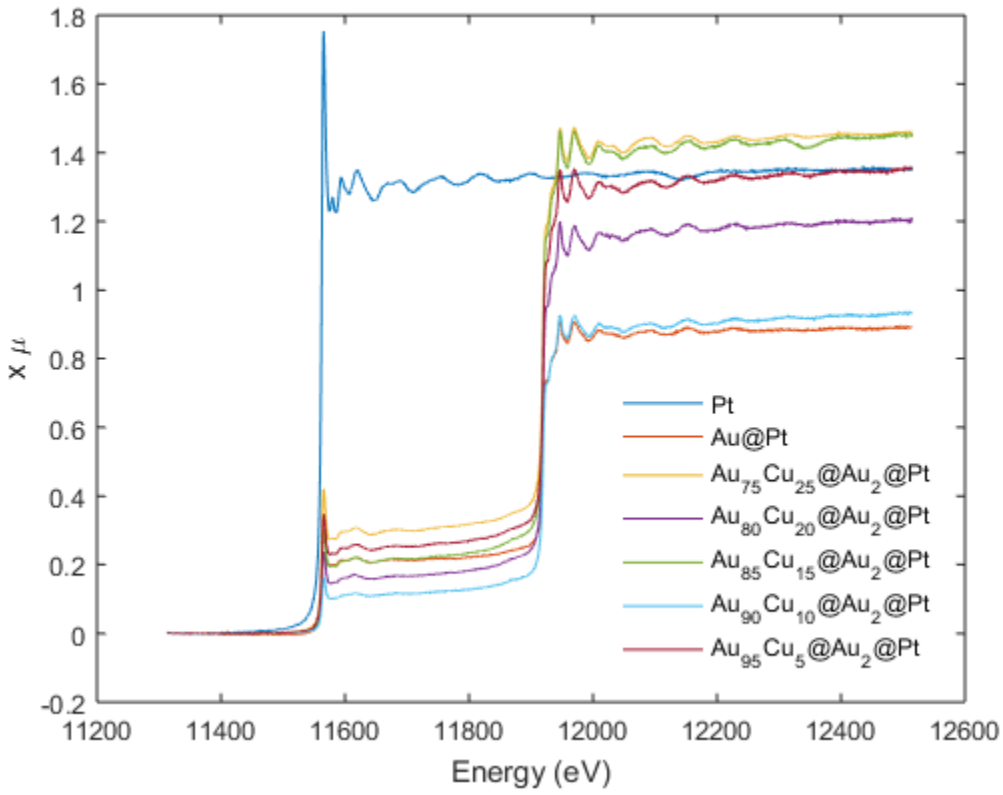

Figure 5.9. X-ray fluorescence spectra for Pt and Pt alloy nanoparticles.

The data in Figure 5.9 compares the extended X-ray fluorescence signal for Pt and Pt alloy samples as a function of energy. The peak located around 11564 eV corresponds to the Pt L_3 edge while the Au L_3 peak is located at 11919 eV on alloy samples. The Au edge is much higher relative

to the Pt edge on Au samples because the Pt loading is so low. Among alloy samples, the relative ratio of these peak heights are approximately constant.

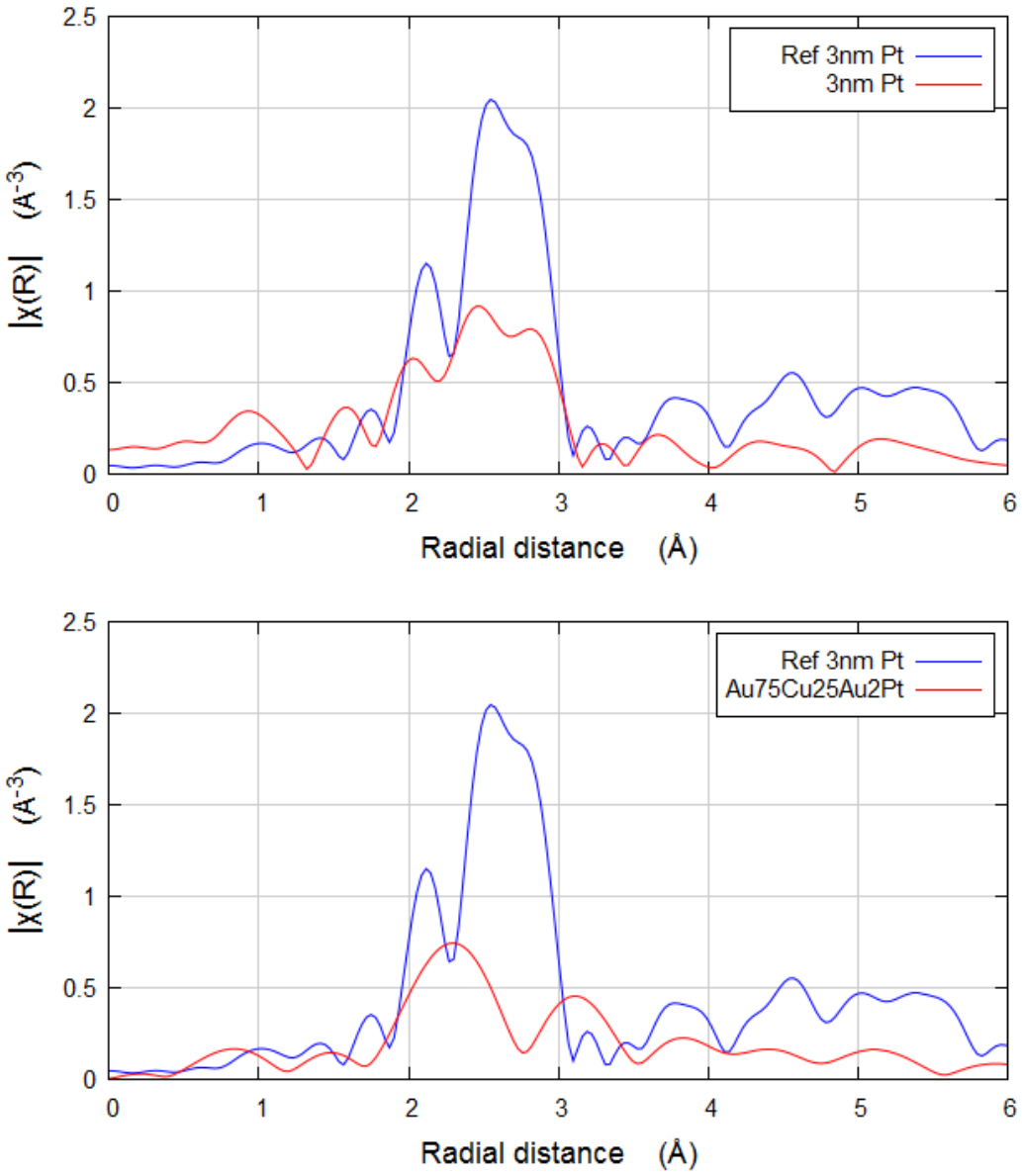

Figure 5.10. Processed XAS data comparing the EXAFS spectra for Pt/C, $Au_{75}Cu_{25}@Au_2@Pt/C$, and Pt reference foil.

Unfortunately, the proximity of the Pt and Au L_3 edges limits the range of energies that we can sample for Pt EXAFS analysis. Processed EXAFS for Pt foil and Pt/C spectra shown in Figure 5.10 show good agreement with other Pt standards reported in literature. Processed EXAFS spectra

from Pt monolayer alloys are very noisy and do not offer much insight into differences in local environment. Simulated EXAFS spectra on different Au@Pt and pure Pt surfaces show only geometric strain effects, which contribute to shifts in peak positions. Due to the similar chemical nature of Au and Pt atoms, ligand effects are not visible in EXAFS spectra.

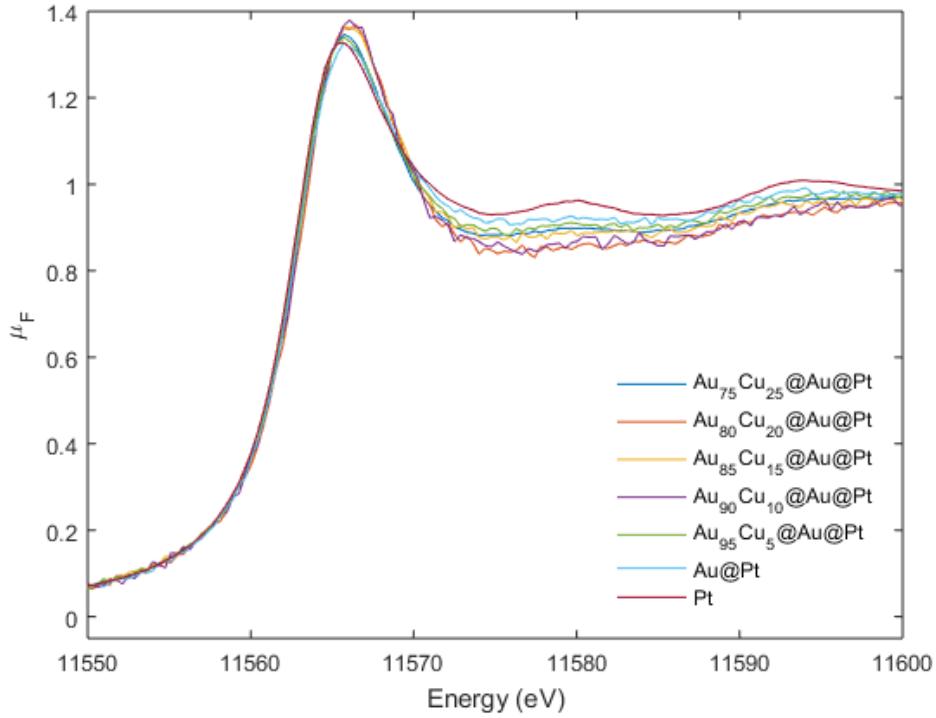

Figure 5.11. Normalized XANES spectra of ORR electrocatalysts.

Examination of the Pt L_3 XANES region shows that all Pt alloys have similar Pt edge spectra, with slight differences in peak position and shape relative to pure Pt. These deviations do not follow any particular trends with alloy composition, so it is not clear whether these observations are physically significant.

Projected density of states calculations were performed on various Pt monolayer electrocatalyst slabs to identify perturbations in the electronic structure of Pt surface atoms induced by ligand and lattice effects. Figure 5.12 shows the projected density of states for *s*, *p*, and *d* bands on Pt, Au@Pt, Pt@Au@Pt, and Pt@Au_2@Pt surfaces.

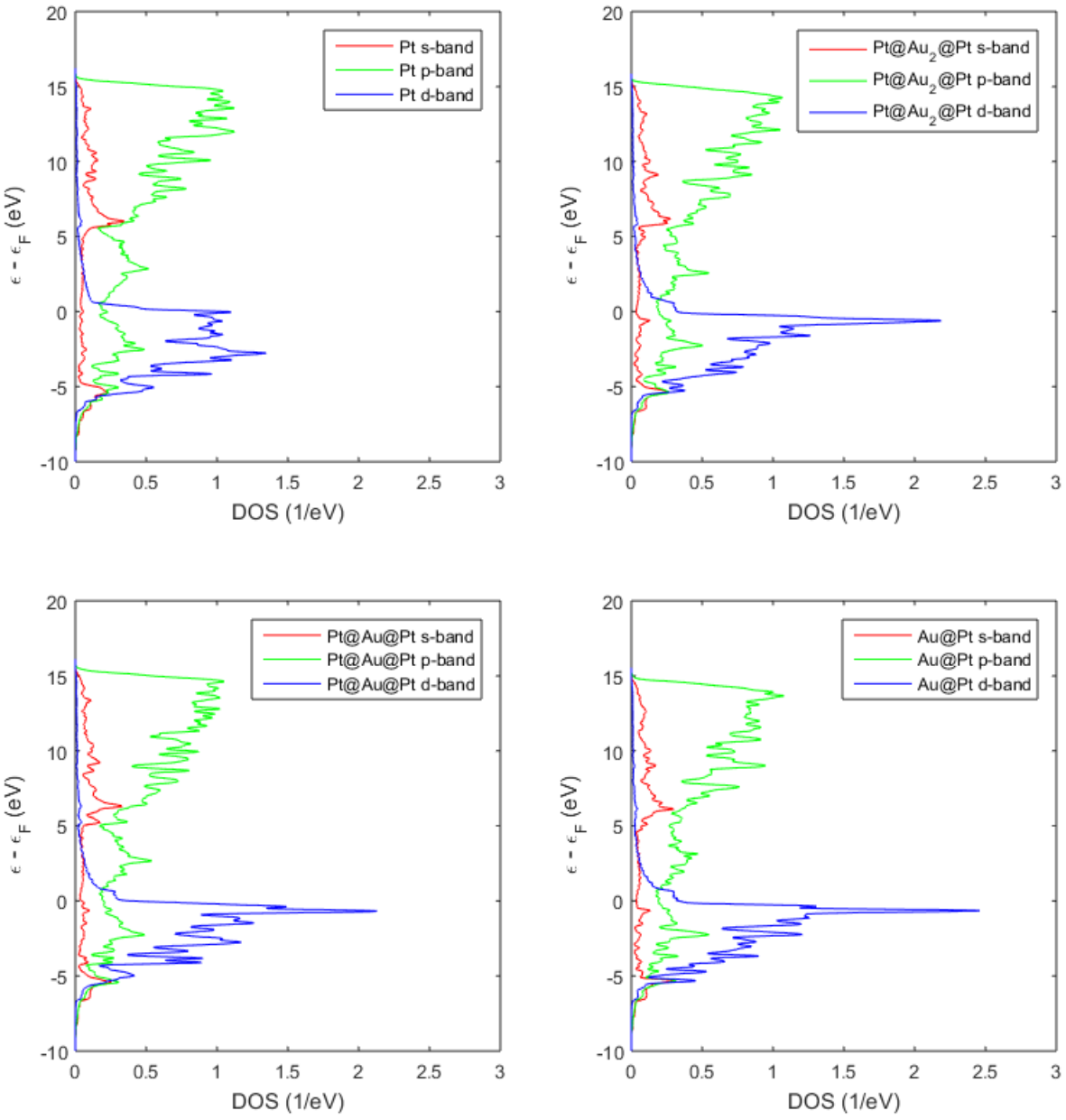

Figure 5.12. Localized density of states plots projected on Pt surface atoms of alloy surfaces.

The data in Figure 5.13 compares changes in *d*-band center and width resulting from ligand and strain effects on Pt monolayer slabs. In general, compressive lattice strain both lowers *d*-band centers and increases *d*-band widths. The similar chemical ligand effect present on Pt alloy surfaces leads to relatively higher *d*-band centers compared to pure Pt surfaces. Increasing Cu content

within the core also reduces the *d*-band width. This effect may explain why the XANES peak shape does not dramatically enlarge with further lattice compression.

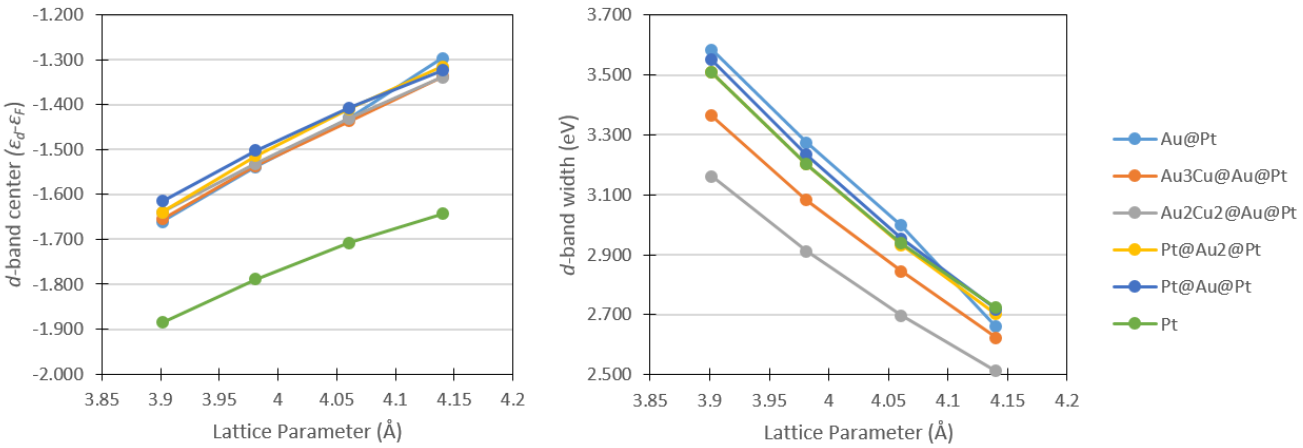

Figure 5.13. Changes in *d*-band structure on Pt alloy surfaces induced by alloying effects.

5.9. Conclusions

In this chapter, a family of ultra-low Pt loading alloy electrocatalysts were designed to improve ORR activity relative to pure Pt. The nanostructure of these materials enable selective manipulation of Pt surface atom reactivity through independently-controlled chemical ligand and lattice strain effects. Catalytic activity on these alloys was manipulated by changing the composition within the AuCu alloy core. The ORR activity of these materials showed the familiar volcano curve relationship to the composition of their nanoparticle cores, which impacts the OH binding energy. Extensive experimental testing and catalyst characterization validate our hypothesis that proposed activity trends result from perturbations in surface energetics induced by lattice strain effect.

5.10. References

1. Gasteiger, H. A. *et al.* Fuel Cell Basics. *Hydrog. energy* (2010).
2. Gasteiger, H. A., Kocha, S. S., Sompalli, B. & Wagner, F. T. Activity benchmarks and requirements for Pt, Pt-alloy, and non-Pt oxygen reduction catalysts for PEMFCs. *Applied Catalysis B: Environmental* **56,** 9–35 (2005).

3. Debe, M. K. Electrocatalyst approaches and challenges for automotive fuel cells. *Nature* **486,** 43–51 (2012).

4. *Multi-Year Research, Development and Demonstration Plan: Technical Plan - Fuel Cells*. (2012). at <http://www1.eere.energy.gov/hydrogenandfuelcells/mypp/pdfs/fuel_cells.pdf>

5. Xie, S. *et al.* Atomic Layer-by-Layer Deposition of Pt on Pd Nanocubes for Catalysts with Enhanced Activity and Durability toward Oxygen Reduction. *Nano Lett.* **14,** 3570–3576 (2014).

6. Zhang, L. *et al.* NANOCATALYSTS. Platinum-based nanocages with subnanometer-thick walls and well-defined, controllable facets. *Science* **349,** 412–6 (2015).

7. Nilekar, A. U. & Mavrikakis, M. Improved oxygen reduction reactivity of platinum monolayers on transition metal surfaces. *Surf. Sci.* **602,** L89–L94 (2008).

8. Park, J. *et al.* Atomic layer-by-layer deposition of platinum on palladium octahedra for enhanced catalysts toward the oxygen reduction reaction. *ACS Nano* **9,** 2635–47 (2015).

9. Chen, C. *et al.* Highly crystalline multimetallic nanoframes with three-dimensional electrocatalytic surfaces. *Science* **343,** 1339–43 (2014).

10. Adzic, R. R. *et al.* Platinum Monolayer Fuel Cell Electrocatalysts. *Top. Catal.* **46,** 249–262 (2007).

11. Gong, K., Su, D. & Adzic, R. R. Platinum-monolayer shell on AuNi(0.5)Fe nanoparticle core electrocatalyst with high activity and stability for the oxygen reduction reaction. *J. Am. Chem. Soc.* **132,** 14364–6 (2010).

12. Shao, M., Sasaki, K., Marinkovic, N., Zhang, L. & Adzic, R. Synthesis and characterization of platinum monolayer oxygen-reduction electrocatalysts with Co–Pd core–shell nanoparticle supports. *Electrochem. commun.* **9,** 2848–2853 (2007).

13. Nilekar, A. U. *et al.* Bimetallic and Ternary Alloys for Improved Oxygen Reduction Catalysis. *Top. Catal.* **46,** 276–284 (2007).

14. Xin, H. First-principles Modeling of the Surface Reactivity of Transition Metals with Perturbed Electronic Properties. (University of Michigan, 2011).

15. Kitchin, J. R., Nørskov, J. K., Barteau, M. A. & Chen, J. G. Modification of the surface electronic and chemical properties of Pt(111) by subsurface 3d transition metals. *J. Chem. Phys.* **120,** 10240 (2004).

16. Kitchin, J. R., Nørskov, J. K., Barteau, M. A. & Chen, J. G. Role of Strain and Ligand Effects in the Modification of the Electronic and Chemical Properties of Bimetallic Surfaces. *Phys. Rev. Lett.* **93,** 156801 (2004).

17. Xin, H., Holewinski, A. & Linic, S. Predictive Structure–Reactivity Models for Rapid Screening of Pt-Based Multimetallic Electrocatalysts for the Oxygen Reduction Reaction. *ACS Catal.* **2,** 12–16 (2012).

18. Xin, H., Holewinski, A., Schweitzer, N., Nikolla, E. & Linic, S. Electronic Structure Engineering in Heterogeneous Catalysis: Identifying Novel Alloy Catalysts Based on

Rapid Screening for Materials with Desired Electronic Properties. *Top. Catal.* **55,** 376–390 (2012).

19. Xin, H., Schweitzer, N., Nikolla, E. & Linic, S. Communications: Developing relationships between the local chemical reactivity of alloy catalysts and physical characteristics of constituent metal elements. *J. Chem. Phys.* **132,** 111101 (2010).

20. Xin, H. & Linic, S. Communications: Exceptions to the d-band model of chemisorption on metal surfaces: The dominant role of repulsion between adsorbate states and metal d-states. *J. Chem. Phys.* **132,** 221101 (2010).

21. Holewinski, A., Xin, H., Nikolla, E. & Linic, S. Identifying optimal active sites for heterogeneous catalysis by metal alloys based on molecular descriptors and electronic structure engineering. *Curr. Opin. Chem. Eng.* **2,** 312–319 (2013).

22. Sasaki, K. *et al.* Recent advances in platinum monolayer electrocatalysts for oxygen reduction reaction: Scale-up synthesis, structure and activity of Pt shells on Pd cores. *Electrochim. Acta* **55,** 2645–2652 (2010).

23. Zhang, J., Sasaki, K., Sutter, E. & Adzic, R. R. Stabilization of platinum oxygen-reduction electrocatalysts using gold clusters. *Science* **315,** 220–2 (2007).

24. Wang, J. X. *et al.* Oxygen reduction on well-defined core-shell nanocatalysts: particle size, facet, and Pt shell thickness effects. *J. Am. Chem. Soc.* **131,** 17298–302 (2009).

25. Stamenkovic, V. R., Mun, B. S., Mayrhofer, K. J. J., Ross, P. N. & Markovic, N. M. Effect of Surface Composition on Electronic Structure, Stability, and Electrocatalytic Properties of Pt-Transition Metal Alloys: Pt-Skin versus Pt-Skeleton Surfaces. *J. Am. Chem. Soc.* **128,** 8813–8819 (2006).

26. Huang, X. & El-Sayed, M. A. Gold nanoparticles: Optical properties and implementations in cancer diagnosis and photothermal therapy. *J. Adv. Res.* **1,** 13–28 (2010).

27. Motl, N. E., Ewusi-Annan, E., Sines, I. T., Jensen, L. & Schaak, R. E. Au−Cu Alloy Nanoparticles with Tunable Compositions and Plasmonic Properties: Experimental Determination of Composition and Correlation with Theory. *J. Phys. Chem. C* **114,** 19263–19269 (2010).

28. Holewinski, A. & Linic, S. Elementary Mechanisms in Electrocatalysis: Revisiting the ORR Tafel Slope. *J. Electrochem. Soc.* **159,** H864–H870 (2012).

29. Pedersen, C. M. *et al.* Benchmarking Pt-based electrocatalysts for low temperature fuel cell reactions with the rotating disk electrode: oxygen reduction and hydrogen oxidation in the presence of CO (review article). *Electrochim. Acta* (2015). doi:10.1016/j.electacta.2015.03.176

30. Garsany, Y., Singer, I. L. & Swider-Lyons, K. E. Impact of film drying procedures on RDE characterization of Pt/VC electrocatalysts. *J. Electroanal. Chem.* **662,** 396–406 (2011).

31. Garsany, Y., Baturina, O. A., Swider-Lyons, K. E. & Kocha, S. S. Experimental methods for quantifying the activity of platinum electrocatalysts for the oxygen reduction reaction.

Anal. Chem. **82,** 6321–8 (2010).

32. van der Vliet, D. F. *et al.* Unique electrochemical adsorption properties of Pt-skin surfaces. *Angew. Chem. Int. Ed. Engl.* **51,** 3139–42 (2012).

33. Bandarenka, A. S. *et al.* Design of an active site towards optimal electrocatalysis: overlayers, surface alloys and near-surface alloys of Cu/Pt(111). *Angew. Chem. Int. Ed. Engl.* **51,** 11845–8 (2012).

34. Schweitzer, N., Xin, H., Nikolla, E., Miller, J. T. & Linic, S. Establishing Relationships Between the Geometric Structure and Chemical Reactivity of Alloy Catalysts Based on Their Measured Electronic Structure. *Top. Catal.* **53,** 348–356 (2010).

Chapter 6

Electrochemical oxygen reduction reaction on Ag nanoparticles of different shapes

6.1. Summary

Silver electro-catalysts are an attractive alternative to platinum for electrochemical oxygen reduction reaction in alkaline fuel cells. Recent advances in the synthesis of metal nanoparticles have enabled the design of silver nanoparticles of different shapes, terminated with different surface facets which exhibit different catalytic properties. In this contribution, we prepared spherical and cubic silver nanoparticle electro-catalysts and tested their electro-catalytic oxygen reduction reaction activity in 0.1M sodium hydroxide. Our work demonstrates that carbon-supported silver nanospheres and nanocubes of similar size exhibit similar ORR activity with the spheres slightly outperforming the cubes. We describe our findings below and suggest possible reasons for the slightly enhanced activity of the nanospheres.

6.2. Introduction

Catalyzing the electro-chemical oxygen reduction reaction (ORR) is critical for the design of highly efficient fuel cells. While platinum has been the principal material of interest because of its high catalytic activity and superior stability – Pt and Au are the only stable metals under the conditions of electro-catalytic ORR in acidic electrolytes – the practical implementation of Pt-based electrodes has been hampered by their high cost.[1,2] While the superior electro-catalytic ORR activity of Pt compared to other metals persists in basic medium (with OH^- as the charge carrier), the number of materials that are stable under these conditions is significantly larger than in acid.[3,4]

For example, silver (Ag) leaches in the form of oxidized Ag ions in acid under ORR conditions. On the other hand, Ag forms a stable oxide near ORR conditions in basic medium as shown in Figure 6.1. Ag is also currently approximately seventy times less expensive than Pt.[5] The main problem with Ag electro-catalysts is that in base these materials are at least an order of magnitude less active on a per surface site basis toward ORR than platinum.[6,7]

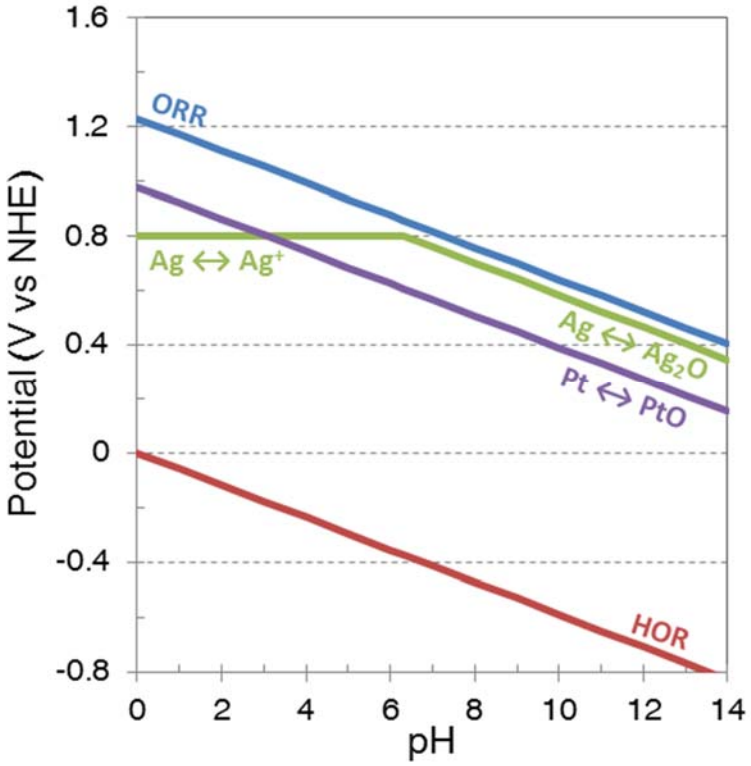

Figure 6.1. The Pourbaix diagram shows the equilibrium potentials for silver and platinum oxidization reactions as a function of the solution pH and potential with respect to the normal hydrogen electrode potential scale. At high potentials, oxidized species are favored making electrode stability a major concern in acidic electrolytes. Operating in alkaline conditions enables the use of more materials including silver as ORR catalysts.

Recent work in our group has demonstrated that Ag-Co alloy nanoparticle electro-catalysts perform ORR in basic medium at a rate that is more than 5 times higher than the rate on pure Ag nanoparticles of identical size.[8] These materials were identified based on an analysis of the ORR reaction mechanism on the Ag(111) surface at the elementary step level.[6–9] This mechanistic

analysis suggested that by perturbing the Ag surface atoms in such a way that they bind oxygenated surface intermediates slightly more strongly than the Ag(111) surface yields a more reactive Ag surface.[9–11] Our studies suggested that the electronic communication between subsurface Co atoms and the surface Ag atoms in the alloy nanoparticles electronically perturbs the Ag surface atoms yielding more reactive ORR materials.[8]

One way to accomplish the objective of creating Ag surface sites that bind oxygenated intermediates more strongly than the Ag(111) surface is, as mentioned above, to create suitable Ag alloys.[8,12,13] An alternative approach is to control the distribution of surface facets exposed to the reactants and intermediates involved in ORR by controlling the morphology of Ag nanoparticles.[14–20] For example, the Ag(100) surface binds oxygenated adsorbates more strongly that the Ag(111) surface.[21,22] Since Ag nanocubes have a significantly larger concentration of the Ag(100) surface sites compared to the Ag nanospheres, we hypothesize that Ag nanocubes should be more reactive than nanospheres. In this contribution we have used colloidal synthetic routes to synthesize Ag nanoparticles of cubic and spherical shapes. We tested these nanostructures in electrochemical ORR in a basic environment. Contrary to our original hypothesis, we found that samples containing Ag spheres and Ag cubes exhibit similar performance with the Ag spheres slightly outperforming the cubes of equal size. We describe our findings below and suggest possible reasons for the superior activity of the nanospheres.

6.3. Experimental Details

6.3.1. Electro-catalyst synthesis

Silver nanospheres were synthesized following a previously established procedure.[19,23] In general, 10mL of ethylene glycol (JT Baker) was added to a vial and heated for 45-60 minutes at 160°C in a silicone oil bath. Then, 3mL solutions of 600mM polyvinylpyrrolidone (PVP from

Sigma-Aldrich; M_w=55,000) and 100mM $AgNO_3$ (Sigma-Aldrich) in ethylene glycol were prepared and dropwise added to the heated vial. The vial was capped and after roughly 1 hour removed from the oil bath and quenched with cool water.

Silver cubes were synthesized by a method developed by Xia.[24] Briefly, 5mL of ethylene glycol was heated to 140 - 150°C. After 45 minutes, 80μL of 30mM Na_2S solution was added to ethylene glycol. A few minutes later, 0.5 mL of 0.28 M $AgNO_3$ and 1.5mL of 0.18 M PVP solutions were quickly added to the vial. The vial was capped and the solution was allowed to react for roughly 45 minutes after which it was removed from the oil bath to inhibit the further nanoparticle growth.

The solutions containing Ag nanoparticles were washed four times with acetone to remove capping agents, solvent, and unreacted reagents. After each washing procedure, Ag nanoparticles were collected by centrifugation at 7000 rpm for 20 minutes. The effluent was discarded and Ag nanoparticle suspensions were reconstituted in a small volume (2 – 5 mL) of ethanol prior to the next acetone wash. After the final centrifugation, Ag nanoparticles were re-suspended in pure ethanol and deposited onto Vulcan XC72 powder (Cabot, pretreated for at least 2 hours in H_2 at 400°C). The catalyst solutions were dried overnight in a heating oven.

6.3.2. Electro-catalyst characterization

UV-visible extinction spectroscopy (UV-vis) experiments were performed using a Thermo Scientific Evolution 300 UV-Vis spectrophotometer with a Xenon lamp source to measure the extinction spectra of dilute Ag nanoparticle suspensions. UV-vis spectra were collected between wavelengths of 300 and 800 nm at a rate of 600 nm min^{-1} and were normalized by the peak signal intensity to facilitate comparison of samples with different concentrations. Scanning electron

microscopy (SEM) was performed on Ag nanoparticles deposited directly on a clean Si chip (≈ 1cm^2; rinsed with piranha solution and dried) using a FEI NOVA Nanolab operating in secondary electron detection mode. Micrographs were obtained using a TLD (through-the-lens detector) and the accelerating voltage was 15kV. Surface-enhanced Raman spectroscopy (SERS) experiments were measured on Ag nanoparticle on Si substrate using a Horiba Jobin-Yvon LabRAM HR system. SERS spectra were acquired over 300 - 2000cm^{-1} range using a 532 nm laser with 5s acquisition time and by averaging the signal over 10 consecutive acquisitions. X-ray photoelectron spectroscopy (XPS) experiments were performed on Ag nanoparticle catalysts on Vulcan XC72 support using a Kratos Axis Ultra XPS with monochromatic Al K_α (1486.69eV) X-ray source. As-prepared Ag/C samples were heated overnight in an UHV system to remove residual moisture before being directly transferred to a vacuum chamber (pressure of ≈ 10^{-9} torr) for analysis. XPS spectra were measured at every 0.1 eV over the ranges of 158-172 eV, 277-300 eV, and 355-385 eV to observe S 2p, C 1s, and Ag 3d peaks. XPS signals were normalized by their acquisition times (10.6, 6.5, and 7.5 s, for S, C, and Ag peaks, respectively). Charging effects were compensated using a flood gun. XPS binding energies were calibrated based on positioning the main C 1s peak at 284.8 eV, which originates from the carbon support.

6.3.3. Electrochemical measurements

Electrochemical measurements were performed at room temperature in a custom built Teflon three-electrode cell with a Gamry Instruments Reference 3000 potentiostat/galvanostat/Frequency-Response-Analyzer. The reference (Hg/HgO in 1 M KOH, Radiometer Analytical) and counter electrodes (Pt wire, Alfa Aesar) were both in isolated compartments with long diffusion paths to the working electrode chamber. Working electrodes were prepared by sonicating the catalyst powders in 99.9% acetone (Fisher) at 1.50 mg mL^{-1} for

more than an hour and dispersing 18 μL onto a 5 mm glassy carbon disc electrode insert (Pine Instruments). These electrodes were placed into a Teflon rotating disc electrode (RDE) housing, which was attached to a rotator (Pine Instruments).

Electrolyte solutions of 0.1 M NaOH were prepared from ultrapure water (18.2 MΩ cm (Millipore)) and 99.99% sodium hydroxide (Alfa Aesar). The reaction rates were measured in the O_2-saturated electrolyte using linear sweep voltammetry at rotation rates between 400-2500 rpm at a scan rate of 10mV/s to achieve steady state rates. A consistent uncompensated resistance of ≈ 40 Ω was measured via high-frequency impedance, and was corrected for in the polarization curves. All potentials are reported relative to the RHE ($V_{RHE} = V_{NHE} + 0.0591$ pH (NHE, normal hydrogen electrode)), calibrated by the H_2 oxidation equilibrium. Electrochemical surface areas (ESCA) of Ag electro-catalysts were measured by Pb underpotential deposition immediately following the rate measurements. In these measurements PbNO3 was added to make 125μM Pb^{2+} in 0.1M NaOH and the cell was deaerated by bubbling Ar for 15-20 minutes. The electrode was repeatedly held at 0.20 V_{RHE} and swept to 0.6 V_{RHE} at 20 mV s^{-1}. The stable voltammograms were integrated assuming 280 μC cm^{-2} Ag.[25]

6.4. Results and Discussion

6.4.1. Characterization of Ag Nanoparticles

The data in Figure 6.2 show the UV-vis extinction spectra of various samples of Ag spheres and cubes prior to their deposition onto Vulcan XC72R carbon. The extinction in the UV-vis spectra is the consequence of the excitation of localized surface plasmon resonance (LSPR) in Ag nanostructures. The wavelength and shape of the LSPR extinction peaks are characteristics of the shape and size of Ag nanoparticles.[24,26] The appearance of the single peak in the Ag UV-vis extinction spectra at around 400 nm is a characteristic of Ag spheres with ≈ 40 nm diameters, while

the triple extinction peak is a distinguishing feature of nanoscopic Ag cubes.[24,26] The UV-vis extinction spectra are consistent with relatively pure samples of Ag cubes and spheres. Following the four acetone washes, the UV-vis extinction spectra showed no changes compared to the original UV-vis spectra, suggesting minimal changes in particle morphology. The size and shape of Ag samples were also verified by SEM of nanoparticles deposited onto a Silicon substrate, shown in Figure 6.2. Analysis of these micrographs showed that Ag spheres had an average diameter of 43.7 ± 8.5 nm while cubes had an average edge length of 40.8 ± 5.4 nm.

Since we used colloidal synthesis methods that employ organic stabilizing agents (mainly PVP), we attempted to remove these molecules before performing electrochemical tests. The removal of PVP was attempted by washing the sample in acetone multiple times as described above. Data in Figure 6.2 d and e show surface enhanced Raman spectra (SERS) of our Ag samples after the first and fourth washing step. The analysis of the SERS spectra suggests that there is a significant decrease in the PVP signal due to the washing process. We note that the Raman peaks around 1400-1600 cm^{-1} correspond to the C-C stretches of PVP.[27] The data also show that there is some residual PVP that was detected on Ag even after multiple washing steps; however, when comparing to the as-prepared samples and considering that these Ag nanostructures are excellent in enhancing Raman signal, the amount of residual PVP appears to be relatively small.

Data in Figure 6.3 show XPS spectra of the Ag nanosphere and nanocube samples on carbon and the Ag-free carbon support. In this XPS analysis, among other elements, we focused on sulfur since it has been shown to affect the chemical activity of metals and it was used in the synthesis of the Ag cubes.[24,28,29] The Sulfur 2p XPS spectrum shows that sulfur is present in all the samples in the similar concentrations and chemical states suggesting that the main source of sulfur

is the carbon support. Data in Figure 6.3 also show the Ag 3d XPS spectra. It is found that Ag is present in the metallic form.

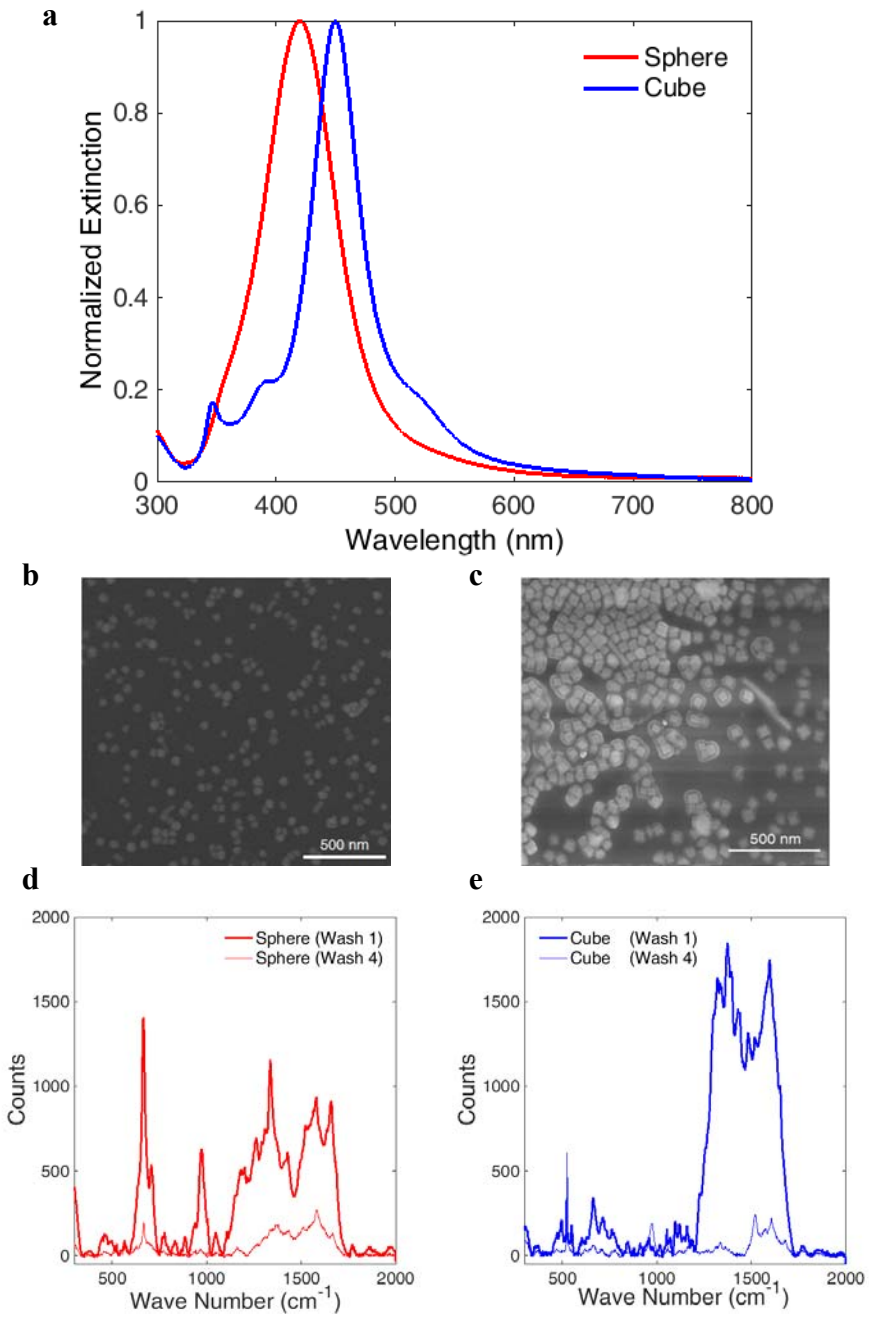

Figure 6.2. Extinction spectra (a) of representative Ag sphere and cube samples that were tested in our electrochemical experiments. SEM images of silver nanospheres (b) and nanocubes (c) particles deposited on Si substrate. SERS spectra Ag nanospheres (d) and Ag nanocubes (e) following multiple acetone rinses.

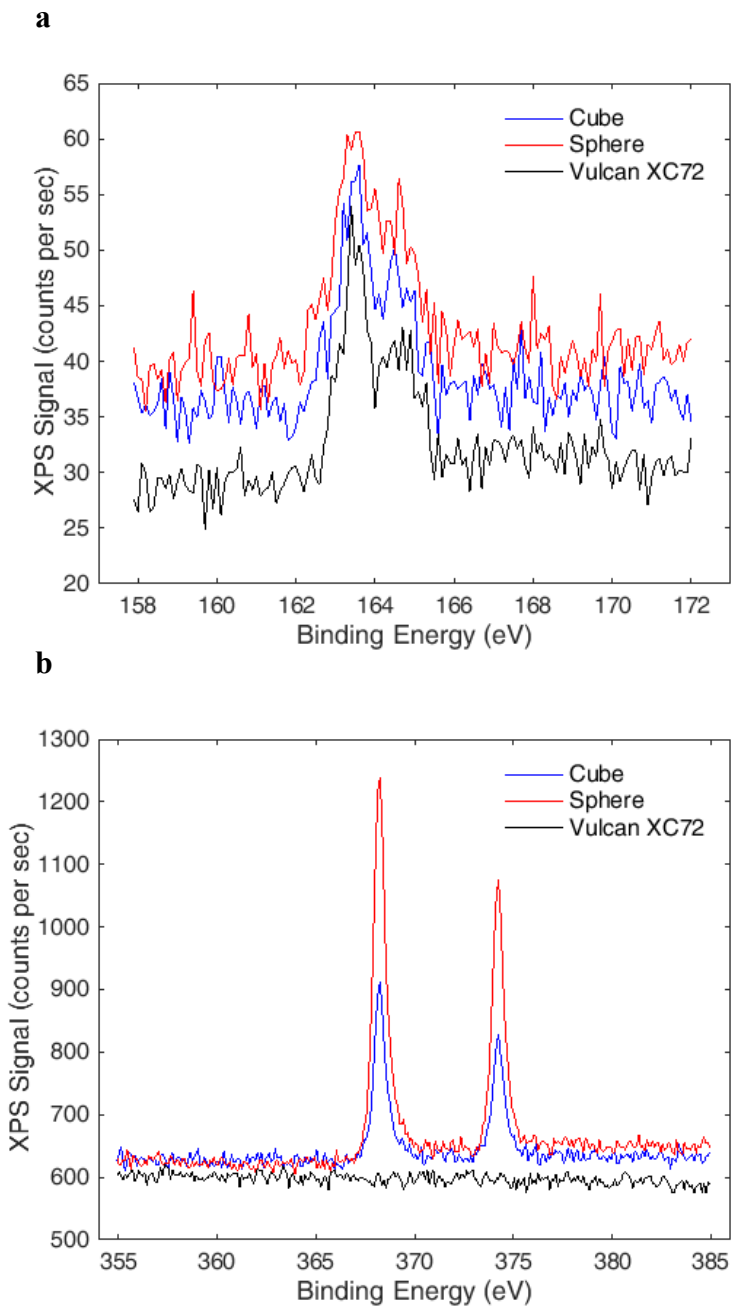

Figure 6.3. XPS spectra for S 2p (a) and Ag 3d (b) core states measured for various Ag nanoparticle catalysts and carbon support.

6.4.2. *Electrochemical Performance*

Linear sweep voltammetry experiments were performed on supported Ag nanoparticles (Ag/Vulcan XC72) in the thin film rotating disk electrode configuration to measure their oxygen

reduction rate as a function of potential and rotation rate. The data in Figure 6.4 show the polarization behavior for representative Ag sphere and cube nanoparticle electro-catalysts. The polarization curves in Figure 6.4 were obtained by adjusting the kinetic current to an equal surface area basis (with a roughness factor of 1) as described in Ref 8. This was accomplished by first computing the raw kinetic current using Koutecky-Levich equation: |ik(V)| = (1/|i(V)| -1/|iL|)-1, where i is the raw measured current, i_k is the raw kinetic current, and i_L is the limiting current measured between 0.2 and 0.5 V_{RHE}. The raw kinetic current was then normalized to the electrochemical surface area (ESCA). We describe further below how ESCA was measured. The normalized kinetic current density ($j_k = |i_k|/ECSA$) was then used to regenerate the RDE current density (j) curves on a superficial area basis as: $|j| = \left(\frac{1}{j_k} + \frac{A_{disk}}{|i_L|}\right)^{-1}$.

At high potentials, ORR is limited by the intrinsic activity of the electro-catalysts and their loading, showing an exponential dependence of current on applied potential. At low potentials, the overall rate becomes limited by the transport of O_2 to the surface which is a function of the RDE rotation rate. The kinetic rate of ORR can be determined by accounting for the effects of O_2 transport to the electrode on the observed rate (current) as described in the Koutecky-Levich equation. The data in Levich plot (inset) shows the mass-transfer limiting current density as a function of rotation rate. The slope of this line indicates that ORR proceeds through the 4 e^- pathway with very high selectivity to H_2O for both electrocatalysts.

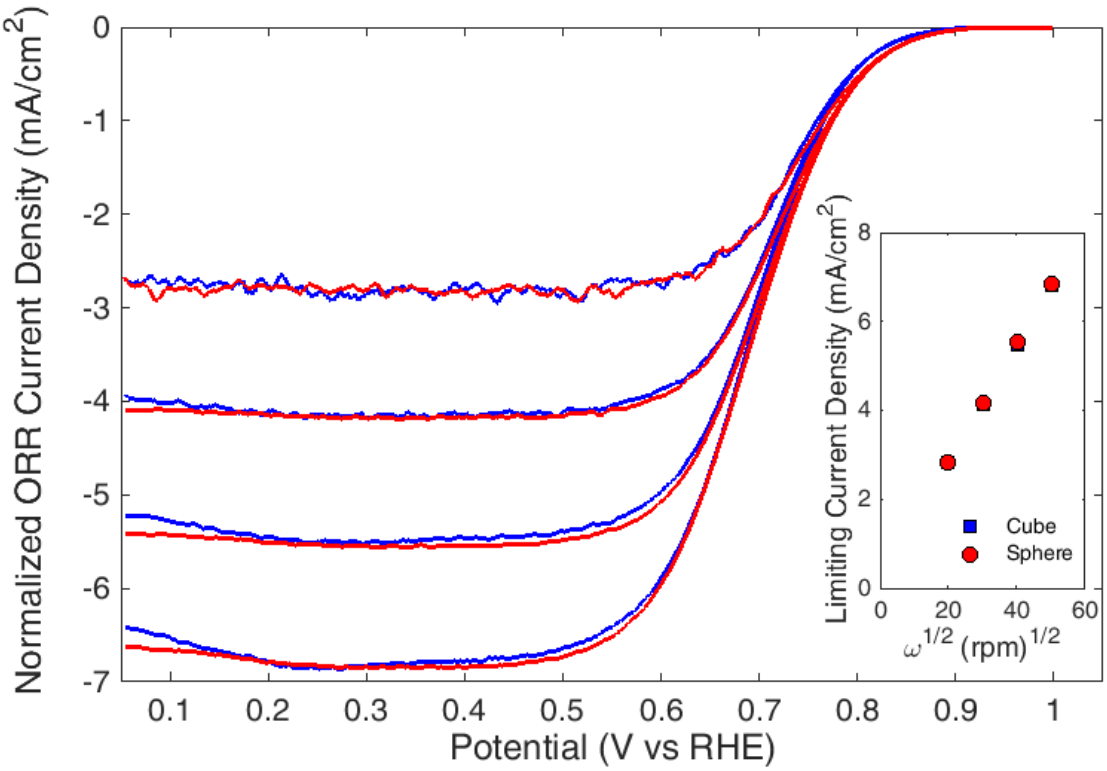

Figure 6.4. ORR current densities were measured for Ag nanospheres (red) and nanocubes (blue) as a function of potential (V vs RHE) at rotation rates of 400, 900, 1600, and 2500 rpm. Both particle morphologies exhibited nearly equivalent mass-transfer limiting current densities and similar selectivity towards complete O_2 reduction to water. The slope of the Levich plot (inset) is consistent with a $4e^-$ transfer mechanism.

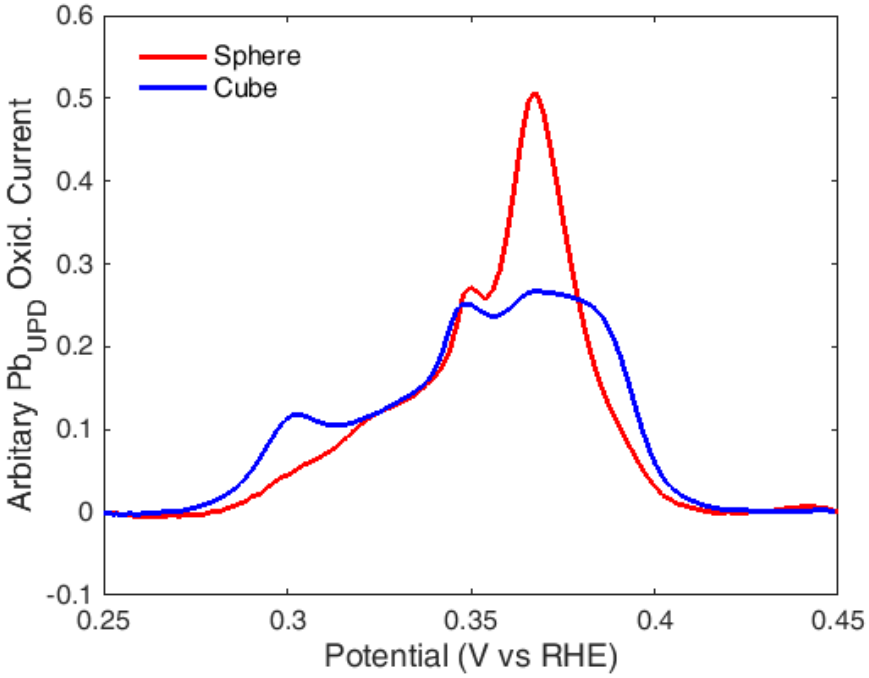

Figure 6.5. The background-corrected Pb UPD oxidization curves for silver nanocubes (blue) and nanospheres (red) in 0.1M NaOH show different features over the potential range of 0.25 - 0.45 V.

To compare the relative kinetic performance of different electro-catalysts, the rate of oxygen reduction reaction was normalized by the number of electro-catalytic sites, or electrochemical surface area (ECSA). This required a rigorous measurement of electrochemical surface area, i.e., the area at the reactive interface between the liquid electrolyte and metal electrode. The ECSA of Ag electro-catalysts was measured by utilizing the phenomenon of Pb underpotential deposition onto Ag. Previous work has shown that by holding an Ag electrode slightly above the $Pb^{2+/}Pb$ reduction potential, a submonolayer (≈ 2/3 monolayers) of Pb deposits onto the Ag surface.[25,30,31] By scanning to higher potentials, the underpotentially deposited Pb submonolayer is dissolved, generating an oxidative current. By measuring the oxidative current, it is possible to directly measure the Ag ECSA by integrating the Pb_{UPD} oxidization peak. The data in Figure 6.5 show the oxidative currents generated during the oxidation of Pb sub monolayers

on the surface of representative Ag cube and sphere electro-catalyst. To generate the plots of the oxidative current in Figure 6.6, the background due to capacitive charging of the carbon support was removed. We note that at the potential range where the oxidation and desorption of Pb from Ag surfaces takes place (0.25 - 0.45 V vs RHE) there were no other electrochemical processes and therefore no further background corrections were required. Multiple peaks in the oxidative current curves are associated with the Pb oxidation and desorption from the different surface facets of Ag. The multiple peaks allow us to quantify the contribution of different Ag surface facets to the electrochemical surface area. We will revisit this issue further below.

The data in Figure 6.6 show the net kinetic currents (not normalized by the ESCA) for different samples of Ag nanoparticle electro-catalysts plotted against their electrochemical surface area at two different operating potentials (0.80 and 0.85V vs RHE). We note that unlike for Pt electrodes, where it is customary to report currents at 0.9 V vs RHE, Ag-based electrodes exhibit lower ORR activity and the currents are usually reported at 0.85 and 0.80 V. The kinetic current was obtained as described above using Koutecky-Levich equation. The data shows that oxygen reduction rate over this range of metal nanoparticle loadings scales linearly with the electrochemical surface area. This linear scaling suggests that the electrode design allows for a rigorous deconvolution and measurements of kinetic currents, which is critical if different electro-catalysts are to be compared using the RDE setup.

The slope of the lines in Figure 6.6 corresponds to the average specific activity (the ORR rate per electrochemical surface area) of the nanoparticles over this range of surface areas. By comparing these slopes at various potentials, it is possible to compare the performance of different Ag nanoparticle electro-catalysts. From the specific activities calculated for these silver

nanoparticle samples, we observe that spheres are approximately 12 ± 8% and 18 ± 10% more active than cubes at 0.80 and 0.85 V on the reversible hydrogen electrode potential scale.

Data in Figure 6.6 show relatively small differences in ORR activity between Ag nanospheres and nanocubes. One plausible explanation is that nanoparticles undergo morphological changes in the electrochemical environment leading to similar surface structures and therefore similar activities. To address this possibility we performed in situ electrochemical adsorption/desorption measurements to investigate potential electro-catalyst restructuring during the course of the measurement. While cyclic voltammetry measurements on Ag nanoparticles in deaerated electrolyte did not yield any significant electro-chemical adsorption features, both Ag structures exhibited distinct Pb_{UPD} stripping features, characteristic of the presence and persistence of different Ag surface facets.

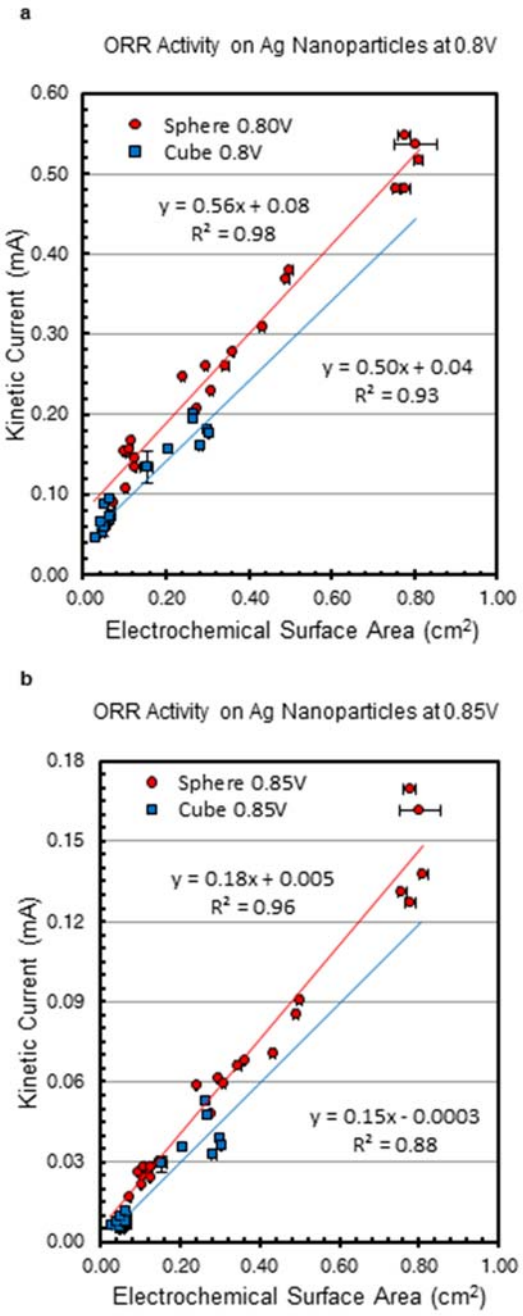

Figure 6.6. Alkaline ORR kinetic currents of supported silver nanosphere (red) and nanocube (blue) electro-catalysts with different weight loadings at two different operating potentials: 0.80 V (top) and 0.85 V (bottom). The measured kinetic currents were shown to scale linearly with electrochemical surface area suggested the specific current density (mA/cm^2 ECSA) was constant for samples over this range of loadings. A direct comparison of the average specific activity shows spheres are more active than cubes at 0.80 and 0.85 V vs RHE with Ag(100) surface facets covering roughly 40 – 45 % of the surface.

The data in Figure 6.5 show the Pb_{UPD} oxidative stripping spectra for the two Ag nanoparticle samples as a function of electrochemical potential measured after a set of electro-chemical measurements were performed on the samples. The Pb stripping spectra show that the Ag surfaces in the two electro-catalysts are different from each other. Previous measurements on well-defined Ag(111) and Ag(100) single crystal surfaces allow us to assign the stripping features to a particular Ag surface facet.[25,30,31] It has been demonstrated that the Ag(111) surface exhibits two sharp peaks located at +130 and +155 mV relative to Pb/Pb^{2+} reduction potential (corresponding to 0.34 and 0.37 V_{RHE}), while the Ag(100) surface exhibits three peaks: a short broad feature located at +50mV [0.26V_{RHE}], a sharp peak located at +100mV (0.31V_{RHE}), and a broad peak located around +135mV (0.36V_{RHE}) as shown in Figure 6.7. [25,30,31]

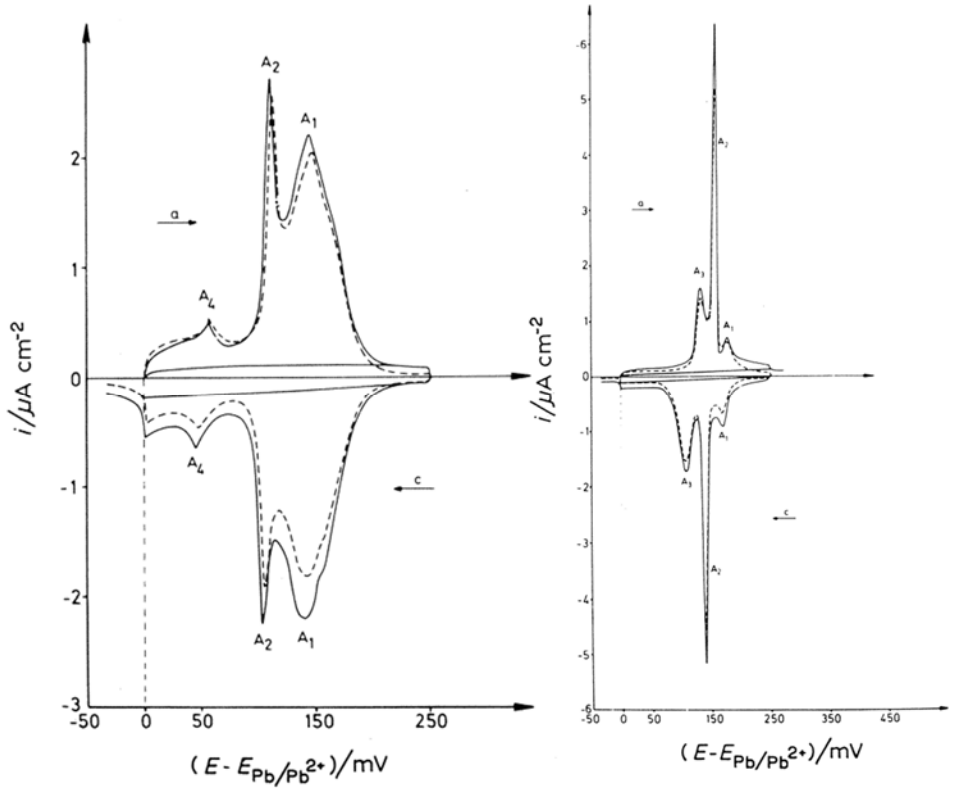

Figure 6.7. Pb UPD spectra measured for Ag (100) (left) and (111) (right) electrodes in measured perchloric acid at 0.42 mV/s.[25]

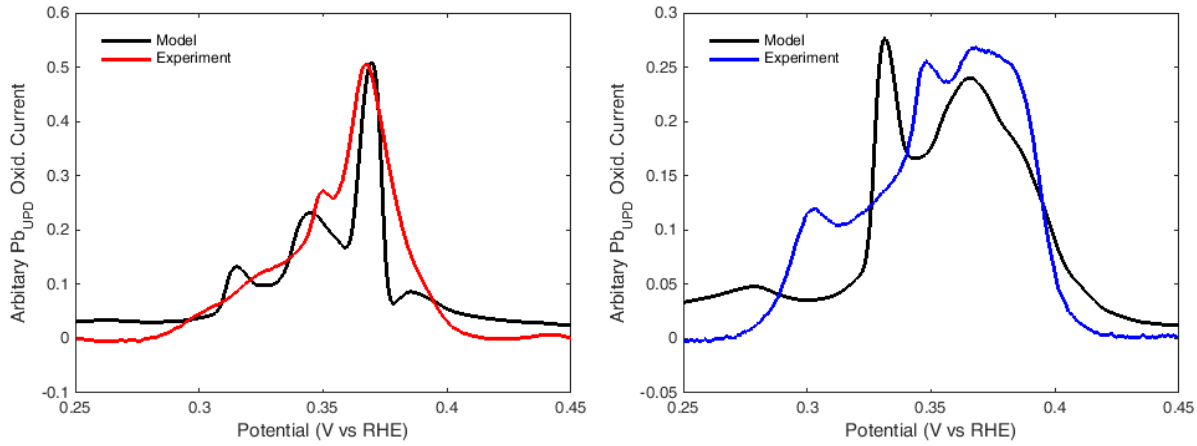

Figure 6.8. Comparison of experimental and fitted Pb stripping spectra for supported Ag nanosphere (left) and nanocube (right) samples.

Utilizing the Pb_{UPD} stripping spectra, it is possible to estimate the relative abundance of the Ag(111) and Ag(100) sites on Ag cubes and spheres. To accomplish this, we de-convoluted the measured Pb stripping spectra in terms of the linear combination of the previously reported and discussed Ag(111) and Ag(100) Pb spectra.[25] The concentration of various surface facets on our nanostructures was determined by minimizing the sum of square errors between the de-convoluted and experimental spectra. Not surprisingly, we found that Ag nanocube samples exhibit largely (100) character (≈ 80 – 95 %) while Ag spheres contained significant fractions of both surfaces. Figure 6.8 directly compares experimentally measured Pb stripping spectra on different Ag nanoparticle samples with their best fits. Data from Pb UPD experiments on Ag single crystals were used to generate curves representative of a silver surface with a mixture of (100) and (111) sites. The single crystal experiments were performed at slower voltage scan rate and in non-interacting perchloric acid unlike our experiments on supported Ag nanoparticles, which were performed at 20 mV/s in 0.1 M NaOH. The slight differences between model and experimental data likely result from the different testing conditions.

The observation that the Ag spheres are more active that Ag cubes is in contradiction with our proposed hypothesis that Ag surfaces which bind oxygenated intermediates slightly more strongly than the clean Ag(111) should exhibit higher ORR activity than Ag(111). We postulate that the reason for this contradiction is that the Ag(100) surface binds oxygenated intermediates, such as OH*, too strongly and that under relevant high potential ORR conditions these sites are poisoned by these intermediates. This is supported by DFT calculations which showed that Ag(100) binds OH stronger than Ag(111) by ≈ 0.5 eV, suggesting that Ag(100) is more likely to be poisoned at high potentials and therefore less catalytically active than the Ag(111) surface.[21,32] We also note that Blizanac and coworkers demonstrated using single crystal Ag(111) and Ag(100) electrodes that Ag(111) was ≈ 33 and 50% more active compared to Ag(100) at 0.80 and 0.85V w.r.t. RHE respectively for ORR performed in 0.1M KOH.[6] If we assume cubes are entirely terminated by Ag(100) sites and spheres have 45% Ag(100) and 55% Ag(111) surface coverage, using these previously reported ORR rate numbers we compute that the spheres are expected to be more active than cubes by ≈ 18 – 27 % at potentials between 0.80 and 0.85 V_{RHE}, which is relatively consistent with our findings.[6] This work suggests the intrinsic ORR activity of Ag nanostructures cannot be improved by replacing Ag(111) with Ag(100) surface sites.

6.5. Conclusion

In summary, we have demonstrated that carbon-supported 40nm Ag spheres are slightly more catalytically active towards alkaline ORR than carbon-supported 40nm Ag cubes. Ex-situ and electrochemical characterization have shown that Ag nanoparticles maintain their distinct morphologies throughout catalyst preparation and testing. We observed the relative ORR activity enhancement of Ag spheres compared to Ag cubes is consistent with the abundance of (111) and (100) surface facets and their relative activities.

6.6. References

1. Gasteiger, H. A., Kocha, S. S., Sompalli, B. & Wagner, F. T. Activity benchmarks and requirements for Pt, Pt-alloy, and non-Pt oxygen reduction catalysts for PEMFCs. *Applied Catalysis B: Environmental* **56,** 9–35 (2005).

2. Stephens, I. E. L., Bondarenko, A. S., Grønbjerg, U., Rossmeisl, J. & Chorkendorff, I. Understanding the electrocatalysis of oxygen reduction on platinum and its alloys. *Energy Environ. Sci.* **5,** 6744 (2012).

3. Gasteiger, H. A. & Ross, P. N. Oxygen Reduction on Platinum Low-Index Single-Crystal Surfaces in Alkaline Solution: Rotating Ring Disk Pt(hkl) Studies. *J. Phys. Chem.* **100,** 6715–6721 (1996).

4. Schmidt, T. J., Stamenkovic, V., Ross, Jr., P. N. & Markovic, N. M. Temperature dependent surface electrochemistry on Pt single crystals in alkaline electrolyte. *Phys. Chem. Chem. Phys.* **5,** 400–406 (2003).

5. Mineral Commodity Summaries 2015. at <http://minerals.usgs.gov/minerals/pubs/mcs/2015/mcs2015.pdf>

6. Blizanac, B. B., Ross, P. N. & Marković, N. M. Oxygen reduction on silver low-index single-crystal surfaces in alkaline solution: rotating ring disk(Ag(hkl)) studies. *J. Phys. Chem. B* **110,** 4735–41 (2006).

7. Wiberg, G. K. H., Mayrhofer, K. J. J. & Arenz, M. Investigation of the Oxygen Reduction Activity on Silver - A Rotating Disc Electrode Study. *Fuel Cells* **10,** 575–581 (2010).

8. Holewinski, A., Idrobo, J.-C. & Linic, S. High-performance Ag-Co alloy catalysts for electrochemical oxygen reduction. *Nat. Chem.* **6,** 828–34 (2014).

9. Holewinski, A. & Linic, S. Elementary Mechanisms in Electrocatalysis: Revisiting the ORR Tafel Slope. *J. Electrochem. Soc.* **159,** H864–H870 (2012).

10. Xin, H., Holewinski, A. & Linic, S. Predictive Structure–Reactivity Models for Rapid Screening of Pt-Based Multimetallic Electrocatalysts for the Oxygen Reduction Reaction. *ACS Catal.* **2,** 12–16 (2012).

11. Xin, H., Holewinski, A., Schweitzer, N., Nikolla, E. & Linic, S. Electronic Structure Engineering in Heterogeneous Catalysis: Identifying Novel Alloy Catalysts Based on Rapid Screening for Materials with Desired Electronic Properties. *Top. Catal.* **55,** 376–390 (2012).

12. Lu, Y., Zhang, N., An, L., Li, X. & Xia, D. Synthesis of high dispersed intermetallic Ag4Sn/C and its enhanced oxygen reduction reaction activity. *J. Power Sources* **240,** 606–611 (2013).

13. Jin, Y., Chen, F., Lei, Y. & Wu, X. A Silver-Copper Alloy as an Oxygen Reduction Electrocatalyst for an Advanced Zinc-Air Battery. *ChemCatChem* **7,** 2377–2383 (2015).

14. Lee, C.-L., Chiou, H.-P., Syu, C.-M. & Wu, C.-C. Silver triangular nanoplates as

electrocatalyst for oxygen reduction reaction. *Electrochem. commun.* **12,** 1609–1613 (2010).

15. Ohyama, J. *et al.* Oxygen reduction reaction over silver particles with various morphologies and surface chemical states. *J. Power Sources* **245,** 998–1004 (2014).

16. Wang, Q. *et al.* Shape-dependent catalytic activity of oxygen reduction reaction (ORR) on silver nanodecahedra and nanocubes. *J. Power Sources* **269,** 152–157 (2014).

17. Lu, Y., Wang, Y. & Chen, W. Silver nanorods for oxygen reduction: Strong effects of protecting ligand on the electrocatalytic activity. *J. Power Sources* **196,** 3033–3038 (2011).

18. Christopher, P. & Linic, S. Engineering selectivity in heterogeneous catalysis: Ag nanowires as selective ethylene epoxidation catalysts. *J. Am. Chem. Soc.* **130,** 11264–5 (2008).

19. Christopher, P. & Linic, S. Shape- and Size-Specific Chemistry of Ag Nanostructures in Catalytic Ethylene Epoxidation. *ChemCatChem* **2,** 78–83 (2010).

20. Linic, S. & Christopher, P. Overcoming Limitation in the Design of Selective Solid Catalysts by Manipulating Shape and Size of Catalytic Particles: Epoxidation Reactions on Silver. *ChemCatChem* **2,** 1061–1063 (2010).

21. Greeley, J., Rossmeisl, J., Hellmann, A. & Norskov, J. K. Theoretical Trends in Particle Size Effects for the Oxygen Reduction Reaction. *Zeitschrift für Phys. Chemie* **221,** 1209–1220 (2007).

22. Singh, P. & Buttry, D. a. Comparison of Oxygen Reduction Reaction at Silver Nanoparticles and Polycrystalline Silver Electrodes in Alkaline Solution. *J. Phys. Chem. C* **116,** 10656–10663 (2012).

23. Marimuthu, A., Christopher, P. & Linic, S. Design of Plasmonic Platforms for Selective Molecular Sensing Based on Surface-Enhanced Raman Spectroscopy. *J. Phys. Chem. C* **116,** 9824–9829 (2012).

24. Xia, X., Zeng, J., Oetjen, L. K., Li, Q. & Xia, Y. Quantitative analysis of the role played by poly(vinylpyrrolidone) in seed-mediated growth of Ag nanocrystals. *J. Am. Chem. Soc.* **134,** 1793–801 (2012).

25. Herrero, E., Buller, L. J. & Abruña, H. D. Underpotential deposition at single crystal surfaces of Au, Pt, Ag and other materials. *Chem. Rev.* **101,** 1897–1930 (2001).

26. Rycenga, M. *et al.* Controlling the synthesis and assembly of silver nanostructures for plasmonic applications. *Chem. Rev.* **111,** 3669–712 (2011).

27. Taylor, L. S., Langkilde, F. W. & Zografi, G. Fourier transform Raman spectroscopic study of the interaction of water vapor with amorphous polymers. *J. Pharm. Sci.* **90,** 888–901 (2001).

28. Liu, M. & Chen, W. Green synthesis of silver nanoclusters supported on carbon nanodots: enhanced photoluminescence and high catalytic activity for oxygen reduction reaction.

Nanoscale **5,** 12558–64 (2013).

29. Lu, Y. & Chen, W. Size effect of silver nanoclusters on their catalytic activity for oxygen electro-reduction. *J. Power Sources* **197,** 107–110 (2012).

30. Kirowa-Eisner, E., Bonfil, Y., Tzur, D. & Gileadi, E. Thermodynamics and kinetics of upd of lead on polycrystalline silver and gold. *J. Electroanal. Chem.* **552,** 171–183 (2003).

31. Bort, H., Jüttner, K., Lorenz, W. J. & Schmidt, E. Lead adsorption on silver single crystal surfaces. *J. Electroanal. Chem. Interfacial Electrochem.* **90,** 413–424 (1978).

32. Viswanathan, V., Hansen, H. A., Rossmeisl, J. & Nørskov, J. K. Universality in Oxygen Reduction Electrocatalysis on Metal Surfaces. *ACS Catal.* **2,** 1654–1660 (2012).

Chapter 7

General Conclusions and Future Directions

7.1. General Conclusions

The central theme of this dissertation is understanding how the catalytic activity of metal nanoparticle electrocatalysts can be improved through the manipulation of the catalytic site nanostructure. Mechanistic insight from quantum chemical calculations and experiments on well-defined surfaces can inform the rational design of novel catalytic systems, which can overcome limitations of the state-of-the-art materials. Specifically, the oxygen reduction reaction in low temperature fuel cells was studied because of its significance to renewable energy, but similar strategies can be applied for other chemical processes. The key lies in first identifying which process, or elementary step, exhibits the greatest degree of control on the overall rate. Understanding the rate limiting step on the atomic level can guide the design of catalytic sites with enhanced activity. In this dissertation, the ORR activity of platinum and silver based electrocatalysts was manipulated by controlling the size, shape, and composition of nanoparticles.

The design of ultra-low Pt loading electrocatalysts was motivated by DFT calculations. In order to improve activity relative to the Pt(111) surface, it is necessary to slightly destabilize OH binding energy by roughly 0.1eV. With insight from quantum chemical calculations, we developed a class of Pt monolayer electrocatalysts with a special structure that enabled independent control over chemical ligand and lattice strain effects. As a result, OH affinity on these materials could be selectively reduced by inducing compressive strain, which is achieved by increasing the composition of Cu within the core. Superior ORR activity compared to Pt/C benchmarks was

achieved by alloys with ~ 80 % Au content in alloy core. Rigorous characterization and electrochemical testing confirm these enhancement result from alloy structure rather than size/shape effects.

In order to improve alkaline ORR activity on Ag based electrodes, the shape of Ag nanoparticles were manipulated to concentrate active catalytic sites.[1] Ag nanocubes terminated with the less coordinated (100) sites were expected to outperform Ag nanospheres, but rigorous electrochemical testing determined that spheres are slightly more active that cubes. An array of *ex-situ* and *in-situ* experiments were performed to verify the stability of the nanoparticle morphologies during catalyst preparation and after electrochemical testing. Distinct Pb_{UPD} stripping spectra enabled relative abundance of 111 and 100 sites to be compared. Ultimately, the relative performance of these Ag nanoparticle systems were consistent with results from single crystal studies.

7.2. Future Directions

7.2.1. Pt monolayer catalysts

Pt monolayer electrocatalysts developed for ORR studies can be used in applications where slightly modified Pt surfaces are preferred such as methanol oxidization.[2] Manipulation of the particle core can make Pt surface atoms either more or less chemical active than unadulterated Pt. Unfortunately, there are two major drawbacks for using these materials as ORR catalysts.

First, the cost of Au within the particle core makes these electrocatalyst prohibitively expensive for widespread application. Strategies for synthesizing cheaper core materials, such as Au-coated carbides, should be actively pursued. Fine control over the properties of the core would enable similar control over reactivity as displayed in AuCu@Au@Pt electrocatalysts.

Second, our Pt monolayer electrocatalysts do not exhibit superior stability compared to other Pt alloy electrocatalysts.[3–5] Initial results of our degradation studies indicate that Pt atoms irreversibly detach from the surface. The origin and mechanism of this restructuring is uncertain, but understanding this phenomenon could lead to the development of more stable materials.

7.2.2. Ag-Alloy electrocatalysts

Our recent work on Ag nanoparticle electrocatalysts suggest increasing the coverage of (111) terrace sites will only slightly improve alkaline ORR activity. Efforts should instead focus on developing Ag-alloys that are better at activating O_2. There have only been a few studies in this area, but there is opportunity to make significant advances with insight gained from Pt alloy studies.[6–8] Catalytic enhancements can be achieve through chemical ligand interactions or by slightly expanding the spacing between Ag surface atoms.

7.3. References

1. Van Cleve, T., Gibara, E. & Linic, S. Electrochemical Oxygen Reduction Reaction on Ag Nanoparticles of Different Shapes. *ChemCatChem* (2015). doi:10.1002/cctc.201500899
2. Antolini, E., Salgado, J. R. C. & Gonzalez, E. R. The methanol oxidation reaction on platinum alloys with the first row transition metals. *Appl. Catal. B Environ.* **63,** 137–149 (2006).
3. Zhang, J., Sasaki, K., Sutter, E. & Adzic, R. R. Stabilization of platinum oxygen-reduction electrocatalysts using gold clusters. *Science* **315,** 220–2 (2007).
4. Nilekar, A. U. *et al.* Bimetallic and Ternary Alloys for Improved Oxygen Reduction Catalysis. *Top. Catal.* **46,** 276–284 (2007).
5. Gong, K., Su, D. & Adzic, R. R. Platinum-monolayer shell on AuNi(0.5)Fe nanoparticle core electrocatalyst with high activity and stability for the oxygen reduction reaction. *J. Am. Chem. Soc.* **132,** 14364–6 (2010).
6. Holewinski, A., Idrobo, J.-C. & Linic, S. High-performance Ag-Co alloy catalysts for electrochemical oxygen reduction. *Nat. Chem.* **6,** 828–34 (2014).
7. Tang, M. & Yi, Q. Synthesis and Electrocatalysis Activity of Silver-Tin Bimetallic Catalysts for Oxygen Reduction Reaction. *Chinese J. Appl. Chem.* **30,** 1176–1181 (2013).
8. Jin, Y., Chen, F., Lei, Y. & Wu, X. A Silver-Copper Alloy as an Oxygen Reduction Electrocatalyst for an Advanced Zinc-Air Battery. *ChemCatChem* **7,** 2377–2383 (2015).